NAVAL POSTGRADUATE SCHOOL
Monterey, California

THESIS

BEDFORM EVOLUTION AND SEDIMENT TRANSPORT UNDER BREAKING WAVES

by

Micah A. Weltmer

March 2003

Thesis Advisor:	Timothy P. Stanton
Second Reader:	Edward B. Thornton

THIS PAGE INTENTIONALLY LEFT BLANK

REPORT DOCUMENTATION PAGE		*Form Approved OMB No. 0704-0188*
Public reporting burden for this collection of information is estimated to average 1 hour per response, including the time for reviewing instruction, searching existing data sources, gathering and maintaining the data needed, and completing and reviewing the collection of information. Send comments regarding this burden estimate or any other aspect of this collection of information, including suggestions for reducing this burden, to Washington headquarters Services, Directorate for Information Operations and Reports, 1215 Jefferson Davis Highway, Suite 1204, Arlington, VA 22202-4302, and to the Office of Management and Budget, Paperwork Reduction Project (0704-0188) Washington DC 20503.		
1. AGENCY USE ONLY *(Leave blank)*	**2. REPORT DATE** March 2003	**3. REPORT TYPE AND DATES COVERED** Master's Thesis
4. TITLE AND SUBTITLE: Bedform Evolution and Sediment Transport under Breaking Waves		**5. FUNDING NUMBERS**
6. AUTHOR(S) Weltmer, Micah A.		
7. PERFORMING ORGANIZATION NAME(S) AND ADDRESS(ES) Naval Postgraduate School Monterey, CA 93943-5000		**8. PERFORMING ORGANIZATION REPORT NUMBER**
9. SPONSORING / MONITORING AGENCY NAME(S) AND ADDRESS(ES) N/A		**10. SPONSORING / MONITORING AGENCY REPORT NUMBER**
11. SUPPLEMENTARY NOTES The views expressed in this thesis are those of the author and do not reflect the official policy or position of the Department of Defense or the U.S. Government.		
12a. DISTRIBUTION / AVAILABILITY STATEMENT Approved for public release; distribution is unlimited.		**12b. DISTRIBUTION CODE**

13. ABSTRACT *(maximum 200 words)*

Observations of the temporal evolution of ripples are analyzed in terms of geometry, migration, crest orientation, and their predicted geometry by models using wave orbital velocities. Two weeks of bedform data were obtained in the surf zone during the RIPEX/SBE in April, 2001. Bed sediment consists of medium- to coarse-grained sand (D_{50}=0.43mm). Models capture temporal trends in ripple geometry, but regression analyses show that they do not handle the range in forcing characteristics and geometries in the surf zone well. Transport models of bedload and total load formulated under uni-directional flows qualitatively capture the temporal evolution of observed transport by ripples, suggesting that under low to moderate forcing, bed load and suspended load occur mostly within the bed-following bottom boundary layer, and are measurable by ripple migration alone. Models predict large transport rates when flat beds were observed, so that at higher forcing ripples cannot be used to measure total sediment transport. Using a two-dimensional probability density function (PDF) of vector displacement peaks, a new ripple analysis model is proposed, incorporating a hierarchy of forcing complexity that includes such physical processes as directional spreading, axis rotation, orbital asymmetry, superimposed currents and infragravity wave velocities. The two-dimensional PDF's are compared with concurrent three-dimensional bed maps and are found to assist in describing ripple sizes, types, orientations, and migration velocities.

14. SUBJECT TERMS Oceanography, Nearshore, Waves, Currents, Bedform Evolution, Sediment Transport, Orbitals			**15. NUMBER OF PAGES** 104
			16. PRICE CODE
17. SECURITY CLASSIFICATION OF REPORT Unclassified	**18. SECURITY CLASSIFICATION OF THIS PAGE** Unclassified	**19. SECURITY CLASSIFICATION OF ABSTRACT** Unclassified	**20. LIMITATION OF ABSTRACT** UL

i

THIS PAGE INTENTIONALLY LEFT BLANK

BEDFORM EVOLUTION AND SEDIMENT TRANSPORT UNDER BREAKING WAVES

Micah A. Weltmer
Lieutenant, United States Navy
B.S., The Pennsylvania State University, 1996

Submitted in partial fulfillment of the
requirements for the degree of

MASTER OF SCIENCE IN METEOROLOGY AND PHYSICAL OCEANOGRAPHY

from the

NAVAL POSTGRADAUTE SCHOOL
March 2003

Author: Micah A. Weltmer

Approved by: Timothy P. Stanton
                Thesis Advisor

                Edward B. Thornton
                Second Reader

                Mary L. Batteen, Chair
                Department of Oceanography

THIS PAGE INTENTIONALLY LEFT BLANK

ABSTRACT

Observations of the temporal evolution of ripples are analyzed in terms of geometry, migration, crest orientation, and their predicted geometry by models using wave orbital velocities. Two weeks of bedform data were obtained in the surf zone during the RIPEX/SBE in April, 2001. Bed sediment consists of medium- to coarse-grained sand (D_{50}=0.43mm). Models capture temporal trends in ripple geometry, but regression analyses show that they do not handle the range in forcing characteristics and geometries in the surf zone well. Transport models of bedload and total load formulated under uni-directional flows qualitatively capture the temporal evolution of observed transport by ripples, suggesting that under low to moderate forcing, bed load and suspended load occur mostly within the bed-following bottom boundary layer, and are measurable by ripple migration alone. Models predict large transport rates when flat beds were observed, so that at higher forcing ripples cannot be used to measure total sediment transport. Using a two-dimensional probability density function (PDF) of vector displacement peaks, a new ripple analysis model is proposed, incorporating a hierarchy of forcing complexity that includes such physical processes as directional spreading, axis rotation, orbital asymmetry, superimposed currents and infragravity wave velocities. The two-dimensional PDF's are compared with concurrent three-dimensional bed maps and are found to assist in describing ripple sizes, types, orientations, and migration velocities.

THIS PAGE INTENTIONALLY LEFT BLANK

TABLE OF CONTENTS

THIS PAGE INTENTIONALLY LEFT BLANK

LIST OF FIGURES

LIST OF TABLES

THIS PAGE INTENTIONALLY LEFT BLANK

ACKNOWLEDGEMENT

I would like to thank my advisor Professors Tim Stanton and second reader Professor Ed Thornton for providing the opportunity to work with such an amazing and exciting data set, and with the fantastic group of individuals who were involved in the Rip Current and Steep Beach Experiments. Professor Stanton kept me on track while allowing me to work independently and make mistakes, and never stopped pushing me towards the lofty goals he had set.

Thank you also to Jim Stockel, Rob Wyland, and Mark Orzech, whose programming and technical expertise allowed me to learn and understand the intricacies of MATLAB and ocean instrumentation. Thank you to Ken Heller for your support in cleaning, drying, and sieving the RIPEX sediment samples in such eleventh hour fashion.

To Mona, my wife, thank you for your undying support of my studies and hopes for a meaningful and respected degree and thesis. For putting up with the foul moods, long days, and working weekends, I am always grateful. I love you.

THIS PAGE INTENTIONALLY LEFT BLANK

I. INTRODUCTION

Sediment transport on a sandy beach under breaking waves is driven by wave and current velocities that are sufficient to mobilize the bed sediments. Ripples are generated under certain conditions, increasing the relative roughness of the bed and providing a clear result-based measurement of sediment transport. Understanding net transport is fundamental to modeling the evolution of any beach system, and to determining the seasonal variability and long-term change of the shore face. Large transport rates can cause objects such as sewage outlet pipes, bedrock, or even mines to be selectively covered or exposed. In studying sediment transport, it is important to understand the hydrodynamic conditions necessary for bed mobilization, and the manner in which different modes of transport and settling occur afterwards to generate and move ripples.

Although not well understood, current wisdom theorizes that in oscillatory flow conditions, two related mechanisms drive sediment transport: bed load and suspended sediment flux. Bed load, or saltation, occurs when sediment particles travel along the bed surface, but do not get ejected out of the thin oscillatory boundary layer into the upper water column as suspended load. The separation between bed load and suspension is not well defined, and often boundary-layer suspension is considered bed load, or thick saltation layers is considered suspended sediment. These processes are readily observed at any sandy beach, and are believed to generate ripples in oscillatory flow conditions by dynamically establishing preferential suspension and deposition sites within each wave orbit cycle. When active, migrating ripples are present, they can be used to diagnose the direction and the speed of the net sediment transport contained in the ripple migration. Presence of the ripples also affects the roughness that the wave velocities "feel" underneath. The resulting increases in bottom roughness affects the amount of sediment that gets suspended by a given flow, which in turn increases the transport that occurs outside of the bed load and ripple migration region.

A. RIPPLE FORMATION

Ripples on a sandy bed are formed in response to sediment motion under an oscillatory flow, when the wave-induced velocities near the bed are of sufficient strength to mobilize the sediments. *Shields* [1936] proposed that sediment suspension is initiated when the lifting force of the fluid exceeds the gravitational and frictional retarding force of the grains. The Shields Parameter [*Shields, 1936*] is a simple ratio of lifting force to gravitational force

$$\theta' = \frac{u_*^2}{(s-1)gD} \tag{1}$$

where u_* is the shear velocity, $s = \rho_s/\rho_w$ is the relative density of the grain to the fluid, and D is the grain diameter. θ' represents the instantaneous Shields Number at a given time in given conditions. Sediment movement is initiated at some critical shear velocity u_{*c} calculated by *Shields* [1936] as

$$\theta_c = \frac{u_{*c}^2}{(s-1)gD} = \frac{\tan\phi}{c_D}\frac{4}{3\alpha^2} \tag{2}$$

where θ_c is the critical Shields Parameter, ϕ is the angle of repose for the sediment, typically around 30°, and c_D and α are non-dimensional coefficients of drag and shear, respectively. θ_c is commonly estimated to be on the order of 0.05, leading *Miller et al.* [1977] to estimate a critical shear velocity $u_{*c}=1.51$ cm/s, where sand grains ~0.28mm in diameter begin to mobilize on a uniform, horizontal bed.

Bagnold [1946] observed from a laboratory swing apparatus that ripples form from a flat bed orthogonal to the orientation of motion, and with properties that depend on the strength of the near bed orbital velocities and displacements. The orbital displacements of narrow-banded wave energy established preferential suspension and deposition locations for saltation, corresponding to the locations of the ripple troughs and crests. Once organized, these ripples continue to grow by saltation from the troughs to crests until orbital velocity increases enough so that the length of the velocity shadow in the lee of a ripple overtakes next crest. *Bagnold* termed these 'rolling-grain ripples' and observed them to remain stable under conditions less than twice the energy required (above) to set grains in motion, or *θ'<0.10.*

Continuing with *Bagnold's* [1946] arguments, once this second threshold is exceeded, ripples grow steep enough to separate the flow and produce vortices in the lee of the ripple. These vortices, if strong enough, can sweep sediment from the lee side of the ripple to be deposited at the next crest and further increase the steepness. The cross-flow wavelength of these so-called vortex ripples grows along with the height until a steady state is reached between the orbital displacement and sediment parameters. At this steady state, the vortex erodes the ripple trough at the same rate that the free flow erodes the crest. Under these conditions, the ripple steepness, defined as the ratio of the ripple height η to the ripple wavelength λ, remains constant. This equilibrium is also determined in part by the sediment type, size, and its still-water angle of repose ϕ. The steady-state vortex (orbital) ripple steepness η/λ was observed by *Bagnold* [1946] to be between 0.125 and 0.20.

Nielsen [1981] suggested that when wave forcing increases, the vortex erosion in the troughs can no longer hold pace with the shearing of the ripple crests. Thus the steady-state steepness for orbital ripples is also the maximum steepness the ripples will attain. The result of this crest shearing and decrease in steepness is one of two options. Either the ripples will begin to reorganize into longer wavelengths, to allow larger and stronger vortices to be generated, or, if the orbitals are too energetic, they will erode completely and sheet flow conditions commence. The threshold for this transition to sheet flow is proposed to be a function of the Shields Parameter, with $\theta' \leq 0.20$ necessary to maintain vortex ripples.

In the field, calm conditions are not characterized by a flat bed, but rather by relict ripples that were formed under higher forcing. Rolling-grain processes are superimposed upon the relicts as wave energy increases again, and a new equilibrium will be established. Flat beds do occur under sheet flow conditions, and ripples reform when the energy declines into the active vortex ripple range.

Following these arguments, many empirical models have been developed to evaluate the geometry of ripples from laboratory experiments as well as field studies in a variety of wave and current forcing conditions. *Nielsen* [1981] used the laboratory flume and swing observations of *Bagnold* [1946], *Carstens et al.* [1969], *Mogridge and*

Kamphuis [1972], and *Miller and Komar* [1980a], along with the field observations of *Inman* [1957], and *Dingler* [1974], to create a model of ripple geometry empirically fit to Shields number and mobility number (ψ, indicating the strength of the flow relative to gravity restoring force – see section 3B), and scaled to wave orbital semi-excursion *a*. *Grant and Madsen* [1982] also used the data of *Carstens et al.* [1969] and others to empirically fit a normalized Shields number to *a*-scaled ripple geometry. This formulation has been subsequently evaluated and adjusted to fit observations [*Li et al.,* 1997, *Li and Amos,* 1998] under a variety of forcing conditions, making it another respected model. Another ripple geometry model that has proven effective is *Wiberg and Harris* [1994], who used lab data [*Carstens et al.,* 1969, *Mogridge and Kamphuis,* 1972, *Dingler,* 1974, *Clifton and Dingler,* 1984] and field observations [*Inman,* 1957, *Dingler,* 1974, *Miller and Komar,* 1980b] to empirically relate ripple geometry not to a computationally derived parameter, but to the wave orbital diameter *d=2a* and its relation to ripple height. Although these studies focused on field observations under wave-dominated forcing, none considered observations at or near the region of breaking waves. This study evaluates the ripple predictors of *Nielsen* [1981], *Grant and Madsen* [1982], *Li et al.* [1997], and *Wiberg and Harris* [1994] for their applicability in the surf zone from a variety of ripple observations made within the surf zone.

Li et al. [1997] compared two total load and two bed load sediment transport predictors, all derived from uni-directional flume observations [*Engelund and Hansen,* 1967, *Brown,* 1950, *Bagnold,* 1963, and *Yalin,* 1963], to observed ripple mass transport under combined wave and current dominated flows. All but *Yalin* [1963] were found to reasonably agree with observed transport. This study also compares the sediment transport predictors of *Engelund and Hansen* [1967], *Brown* [1950], *Bagnold* [1963] to mass transport estimates based on observed ripple geometry and migration rates.

The formation and migration of orbital ripples results from a combination of bed load, sediment suspension, and the processes that force them. When conditions are below critical sediment motion thresholds, sediment transport is nearly negligible and if relict ripples exist, they do not migrate. As wave forcing increases and sediment is mobilized, bed load and selective suspended sediment transport during each wave orbit enhance

ripple formation and cause the ripples to migrate. Saltation is observed to occur in only a very thin boundary layer above the bed that follows the shape of the bedforms, and is believed to directly contribute to the alteration and net movement of ripples. Sediment suspension within vortex ripples, as discussed above, occurs during each wave cycle, primarily as the scouring of ripple troughs during the orbital velocity maximum, and settling of suspended sediment near the ripple crest. Thus it is proposed that while the near bed wave orbital velocity is within or near the orbital ripple regime, total sediment transport can be reasonably estimated by observing the sediment mass flux as reflected in ripple migration. When forcing increases further and the bottom boundary layer thickness becomes comparable to the ripple height, ripple crests begin to shear off, the troughs fill in and sediment transport is necessarily via bed load and boundary layer suspension, and other observations of sediment transport become necessary.

B.   RIPPLE OBSERVATION TECHNIQUES

Technologies for determining ripple geometry have evolved from periodic diver measurements [*Wright et al.*, 1984], through bottom-mounted cameras [*Boyd et al.*, 1988, *Li and Amos*, 1998], to fixed rotary sidescan sonars [*Hay and Wilson*, 1994, *Traykovski et al.*, 1999]. The advancement from diver measurements to photographs allowed for a continuous time series of observations under varying surface conditions, but both photography and sidescan sonar produce 2-dimensional images of the sea bed, but leave ripple height unknown.

Structured lights and shadow bars have been added to the field of photographs [*Li and Amos*, 1998, *Dixon,* 2000], to infer ripple height, but this provides only a single profile measurement of the ripple field, and observations are severely limited by sediment opacity under even moderate wave forcing. Detailed analysis of the sidescan sonar data allows an estimate of ripple height under visually opaque conditions [*Traykovski et al.*, 1998], but only as a proxy to the standard deviation of the return times at a given beam incidence angle, generating a single ripple height for a number of ripples. A single-point measurement (eg., an altimeter) solves the dilemma between continuous data and resolving ripple height, but even when used in conjunction with a imaging technique, still

yields bed height at only a single location. Estimating ripple geometry from single point altimeters relies explicitly upon migration of the ripples, prior knowledge of the ripple orientation, and the assumption that the ripples are spatially uniform.

Robust suspended sediment measurements are more difficult. Until very recently, only qualitative estimates of suspended sediment could be made in the laboratory or, especially, the field. Recent development of acoustic devices that can measure suspended sediment concentration [*Stanton*, 2000, *Hanes et al.*, 2001] and even grain size distribution [*Howd and Brodersen.*, 2002] from acoustic backscatter levels represent advances in our ability to measure in situ suspended sediment concentration profiles.

The Rip Current Experiment (RIPEX) and concurrent Steep Beach Experiment (SBE) produced a detailed set of continuous observational data that combines three-dimensional bed altimetry maps, co-incident suspended sediment concentration, wave surface measurements, and three component velocity profiles within the surf zone. Concurrent concentration and velocity profiling methods with a bistatic coherent profiler [*Stanton*, 2000] allowed centimeter-scale sediment fluxes to be measured under restricted conditions. The objective of this paper is to analyze the wave forcing and bed response data collected during these experiments. A wide variety of forcing conditions were recorded during the 14-day deployment, from actively migrating orbital ripples through elimination of bedforms by a storm during sheet flow conditions, and the subsequent regeneration of ripples. Existing ripple geometry and sediment transport models are evaluated using these field data, and a new approach to these types of models is proposed.

II. EXPERIMENT

The data presented here were collected as part of the Rip Current Experiment (RIPEX) and Steep Beach Experiment (SBE) from 07 April through 07 May, 2001. These concurrent experiments examined the forcing and morphologic variability associated with a rip cell system offshore from a steep beach face across a range of temporal and spatial scales.

A.   ENVIRONMENT

The shoreline of Sand City, California, in the southern end of Monterey Bay, is a moderately erosional beach backed by large continuous sand dunes, on the order of 10m high. Offshore wave climatology for April was an average 2.2m significant wave height with a range of 1-6m, and a mean wave period of 7.4 seconds, with a peak of 12 seconds [*NOAA buoy data*]. The beach slope is moderate (1:30) with a shoal of decreased slope just outside the intertidal zone. Median sediment grain size is .43 mm, measured three times during the experiment near the boundary layer measurement site. Since the provenance of the sediment is the granite and sandstone from the Coast Ranges of central California, grain composition was observed as dominantly quartz, with noticeable fractions of feldspar, epidote, garnet, and olivine.

Blocking by the bay's headlands (figure 1) and the refraction of wave energy by the Monterey Canyon result in nearly shore-normal incident wave energy on the beach. Strong shore-normal incident energy and steep beach profiles characteristically produce strong, persistent rip currents (figure 2). Since these features are all persistent in this region of Monterey Bay, it is a good location to study rip current dynamics, and is conveniently located near to the logistical support at the Naval Postgraduate School.
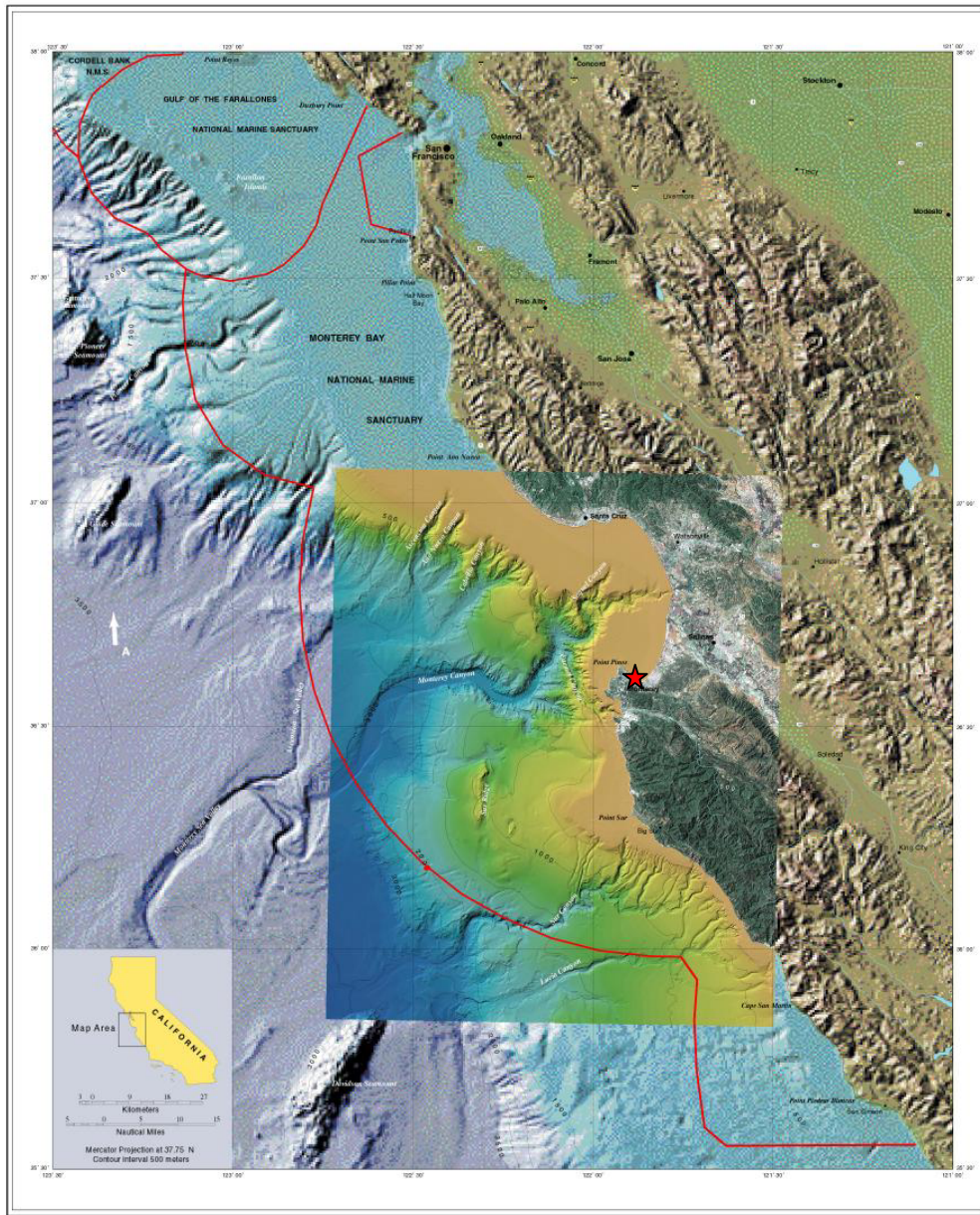
Figure 1. Bathymetry map of Monterey Bay, showing approximate location of RIPEX/Steep Beach Experiment (SBE). Courtesy of MBARI.

The rip channels at the Sand City site are spaced 100-150m apart, and consist of deep, narrow channels in broad, shore-connected shoals that exist along many kilometers of this shoreline [*MacMahan et al*., submitted to J. Geophys. Res., 2002, *Reniers et al*., submitted to J. Geophys. Res., 2002] (see figure 3). In turn, the morphology of the rip

8

channels funnels the return flow of the onshore mass flux of the waves, creating a positive feedback mechanism for sustaining the rip channels and currents.

Figure 2. Photograph of Sand City, CA shoreline, showing evenly spaced rip channels and associated currents and the continuous dunes behind the beach.

The Steep Beach portion of the experiment analyzed the forcing and morphologic variability across the broad shoal between rip channels at small temporal and spatial scales. While the context of the rip cell is kept in mind throughout this analysis, the focus is on bed morphology observations near the middle of a shoal.
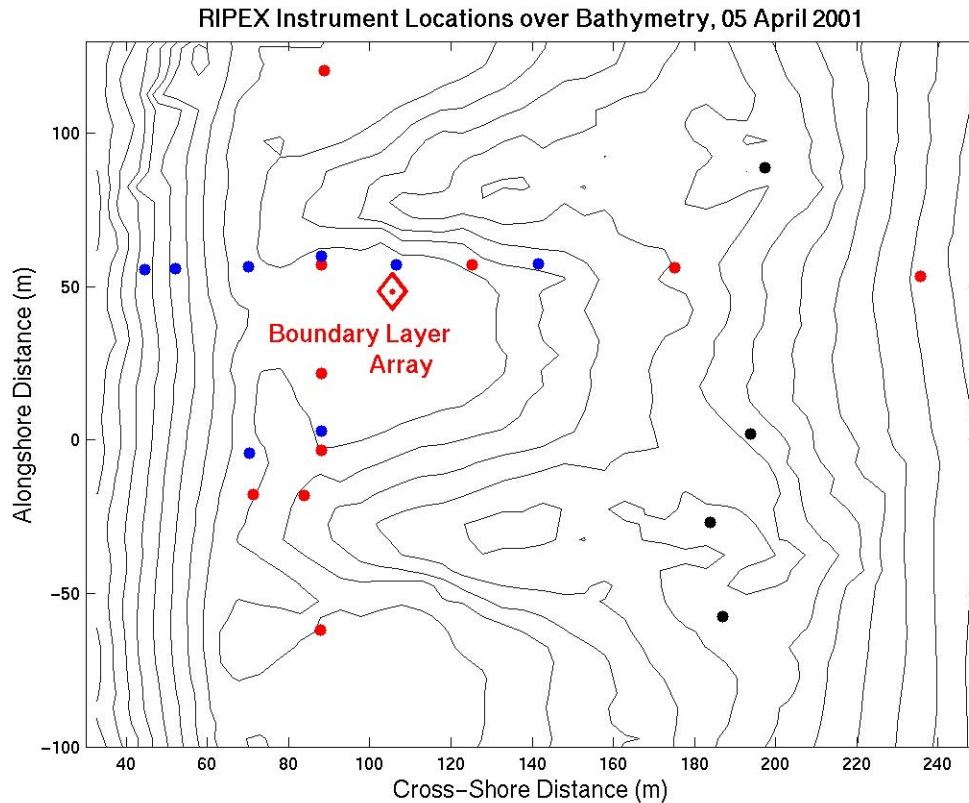
Figure 3. Contour map of RIPEX/SBE study area at the beginning of the experiments. Superimposed are the locations of the deployed instruments and the SBE tower array.

B. EXPERIMENTAL DESIGN

The primary instruments used for this analysis were mounted on a fixed boundary layer array that held a vertical stack of Electromagnetic Current Meters (EMCM) from approximately 30 to 220 cm above the bed to resolve mean, wave and turbulent velocity profiles (figure 4), a Scanning x-y Acoustic Altimeter (SAA) that produced three-dimensional maps of the bed over an area approximately 1.2m x 1.2m square every 30-40 minutes, a Bistatic Coherent Doppler Velocimeter (BCDV) to detect 3D velocity and volume sediment concentration vertically through the water column at 1cm intervals over a 50cm range above the bed, and a surface-piercing capacitance wave staff that measured surface height. The operation of these instruments is described in the next section. The BCDV sample location was within the footprint of the SAA, and the EMCM array was

located to within 3m along shore from the BCDV. The lowest EMCM, nominally 30 cm above the bed, was used to estimate bottom wave forcing as it is robust to bubbly, wave breaking conditions, and was submerged most of the time.
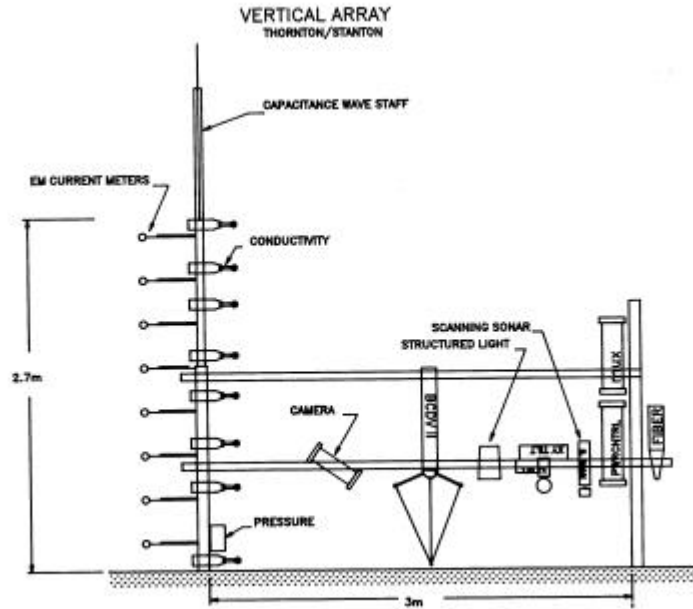
Figure 4. Schematic of Bottom Boundary Layer instrument array, including EMCM's, BCDV, and SAA.

Other instruments deployed for this experiment included an array of Pressure and Horizontal Velocity sensors (PUV's), Acoustic Doppler Velocimeters (ADV's), Acoustic Doppler Current Profilers (ADCP's), and pressure sensors, the locations of which are shown in figure 3 superimposed on the initial bathymetry. One set of instruments was placed in a cross-shore line to measure gradients of wave energy, velocity, and setup. A second line in an alongshore arrangement measured shear instabilities of longshore currents and infragravity waves. Instruments were powered and controlled by a synchronized recording station located at the Sand City Sewer pumping plant with data links to the Naval Postgraduate School's Beach Laboratory on Del Monte Beach.

The location of the fixed boundary layer array from which the data for this thesis was obtained is denoted as the large diamond in figure 3. The overall function of the fixed boundary layer array was to measure the velocity and suspended sediment profile,

surface and bottom boundary layer, and detailed bottom morphology under breaking waves. Instruments mounted on the array but not used in this study include conductivity cells to measure bubble void fractions, structured light and video camera, and another pressure sensor.

The data set of shortest duration is the Scanning Acoustic Altimeter, which recorded from 15-29 April. The tower array containing the EMCM's and capacitance wave staff continued recording to the end of the deployment, but did not begin recording until 16 April. To achieve greatest data coverage, this analysis was limited to that data between 16-29 April, 2001, or yeardays 106-119.

C.   INSTRUMENTS AND PROCESSING

Several different instruments from the boundary layer array were used to acquire the data analyzed for this paper. To fully understand the nature of the measurements and the utility of the data from each instrument, it is instructive to explain how each of the primary instruments works, some of the difficulties encountered, and how the data were processed into a form useful for analysis.

1.   Electromagnetic Current Meters

Seven Electromagnetic Current Meters (EMCMs) were mounted on a tower (figure 4) in the surf zone, ranging in height from 30cm above the bed to approximately 220cm above the bed. These devices consist of 5cm diameter spheres with an internal horizontal coil that excites an oscillating electromagnetic field. Two orthogonal sets of electrodes protruding from the sphere sense extremely small voltages that are induced by the motion of the conductive seawater past the field within a 10cm diameter, which are simply scaled to the two component velocity vector of the fluid. Drift in EMCM measurements is less than 2cm/s and noise is less than 1cm/s RMS.

Because there are no moving parts to the Electromagnetic Current Meter, the data stream is continuous, and the sample frequency is limited to 4 Hz by the processing performed prior to data acquisition, and physical sample volumes. The EMCM stack, capacitance wave staff, and conductivity cell stack (not used in this study) were all synchronously sampled by the BCDV electronics at 15.6 Hz.

12

2.   Surface-Piercing Capacitance Wave Staff

The capacitance wave staff consisted of a 1mm diameter stranded stainless steel wire uniformly coated with Teflon®. The capacitance of the wire with respect to the conductive seawater is proportional to the surface area of wire immersed in water. Since the diameter of the wire is constant along its length, the immersed area is directly proportional to the height of the wire that is immersed. The capacitance was measured with an AC bridge and converted to a voltage, which is scaled to the instantaneous water surface height and fed into the data acquisition system.

3.   Bistatic Current Doppler Velocimeter

The Bistatic Coherent Doppler Velocimeter (BCDV) is a new device developed by the ocean turbulence research group at the Naval Postgraduate School to measure three-component velocity and sediment concentration in 1cm bins at 40Hz. This instrument, mounted on what was termed the "goalpost" (figure 4), uses a single monostatic transducer to emit acoustic pulses at 1.3 MHz, then receive backscattered energy at the central transducer and the 3 surrounding bistatic transducers at 1cm range bins out to 1.2 m range. Sediment concentration was estimated from the backscattered power measured by the central transducer over an 80dB dynamic range, using a laboratory calibration based on an in situ sediment sample.

4.   Scanning X-Y Acoustic Altimeter

Another new instrument developed by the Naval Postgraduate School's ocean turbulence research group and mounted on the goalpost was the Scanning X-Y Acoustic Altimeter (SAA). The SAA continuously measured bed heights to produce a bed height map over a 1.2m x 1.2m square every 30-40 minutes. A pulse-coherent altimeter transducer is mounted on a 2-axis step-motor with the transducer head directed down toward the bed. The transducer was stepped in 1° increments to a range of ±35° in each the cross-shore(x-axis) and alongshore(y-axis) directions. The SAA allowed bedforms

and their temporal variation to be measured even in turbid and optically opaque conditions, which is frequently the case under breaking waves, until either large bubble concentrations made the water column acoustically opaque or the water level fell below the transducer height.

During each mapping cycle, the SAA began sampling by establishing a vertical centerline and stepping back and forth rapidly in the cross-shore while incrementally moving outward in the along-shore direction at the end of each cross-shore pass. When the angle limits were reached in one along-shore direction, the SAA again re-set to the centerline, leveled itself, and proceeded in the same manner in the opposite along-shore direction. Figure 5 shows a typical distribution of raw bed height measurements.
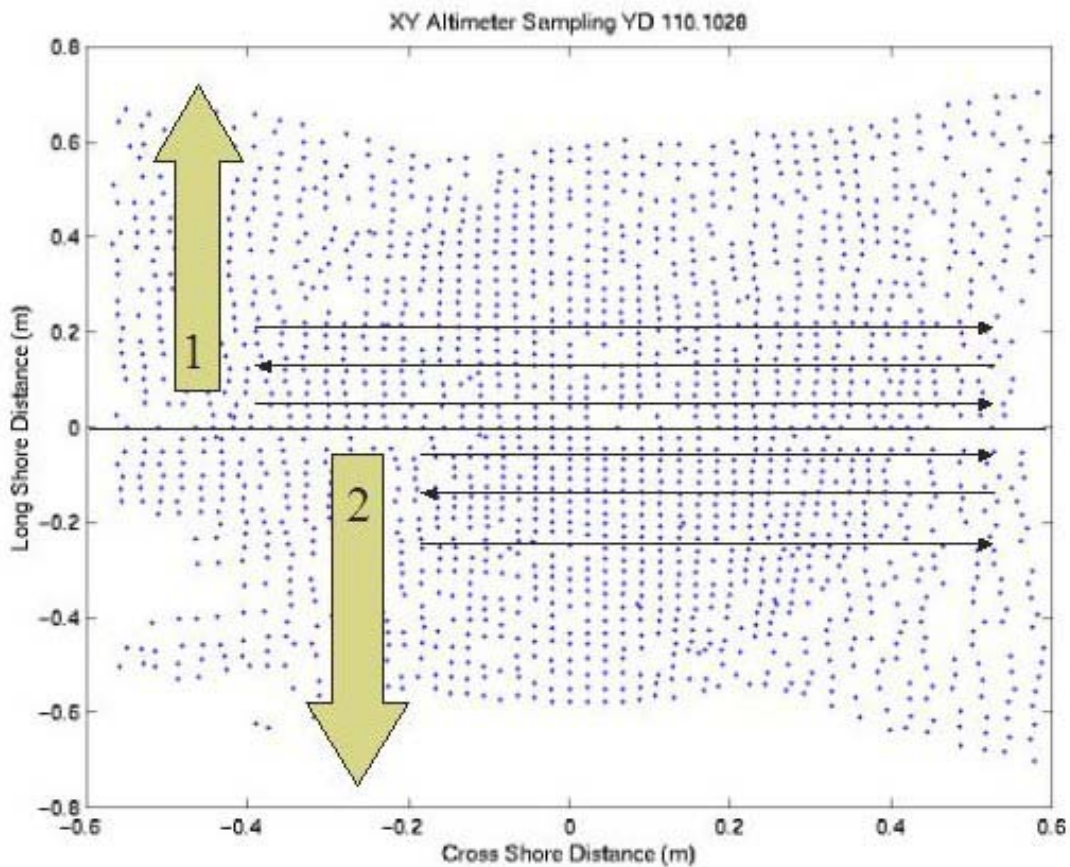
Figure 5. Typical raw bed height sample distribution for the Scanning X-Y Acoustic Altimeter (SAA). The SAA scanned in 1 degree increments over a ±35° range in each axis. Arrows superimposed demonstrate the sampling pattern used by the instrument.

Typical sampling times for a complete map "run" are 30-40 minutes, depending upon the acoustic turbidity (bubbles, etc) and bed load movement. Each point was sampled with 20 pulses of 1.3MHz sound waves. An onboard microprocessor processed the data into a bed range. If the presence of suspended sediment or bubbles prevented detection of the bed, as frequently occurred near the edges of the map, each point would be re-tried three times before incrementing to the next position. In times of excessive sediment or bubbles, map runs commonly exceeded 180 minutes in duration.

In post analysis, an Objective Analysis (OA) algorithm was used to map the spatially irregular data into a uniformly gridded $z(x,y)$ map and generated an error map of center weighted averages of data within a 6cm diameter Gaussian field at each grid point. The result is regular smoothed bottom morphology maps with a nominal horizontal resolution of 1.5cm. Ripple wavelengths from 3cm to 1.2 meters can be resolved from these maps.

Many of the raw maps contained data gaps where the SAA was not able to acquire the bottom. This occurred frequently near the limits of the sampling range, and at low tides when bubble injection obscured the water column or the SAA was above the water, limiting the bed detection to near nadir. While the 6cm sampling range of the OA reduced the size of the gaps and made them a more regular shape, the absence of data clearly dominates many of the maps, except those at the highest tides.

Due to the large sampling duration of each map, and the rapid ripple migration within the surf zone, a second Objective Analysis was performed taking advantage of the double sampling of the centerline profile during each mapping run. If the entire field was OA'ed together, the time difference between centerline samples (at least 15 minutes) caused points within the 6cm Gaussian radius of the centerline to be sampled asynoptically. The result was a smearing of the halves near the centerline into continuous bedforms (figure 6a). The second OA was performed to separately OA each half of the data field, then merge the two analyzed grids at the centerline. The resulting maps often have sharp discontinuities at the centerline, more clearly representing the temporal evolution of the bedforms (figure 6b). Analysis exploiting this 'split field' sampling and processing is described in section A-1 of chapter 3.

a) Bed Morphology, yearday 110.3181

b) Split OA Bed Morphology, yearday 110.3181
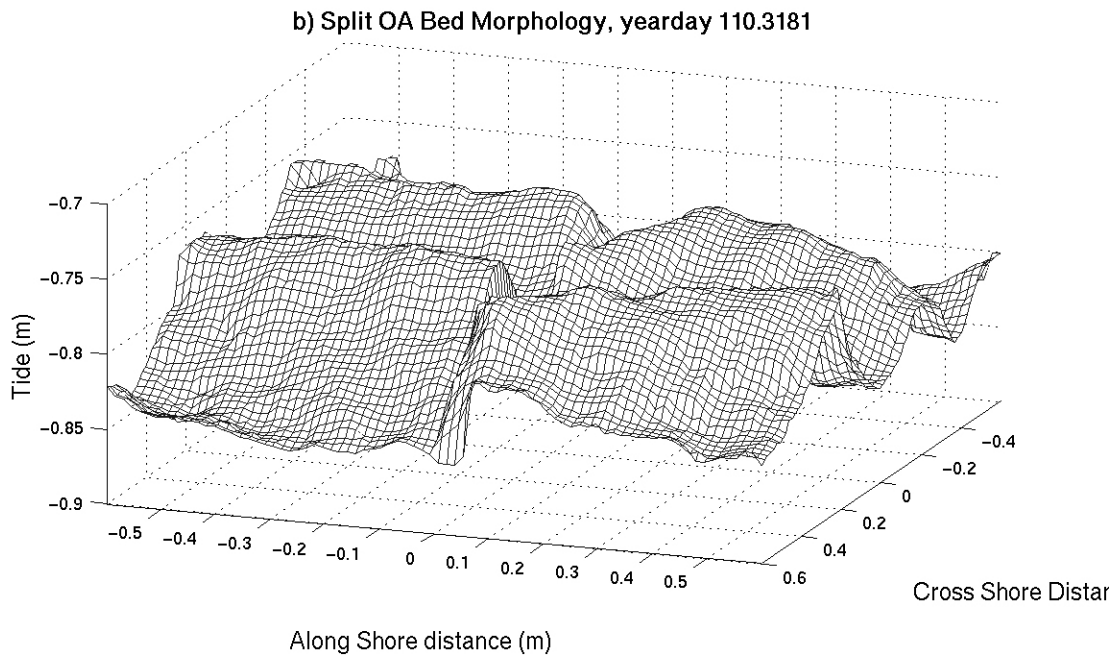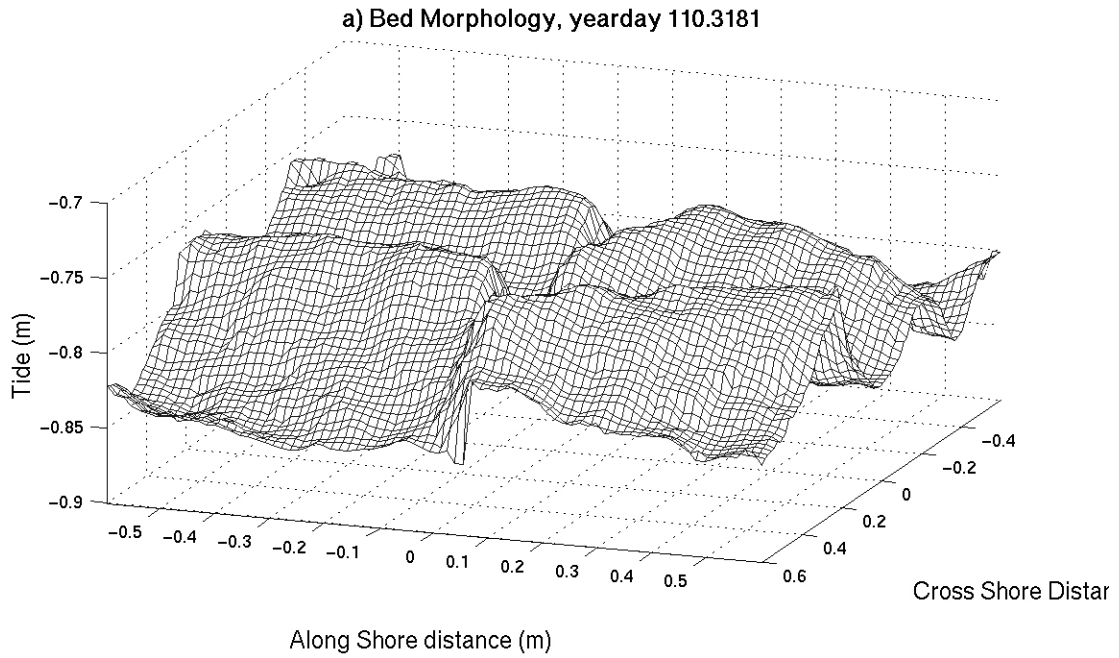
Figure 6. (A) Surface map of the bed as measured by the SAA on Yearday 110.87, using the original Objective analysis. The central discontinuity is smeared and data gaps occur where the altimeter could not acquire the bed. (B) Same as A, except the split OA scheme was used. Note the sharper central discontinuity.

5. Bed Height Corrections

During the experiment, the frame upon which the SAA and BCDV were mounted underwent several movement events. To correct for these support frame movements, a mean bed height of the inner 30cm x 30cm (the most reliable data, directly under nadir) from the OA'ed altimeter grid was calculated and plotted in a time series, shown in figure (7a). These bed heights were then compared to BCDV tilt sensor measurements to make the necessary corrections.

Under strong wave forcing the instrument frame initially tilted up and rotated around the shore-facing back brace poles. This was detected by increasing cross-shore tilts of up to 16° measured by the BCDV (figure 7b). When this problem could be corrected on day 109, the frame was re-jetted into the sediment with improved sand anchors. The result was a slight over-correction of the tilt. The frame began to lift again, this time much more slowly.

A simple geometric model allowed correction of the changing bed heights due to this rotation. Assuming that the bed was level between the anchor locations, the initial tilt ϕ_0 and bed height were used to calculate the rotation radius AB (figure 8). Assuming also that the rest of the goalpost remained rigid, the pre-deployment measured geometry as labeled in figure 8 was used to calculate a height adjustment to be applied to the SAA, based on the tilt angle ϕ, using the equation:

$$dz = R\left(\sin 45\left(\cos\phi - \cos\phi_0\right) + \cos 45\left(\sin\phi - \sin\phi_0\right)\right) + a\left(\cos\phi_0 - \cos\phi\right) \qquad (3)$$

where R is the length of the back support brace and a is the distance of the SAA transducer below the crossbar.

Several discontinuities in bed height that may represent manual adjustments in the cross bar were then compared to a plot of the BCDV y-direction (along-shore) tilts (figure 7c). A perturbation in the tilt reading, corroborated by field notes from the experiment, identified corrections that were to be made. Although several candidate adjustments were identified from comparison of the plots, only two could be reconciled with the field log. The corrections of .25m and .26m on yeardays 110 and 116,

respectively, simply eliminated the observed discontinuities in bed height. The resulting corrections and the final bed height time series are shown in figure 7c and d.
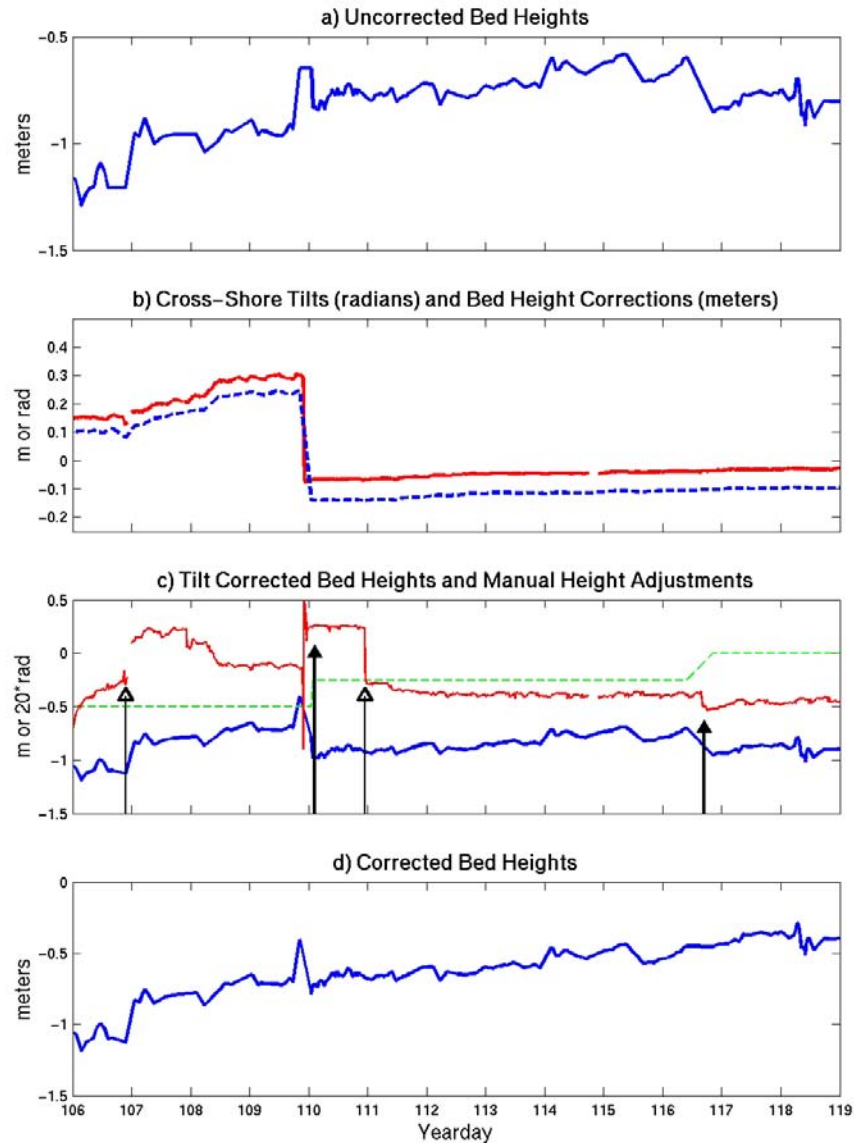
Figure 7. Summary of bed height corrections made. (A) Raw inner bed height means. (B) Cross-shore BCDV tilts (solid red) and corrections made to the bed heights (dashed blue). (C) Bed heights corrected for BCDV tilt (thick blue solid), BCDV along-shore tilts (light red solid), and manual goalpost adjustment corrections (green dashed). Thin arrows indicate candidate correction locations, thick arrows indicate correction locations verified by the field log. (D) Final corrected bed height time series showing net accretion during the experiment.

18
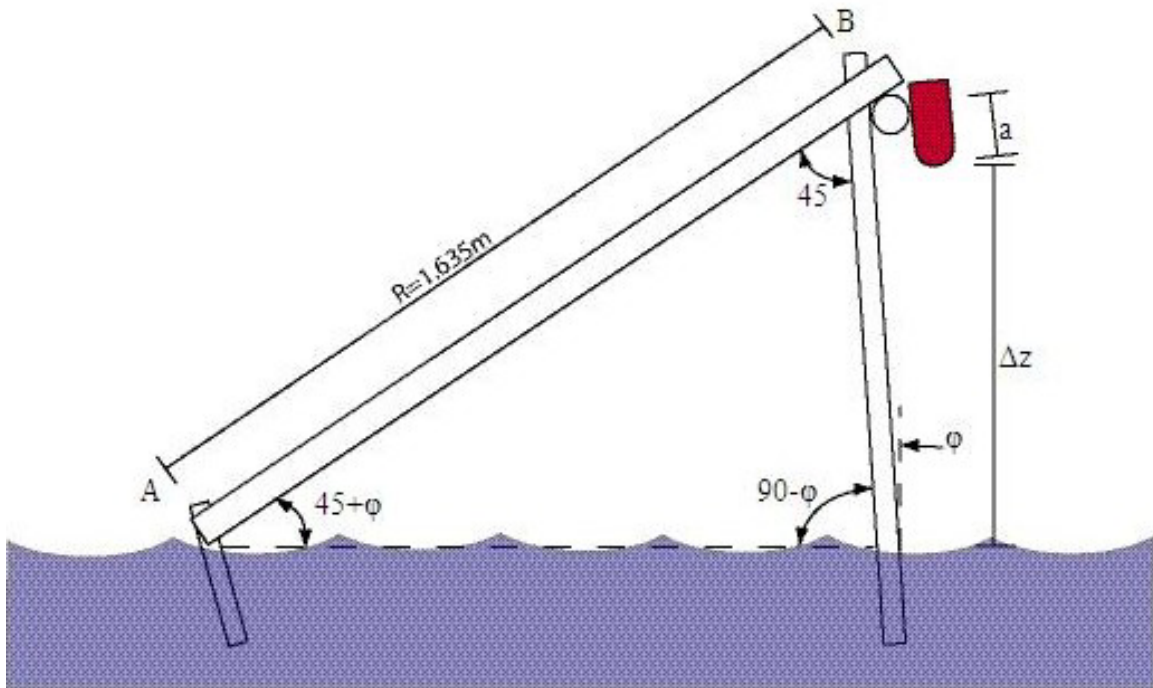
Figure 8. Diagram of "goalpost" geometry. The length of rotation arm AB was estimated from initial tilt and bed height measurements, and the rotation axis A was assumed to be stationary throughout the experiment.

6.   Altimeter Map Coverage

The variability in data coverage, as well as in mapping time is significant. Low data coverage occurs under low water depths and high bubble concentrations that prevent accurate characterization of the bed conditions, and the long mapping times potentially alias the bedform positions as they migrate. Thus, only maps with high data coverage (>85%) and low run times (<90 minutes) are considered for full analysis. The red circles in figure 9 show maps that meet these criteria. Seven distinct cases of groups of good quality data containing sequential maps covering at least 3 hours (0.125 days) were obtained and are labeled in figure 9 and summarized in table 1. Comparing the high quality maps to the tides, one can see that good quality data is obtained only during high tides, with only one exception on yearday 110, when the low tide was deepest. This is because the SAA was mounted such that the water surface was below the transducer head during low tides and because frequent wave breaking/bubble injection events occurred at shallower tides and during higher energy conditions.
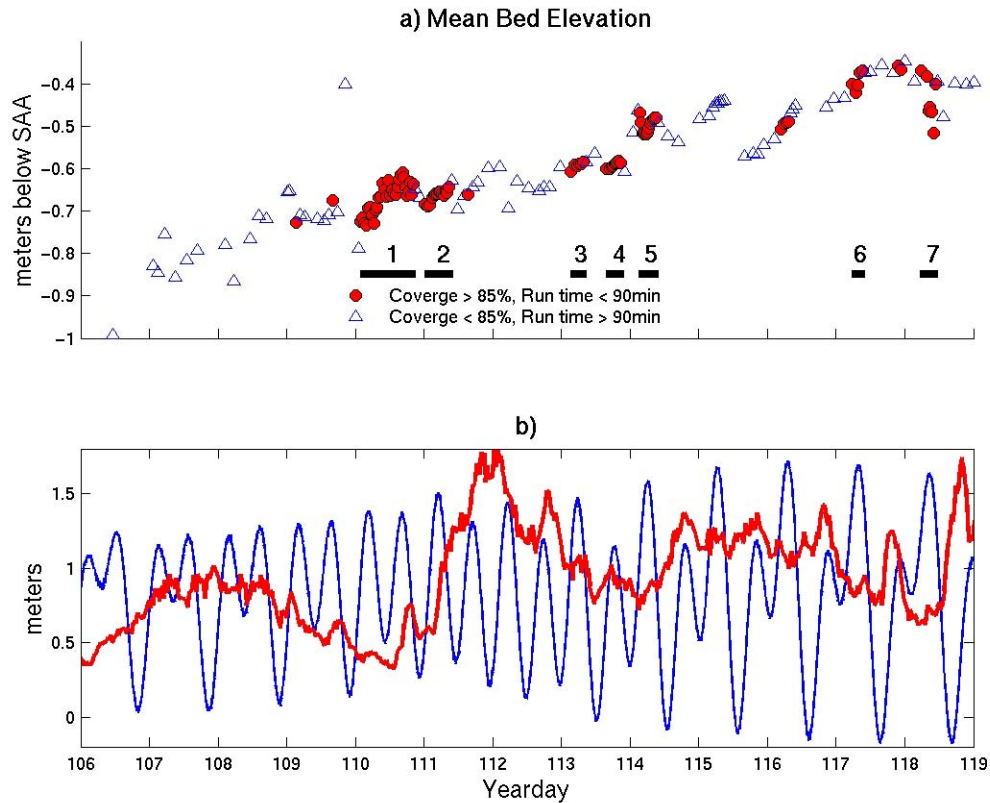
Figure 9. SAA data quality distribution and tidal comparison. (A) Corrected bed height measurements. Maps with coverage greater than 85% and run times less than 90 minutes are shown as red circles. Numbered groups are identified case studies. (B) Tide measurements from the nearby Monterey Harbor (thick blue line), and the offshore significant wave height, H_s (thin red line).

Figure 9 also shows that in addition to the yearday 110 case 1 having the lowest tidal range, it covers the longest time and includes the most sequential maps. If the two maps between cases 1 and 2 are disregarded, both could be merged to create a single continuous case, spanning three high tides. It is this merged case on which the detailed ripple analyses focus. Furthermore, of all the continuous cases, these are the only two in which large bedforms can be fully resolved on the altimeter maps. Several maps on day 109 were able to be fully analyzed, but it is not considered a case due to the discontinuity of maps resolved. Following a storm that passes on yearday 111-112, the bedforms are eliminated, and sheet flow conditions cause essentially flat beds for the remainder of the

cases, until small, broad bedforms with wavelengths in excess of the altimeter footprint begin to appear briefly on yearday 114 (case 5) and again on yearday 118 (case 7). For detailed analysis of ripples and bedforms, the maps in cases 1 and 2 are considered jointly in this study as well as the available maps on day 109, because of the inability to completely resolve bedforms in the other maps.

Case	Time (hr)	Map Coverage	Run time(min)	Mean u(m/s)	Mean v(m/s)	Hs (m)	Orbital diam. (m)	Bed type
1	19.11	95.59 %	36.99	-0.0784	-0.0208	0.4663	0.7633	Active Orbital Ripples
2	9.53	97.50 %	40.82	-0.0728	-0.0223	0.839	0.7269	Active Orbital Ripples
3	5.1	89.83 %	51.01	-0.2446	-0.1944	1.021	1.0852	Sheet Flow
4	6.37	89.83 %	42.48	-0.219	-0.1941	0.9292	1.0394	Sheet Flow
5	6.53	75.37 %	30.14	-0.1201	-0.0863	0.8462	1.061	Sheet Flow
6	4.4	99.03 %	52.77	-0.0794	-0.2546	0.8667	1.6117	Very large ripples
7	5.95	96.10 %	39.66	-0.0987	-0.1453	0.6892	1.5287	Very large ripples

Table 1.   Summary of fully resolved Scanning Acoustic XY Altimeter cases, corresponding to labels on figure 9.

Sediment concentration measurements are also limited within the data set because of contamination of backscatter profiles by surface-injected bubbles.   The high backscatter created by surface injected bubbles can saturate backscatter profiles to the point where little energy reaches the bed. Detection of the bottom depends on being able to resolve the sharp peak in backscatter as the acoustic pulse reaches the bottom, so large bubble injection reduces the chance of resolving the bottom. Also of concern are periods

of thick bed load layers. In many cases where sheet flow is occurring, the top of the bed load layer is likely to be misinterpreted as the bottom. Again, the acoustic pulse is likely not able to penetrate the bed load layer, and thus it must be assumed that in such cases the bed load layer is not thick enough to obscure the shape of any existing bedforms.

7.   Scanning Acoustic Altimeter Post-Processing

Since the SAA took up to 90 minutes to sample even a high quality map, the sampling cannot be regarded as synoptic. The following section describes the method developed to detect and adjust propagating bedforms, and to quantify the geometry of the ripples seen in the altimeter maps.

A first order description of the physical character of uniform long-crested ripples can be accomplished with three parameters: ripple height, ripple wavelength, and crest orientation. Each of these parameters can be calculated by locating the ridges, the troughs, and the relative height of each. An interactive MATLAB function was developed for use on fully resolved ripples that took user-defined input to automatically trace the ridges and troughs as a series of points, and to label each point with a bed height.

After choosing the grid map to analyze, the user is presented with a surface map and a contour map of the chosen grid. From these, he inputs how many ridges and troughs can be identified on each side of the grid. These numbers may all be the same, or they may all be different, based upon the ripple orientation, length, and migration rate, and their locations within the grid. Each half is analyzed individually. For the sake of statistical integrity, only ridges or troughs that extend across the map half are counted. A cross-shore profile for each side of the map is then displayed, and the user identifies each ridge and trough with the cursor.

At this point, the analysis becomes fully automated. The algorithm increments outward in the along-shore direction from the column from which the profiles were generated, and a local maximum within 5 grid points cross-shore of the last identified point is identified for each ridge in each column, (local minimums for troughs). The

locus along each ridge (trough) point is converted to sets of (x, y, z) locations. Figure 10a shows a sample contour map with ridge and trough lines marked.
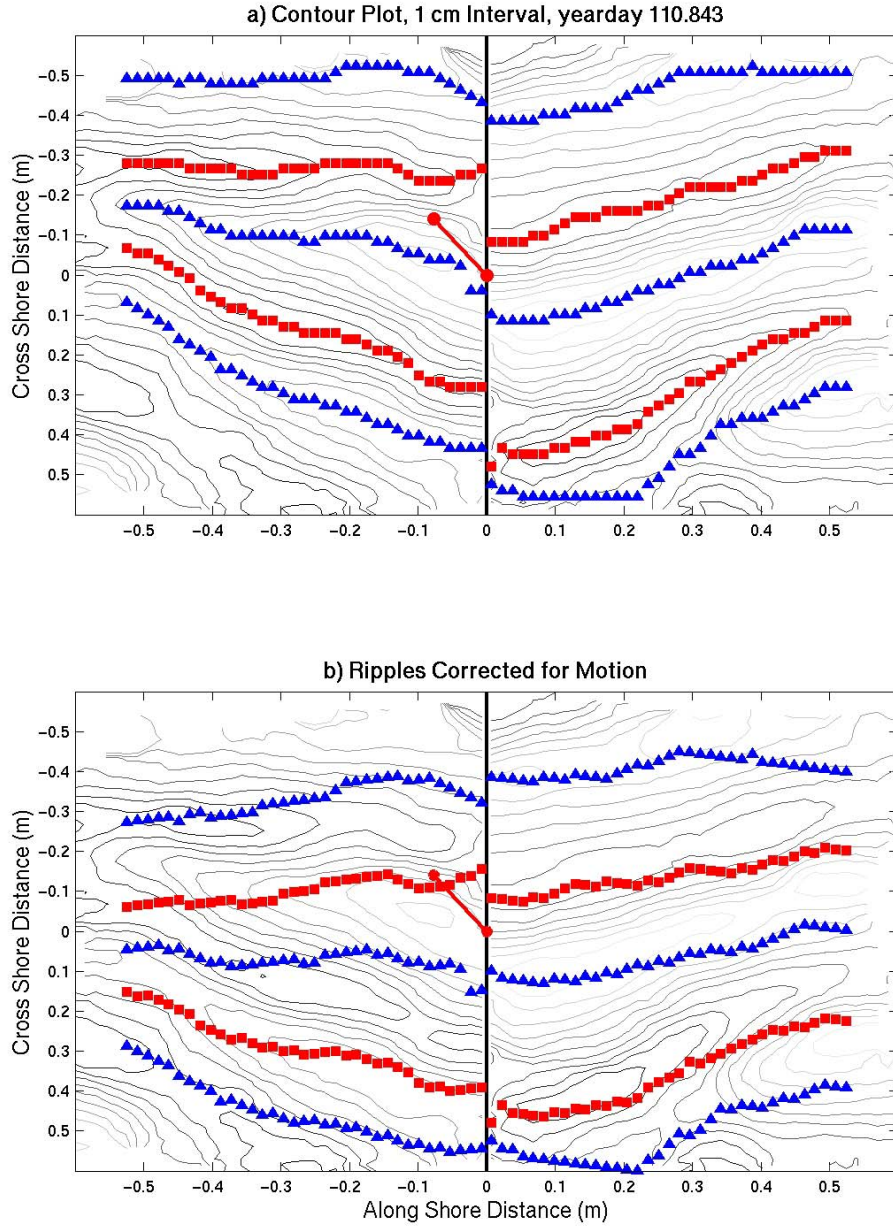
Figure 10. (A) Sample contour map with ripple ridges (triangles) and troughs (squares) marked. (B) Same as A, but with ridges and troughs corrected for ripple migration. The bar in the center of each map represents the vector mean bottom current over the SAA mapping interval, scaled to the axes of the contour map, with units of ms^{-1}.

23
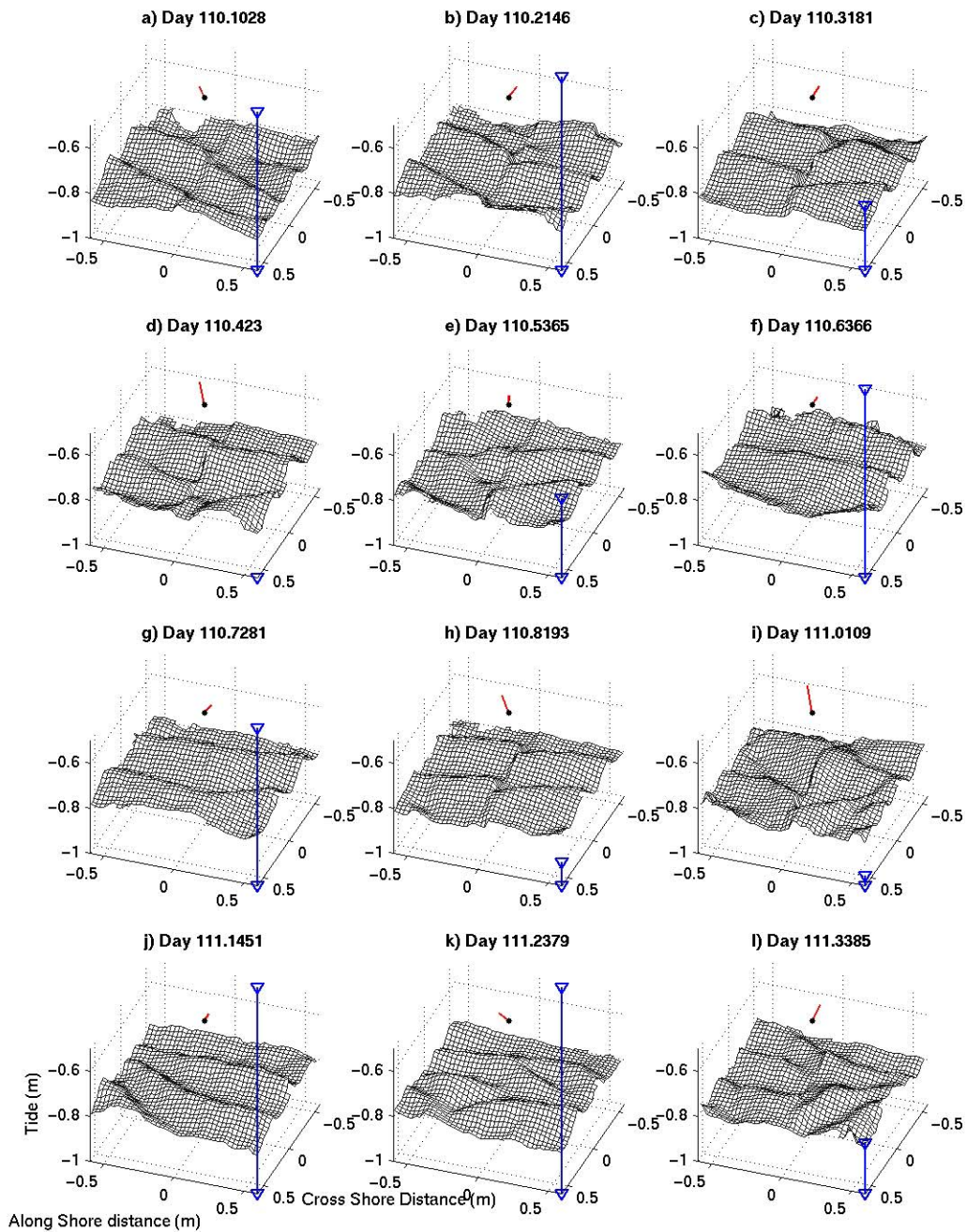
Figure 11.   Summary of altimeter grids from the highest quality data, yeardays 110-111.5. Every fourth map is shown. Lines on near sides with triangles represent relative tidal depths, and lines above bed represent vector mean currents over each sampling interval.

The mean ripple height and length are now determined. For each point along each ridge, a 5-point (two on either side) least squares fit is made, and its normal calculated. This normal is nominally perpendicular to the ridge crest, and should ideally intersect the adjacent trough at the closest possible point. To determine this, the point along the adjacent trough that the normal gets closest to is identified. A 3-point least-squares fit is made to the trough, and the intersection of this fit to the ridge normal is calculated. This intersection must fall within the same half of the map as the originating ridge point, or the point is ignored. The straight-line distance between the ridge point and this intersection is identified as the ripple half-wavelength. The ripple height is then estimated from the difference between the initial crest point and the trough intersection point.

The same calculation is repeated for each point along each ridge, for the trough on each side, and in reciprocal for each point of each trough. Each ripple height and half-wavelength for each half of the map are accumulated for statistical analysis.

The gridded bed height maps in figure 11 clearly show that the time required to completely sample the map area causes a central discontinuity due to the change in position of the bedforms over the half map time span. However, it is also expected that the ripples are continuously and uniformly moving while the SAA is incrementing along-shore away from the centerline. The result of this movement is a chevron-shaped feature that is open toward the direction of movement. Correcting for this finite data sampling time greatly improved accuracy of ripple characteristics and allowed ripple migration speed and orientation to be found.

To do this, a 2nd- order polynomial fit was computed for the inner 5 points of each ridge or trough line found within each half map. The intersection of this fit with the centerline (the y-axis intercept) was calculated and the difference taken between intercepts of corresponding features. This difference represents the distance each feature travels (d) in the time it takes to map one-half of the map. Since only the first and last data point of the map were time-tagged, this time was assumed to be half of the total mapping time for that map ($t/2$). Averaging the differences between all features that

25

could be correlated, ripple propagation speed $V_r=2d/t$ was calculated for each map where ripples were present and completely distinguishable.

Assuming that the ripple propagation speed for each map was uniform across the sample domain and constant though the sample time, a linear correction can now be applied to the ripple ridges and troughs on each half of the map, ranging from zero correction at the centerline of the first half mapped, to a distance cross-shore of *-2d* at the far side of the second half, against the direction of propagation. Examples of corrected ridge and trough lines are shown in Figure 10b overlain on the original morphology contour map.

These new sample-time corrected maps have been used to re-calculate ripple height and half-wavelength, using the same method applied to the uncorrected maps. From these revised feature positions, an average least-squares linear fit is also calculated for each crest and trough, still separate for each half to avoid additional central offset errors, to represent a mean ripple orientation. The orthogonal to the mean ripple crest orientation is assumed to be the true propagation direction, as any deviation from an orthogonal propagation would result in a re-orientation of the ripples [*Boyd et al.*, 1988, *Traykovski et al.*, 1999].

The time series of yearday 110-111.5 cases 1 and 2 for one analysis half's ripple heights and half-wavelengths are shown in figure 12. The ripple heights and half-wavelengths display very little noticeable change in mean or standard deviation with the orientation corrections. This is an expected result because while the positions of the crests and troughs were altered, the height and irregularity of the ripples are not. Since estimating ripple crest orientation and shape was the motivation behind this correction, figure 10 demonstrates the significant effect this correction has on the ripples, aligning the crests more linearly and shore-parallel, and eliminating the chevron shape caused by the ripple migration.
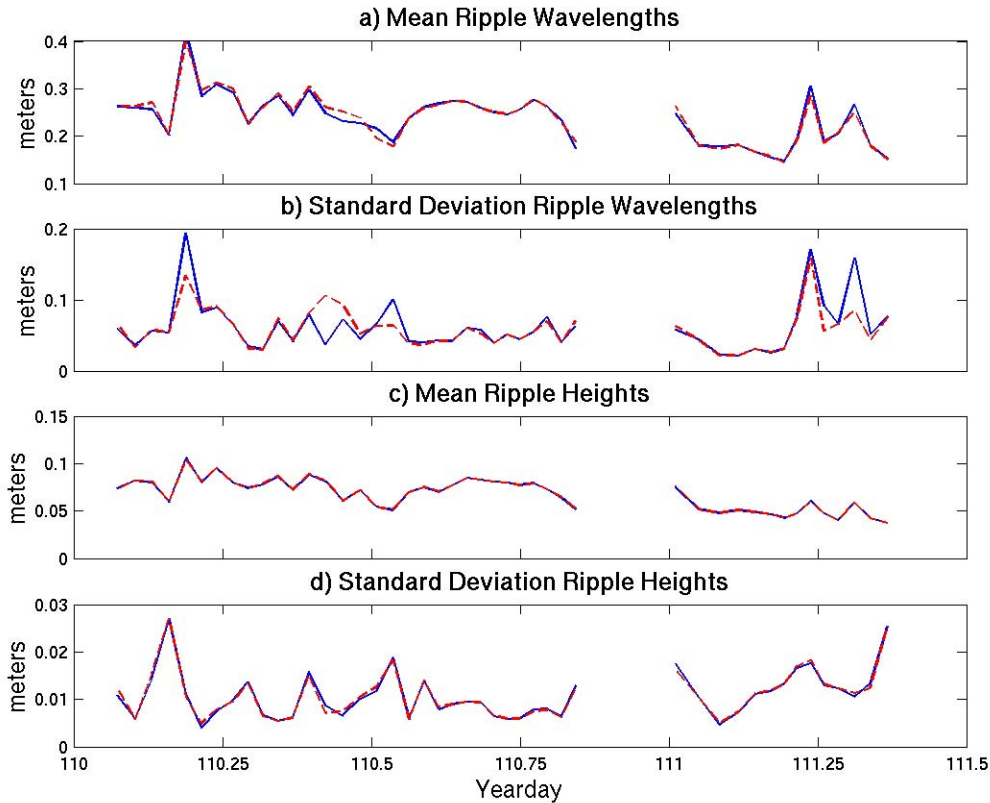
Figure 12. Effect of ripple correction on ripple height and ripple length. (A) Uncorrected (solid) and corrected (dashed) mean ripple wavelengths. (B) RMS ripple wavelength. (C) Mean ripple heights. (D) RMS ripple heights.

This analysis provides mean ripple height, half-wavelength, propagation speed, and crest orientation from each sampling-corrected map. Histograms of these variables sampled from each map have nominally Gaussian distributions with little spread (figure 13). Some, however, have a broader distribution, as is shown in figure 14. In this type of distribution, the ripple heights, but more commonly the wavelengths, have a more bi-modal distribution (figure 14d,e), resulting from a steeper, more closely spaced crest-trough interval on the leading side of the ripples than on the trailing side. Figure 15 demonstrates yet another type of histogram observed in which the irregular distribution is not easily characterized, with a broader distribution and many outlying points from the central group. This is the same SAA map shown in figure 11e. These irregular distributions were found in maps with more irregular, short-crested or bifurcated ripples,

27

and were the result of the angles of the ripple normal lines near bifurcations and terminations to the dominant ripple alignment.
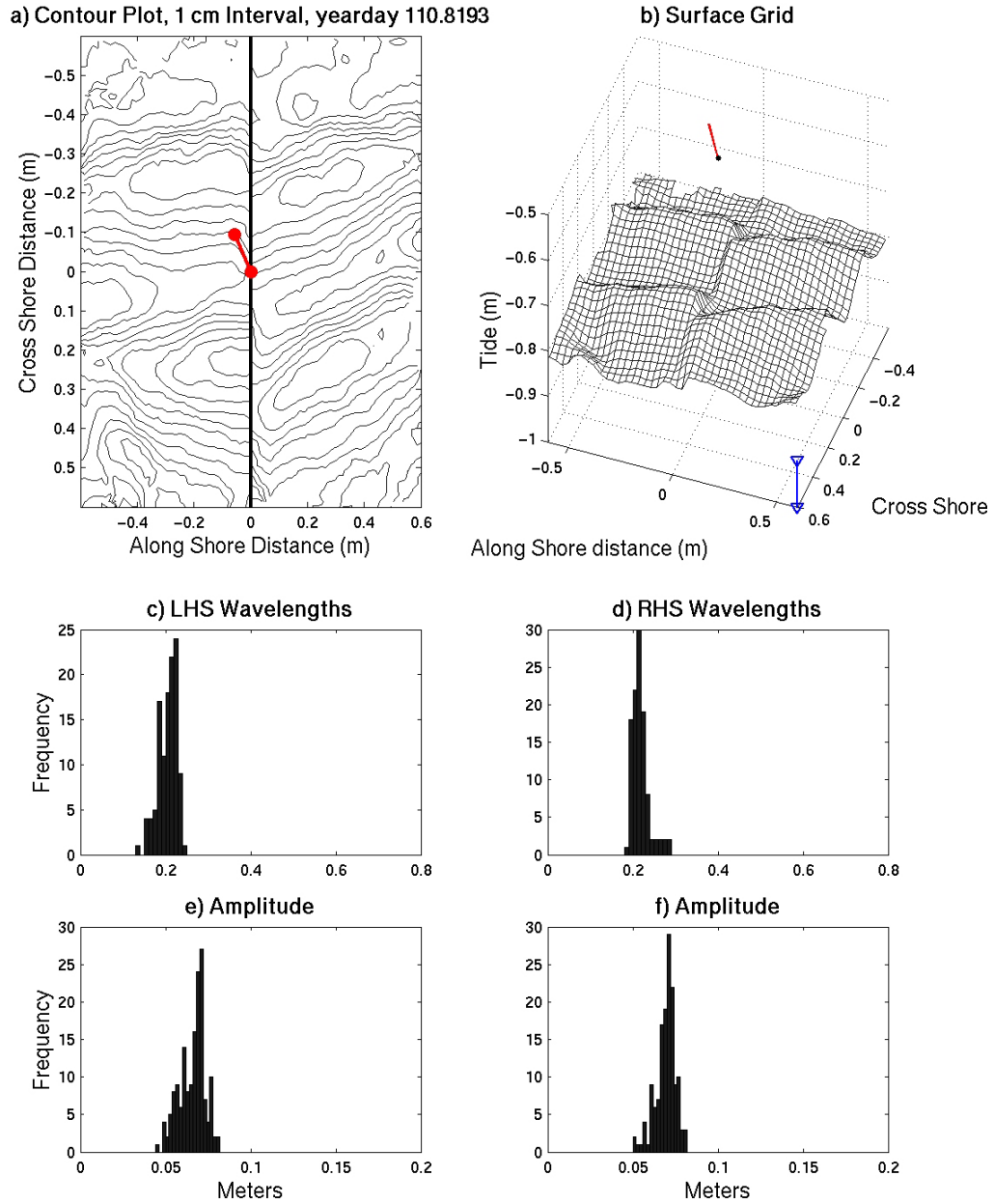
Figure 13. Typical, well-behaved ripple height and length distributions: yearday 110.819 (A) Contour map. (B) 3D mesh depiction of same. (C-F) Histograms of Ripple Height and Wavelengths derived from this map.
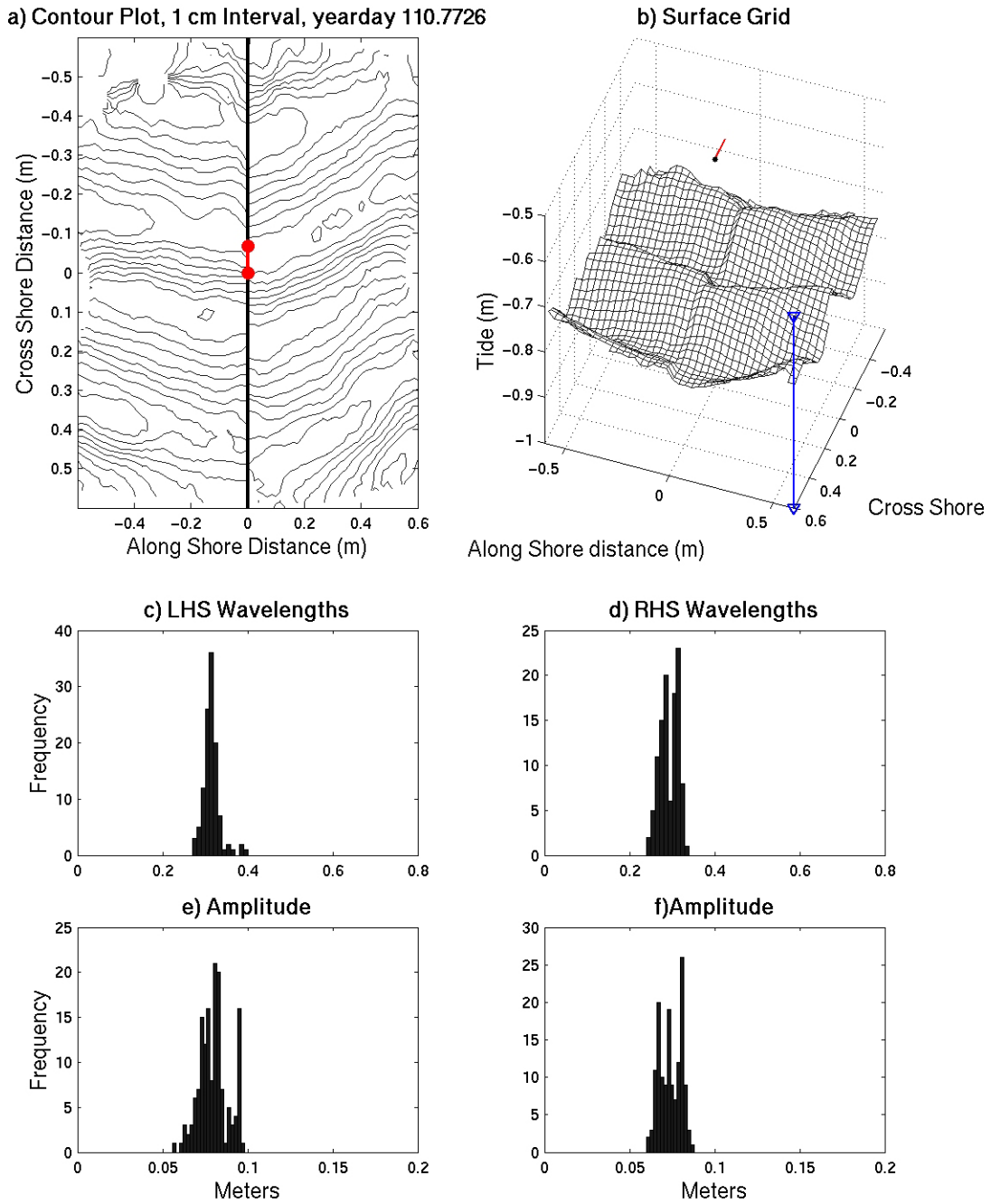
Figure 14. Same as Figure 13, but showing a broader, bimodal distribution of ripple lengths, indicative of the asymmetric ripples, on yearday 110.773.
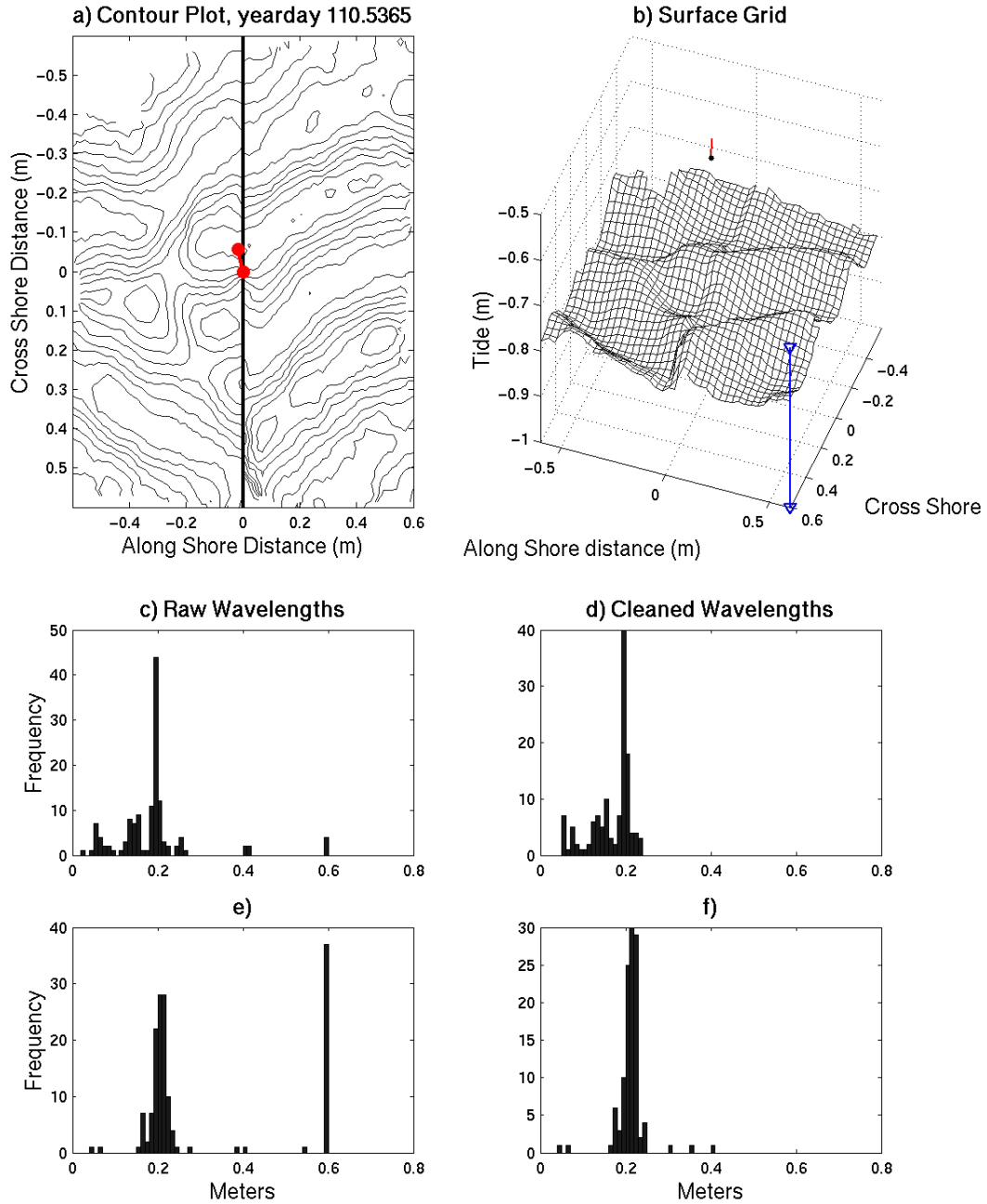
Figure 15. (A) Contour map of bifurcating ripples on yearday 110.537. (B) 3D mesh depiction of same. (C-F) Its accompanying histograms, showing broad distribution and many outlying ripple wavelengths due to a sharp angle of ripple crest normals near the bifurcation to the mean crest orientation. The second set of accompanying histograms has eliminated points greater than 2 standard deviations beyond the mean.

To attempt to account for this error, two steps were taken. First, the outliers were determined to result from irregularities in the evaluated crest and trough positions, as would appear near the bifurcation in 15a. The linear fit surrounding these irregularities produced a normal that projected at a very sharp angle to the mean ripple orientation. This resulted in very unrepresentative wavelengths. Outliers were only found in wavelength histograms, since such irregularities do not exist in height along the ripple crests or troughs. This problem was corrected by eliminating from the calculations all data points greater than two standard deviations from the mean. The result of this adjustment can be seen in figures 15d and 15f. The standard deviation is significantly reduced, especially for the cases with larger means and deviations. Smaller amplitude ripples were generally much more regularly shaped and did not show as great an effect.

The second correction made to try to understand the wavelength distribution irregularities was to subjectively classify the ripples. Using the ripple categories of *Boyd et al.* [1988] (figure 16), a ripple type was attached to each map's statistics. These categories appear as a separate variable, distinguished by marker shape, and serve to try and correlate ripple characteristics to ripple type. The ripple types, markers, and their dynamic relevance are described below.

a.   *Long-Crested*

Orbital ripples that are solely under the influence of regular, oscillatory wave motion are classified as Long-Crested and labeled with a blue square. Symmetric cross-sectional form and long, continuous, straight crests identify a ripple field as Long-Crested (see figure 11g). Long-Crested ripples may migrate minimally, and indicate a relative steady state. They often have very narrow distributions in both height and wavelength.

31
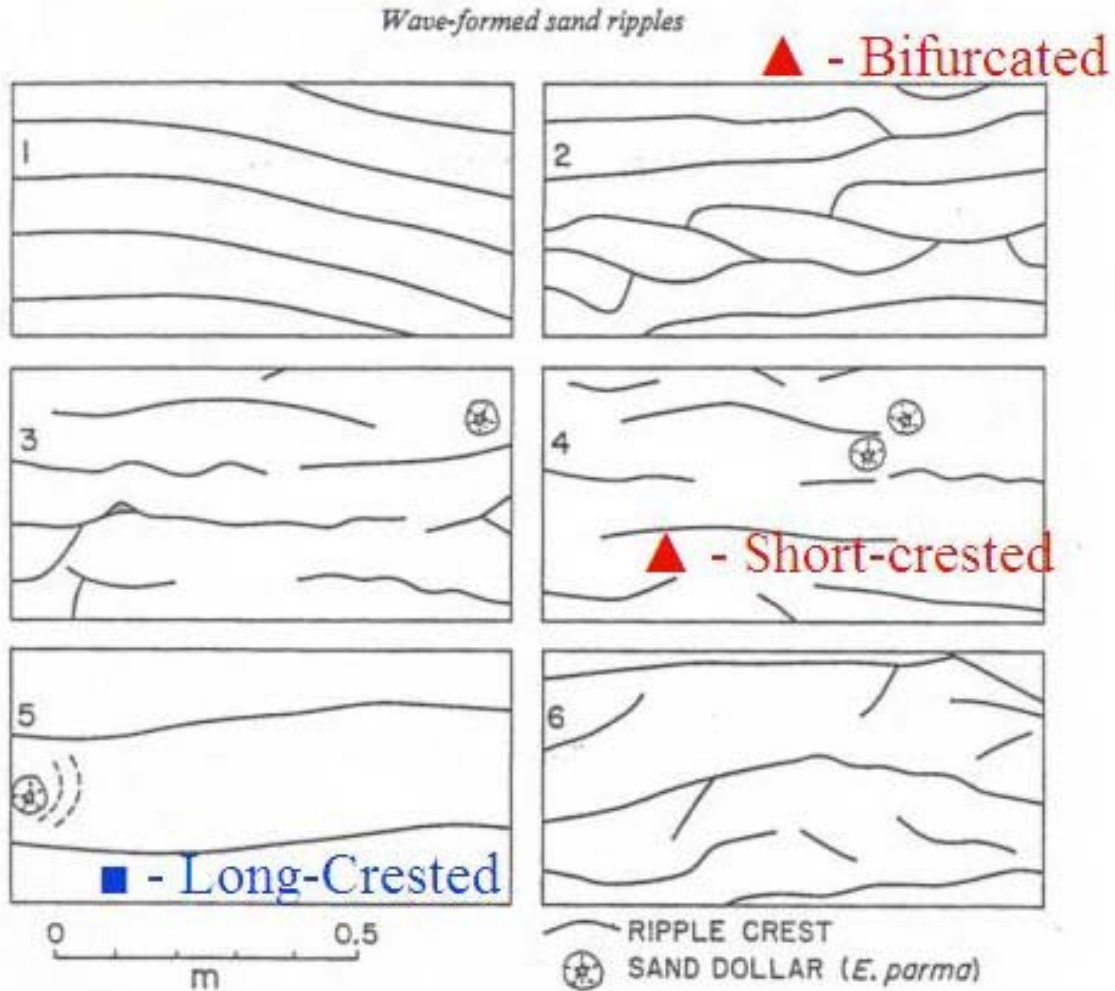
Figure 16. Ripple types observed and figure symbols used to depict each. (After *Boyd et al.,* [1988], figure 6).

b.   *Short-Crested*

When a change in the wave environment occurs, whether wave height, period, or incidence direction, ripples become Short-Crested or Bifurcated. Discontinuous, misaligned crests characterize Short-Crested ripples (figure 11k), while Bifurcated ripples are those whose crests are split into two (figure 11e). Because of the small spatial coverage of the SAA, Short-Crested and Bifurcated ripples are often confused or difficult to distinguish, and are therefore classified jointly at Short-Crested and labeled with a red triangle. Widely spread ripple length and height distributions are often associated with Short-Crested ripple types.

c. *Asymmetric*

Asymmetric ripples occur when a mean current or asymmetry is introduced to the wave field [*Clifton and Dingler,* 1984]. This mean current may be the result of longshore transport, rip circulation, undertow, or longer time scale motions such as infragravity waves, edge waves, or tides. As the name indicates, the form of an Asymmetric ripple is characterized by a shorter, steeper face to the lee of the crest than on the facing side (figure 11f, 15). Numerical indications of Asymmetric ripples are a bi-modal distribution in ripple height, length, or both. When subjective visual scrutiny of the map agrees with an asymmetric form, the ripple field is labeled Asymmetric. These ripples are shown on future diagrams with a green circle.

d. *Short-crested and Asymmetric*

Mean currents can exert an influence on the flow field in steady or changing conditions. When evidence exists for mean currents during a change in wave climate (wide, bi-modal distribution), ripples often appear Short-Crested and Asymmetric (figure 11l). Such ripples are labeled with a black diamond.

8. **Secondary Ripple Geometry Measurements**

On altimeter maps where ridges and troughs cannot be traced completely across the map, but a single cross-shore section captures a full ripple wavelength, a single estimate of ripple height and wavelength is obtained by locating the local minima/maxima in the cross-shore profile. In this manner, ripple geometry estimates were obtained as early as yearday 106 and as late as yearday 118. Ripple half-wavelength was estimated as the mean of the crest-trough distances, and the ripple height was the mean of the crest-to-trough altimeter height differences. It should be noted that where there are no altimeter ripple measurements prior to yearday 110, the maps are of poor quality (figure 9). The data following yearday 112, however, has much more high quality data, but SAA maps show a flat bed, indicating sheet flow conditions. Flat bed conditions are marked on time series as solid bars where observed.

Backscatter profiles from the BCDV center beam have also been used to supplement the altimeter map time series. The BCDV provides continuous backscatter measurements at a single location within the SAA map domain, allowing rapidly changing features to be measured with up to 20 Hz resolution vs. the 30-60 minute mapping time needed by the scanned altimeter. The acoustic hardware and processing is very similar to the SAA, and a similar bed-finding algorithm has been used to process the backscatter data by identifying a backscatter peak beyond a pre-defined range (to minimize bubble saturation) as the bed. The most significant difference is that the BCDV-based bed elevations have vertical resolution reduced to 1cm vs. 0.25 cm, while the temporal resolution in this analysis is 30 seconds. By tracing the bottom, each successive minimum and maximum in bottom detection represents the trough and crest of each successive ripple as it migrates past the BCDV footprint. Ripple heights were estimated by finding the difference between each local minima and maxima. The time of the sample is estimated to be the midpoint in time between the minimum and maximum. The resulting bed height time series has been used to estimate local ripple height, η, and the temporal wavelength t is used with a constant ripple half-wavelength, $\lambda/2$, of 20 cm to approximate ripple migration speed, $v=\lambda/2t$.

Ripple migration and crest orientation are impossible to determine from the maps where the ripple geometry was determined from a single measurement location. While cross-shore profile measurements extend the breadth of forcing during which ripple geometry is known, migration and transport analysis cannot include them because of the lack of measurement continuity in time. BCDV estimated ripple migration speeds, on the other hand, are used for comparison with ripple migration speeds obtained by the centerline discontinuity offset of the fully resolved altimeter maps.

Armed with these many statistical characteristics of the ripple fields, they are now analyzed, along with the dynamic forcing, to evaluate model predictions of ripple geometry and sediment transport calculations.

III. RESULTS AND ANALYSIS

A. OBSERVATIONS

1. General Evolution

The evolution of the significant wave height (H_s) throughout the experiment is shown in figure 17a, computed from a wave buoy moored offshore of the RIPEX site in 17 meters of water, and from the capacitance wave staff mounted on the array with $H_s = 2\sqrt{2}\eta_{rms}$, where η_{rms} is the standard deviation of the surface elevation. Prior to yearday 111, the significant wave height at the array increased due to shoaling, and matched the offshore H_s very closely except when altered by low tides that could not be resolved by the wave staff.

Beginning on yearday 111, however, the significant wave heights began to separate as the wave energy that reached the boundary layer array became saturated with the surf zone extending seaward of the array. The blow up in time in figure 17c shows that during high tides on yeardays 110 and 111, the waves were observed to break shoreward of the BL array. Before and after this time, however, the observed breakers were always at or seaward of the array, allowing for the dissipation of wave breaking to saturate the nearshore wave energy, especially in the very high energy of the storm on yearday 111/112. The breaker locations were obtained from 20 minute time lapse video images overlooking the instrumented shoal / rip channel cell.

Also at this time, the tidal ranges began to increase, as shown in figure 17b, and consequently, less of each increasingly shallower low tide could be resolved by the wave staff. Evidence of the wave staff's difficulty in handling low water depths can be seen in the overlain mean surface elevation (η_{avg}) in figure 17b. The wave wire means follow the tide very well until the means fall below ~0.3 meters. This corresponds with the lowest exposed portion of the wave staff at 0.24 meters, and times where the wave wire's η_{avg} was below 0.25m for greater than 10% of the time have been blanked from all further velocity and surface elevation data taken from the BL array.
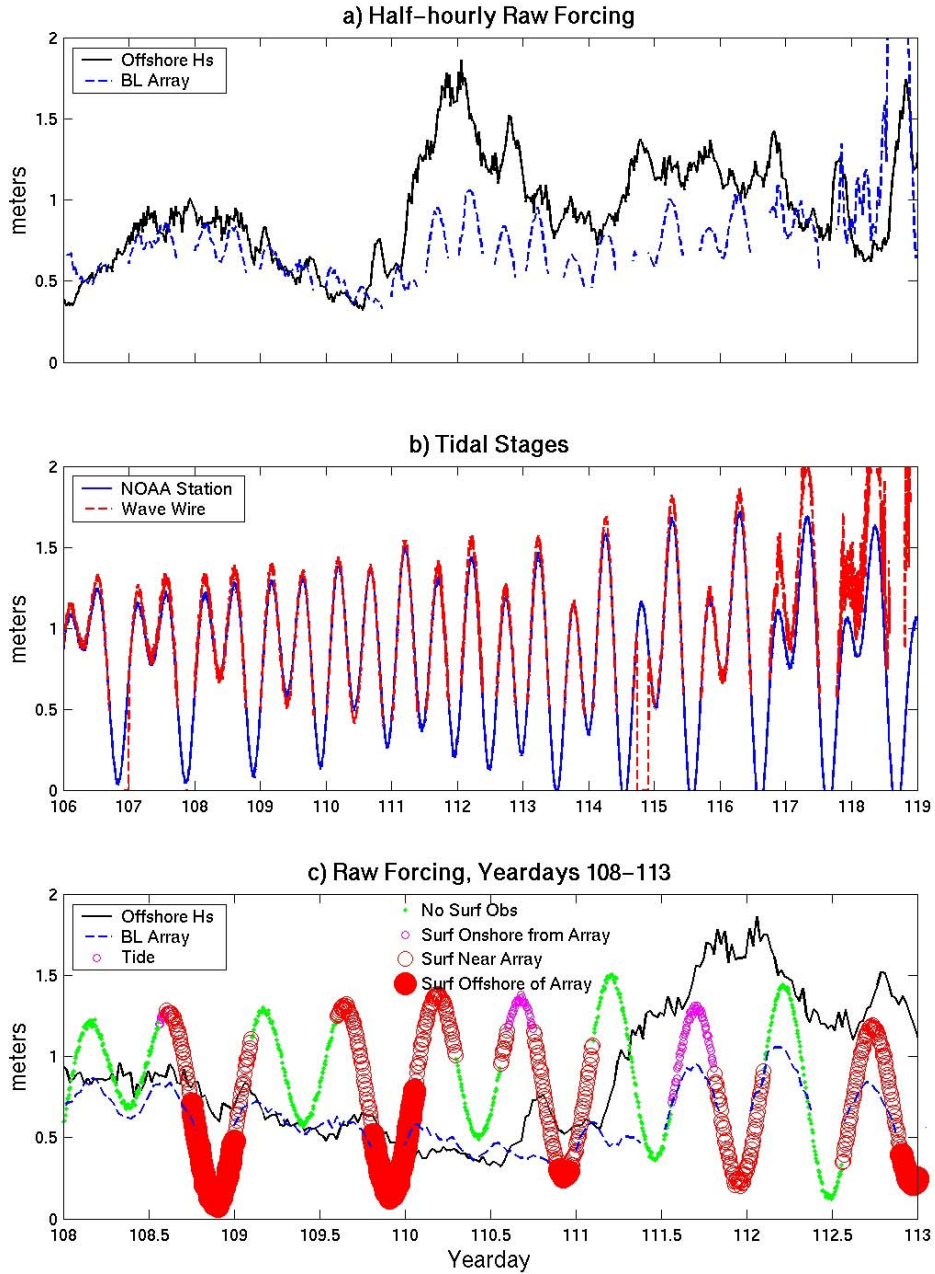
Figure 17. (A) Offshore significant wave heights (solid) and those measured by the boundary layer array (dashed) through the deployment. (B) Tidal signal as measured at Monterey Pier (solid) and the wave wire (dashed). (C) Blow up in time of offshore Hs (solid), wave wire Hs (dashed), and tidal signal (circles). Tide markers are indexed by analysis of 20 minute mean video images which show mean breaker position relative to the BL array.

2.   Ripple Evolution

In the interval from yearday 109 to 111.5, when regular bedforms were observed in the SAA maps, the ripple analysis described above was conducted for each map. Statistics calculated included ripple height, ripple length, ripple migration speed, and mean ripple crest orientation. Because of the separate analysis procedures between the halves described in chapter 2, ripple geometry data is presented twice for each map; once for each half. Ripple migration and crest orientation are each summarized as a single value for each map. Because of the wide temporal spacing of the measurements obtained from single cross-shore profiles, they will not be discussed in this portion of the analysis.

Ripple height, wavelength, and steepness are presented in figure 18, along with NOAA tide data measured at Monterey Wharf, approximately 2 km away, and offshore significant wave height for reference. The central symbol represents the mean and is coded according to the ripple type identification described in section 2-B-7. The length of the bars represents the standard deviation of properties within each map. Although not statistically significant because each sample was not independent and random, the standard deviation of ripple height and wavelength is presented to give the reader an indication of the spread of the data, derived from each corrected map.

To first order, both the heights and wavelengths are modulated by the tides on yearday 110, with smaller ripples at low tide and larger ripples at high tide. Because both vary together, steepness, calculated here from the means, remains fairly constant, near the 0.15 value characteristic of orbital ripples. The spread of ripple height decreases through yearday 110 as the significant wave height decreases, allowing for more regular wave motion to dominate and long-crested ripple types to prevail during the second high tide of day 110.
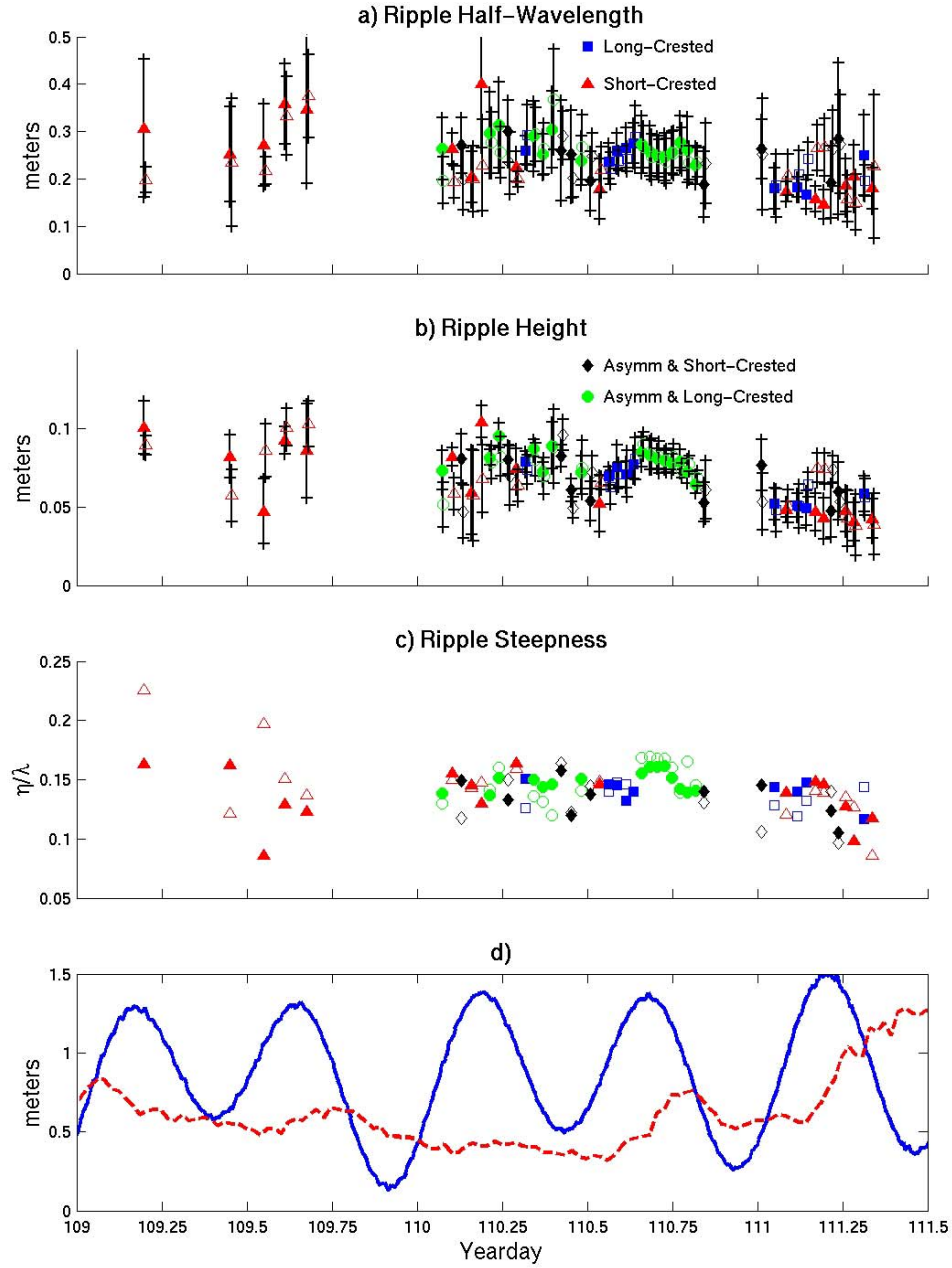
Figure 18. (A) Wavelength, (B) Height, and (C) Steepness of ripples measured by the SAA. Central symbols are mean values, bars represent standard deviation. Ripple types are labeled as follows: Long-crested (blue square), Short-crested (red triangle), Asymmetric long-crested (green circle), Asymmetric short-crested (black diamond). Open symbols are from the LHS, closed symbols are from the RHS. (D) Tide and Offshore Hs for reference.

Beginning at the start of yearday 111, the ripples become shorter in both height and length, the standard deviation becomes larger, and short-crested ripple types begin to dominate (see also figure 11i-l). The ripple steepness also begins to decrease, indicating a change from orbital to anorbital ripple forcing. SAA and BL array coverage during this low tide was poor, and figure 18d shows a brief increase in the offshore forcing that coincides with this low tide. Whether this sudden change is because of a disturbance of the bedforms during the very shallow low tide, or because of the increase in incident wave energy from the approaching storm is uncertain, but it is evident that something caused disruption to the ripples just prior to day 111.

A time series of ripple migration speeds and mean crest orientation in figure 19, shows that migration is primarily onshore (negative) but variable until near the end of yearday 110. Estimated BCDV ripple migration rates are also plotted in figure 19a, and show migration speeds which are much less variable at the beginning of yearday 110. In animations of the SAA maps, long, straight-crested ripples can be observed slowly and steadily moving onshore during the second high tide of yearday 110. This high tide coincides with the very lowest offshore significant wave heights, as well as with the lowest mean bottom currents (figure 19c). The fastest migration rates are seen at the low tides, where the shallower water creates a larger cross-shore gradient of momentum flux of the waves over the shoal, and increases the mean shoreward current and the wave/bore forcing. Nearshore theory for straight simple beaches would suggest that the near-bottom mean velocity should be seaward to counter the shoreward mass flux of the incident waves. In the presence of rip channels, however, figure 19c shows that two-minute mean bottom velocity is almost entirely shoreward. This is discussed in greater detail in chapter 4. At the high tide, a corresponding minimum in mean bottom current occurs, and the ripple migration stalls or reverses, as seen at the high tides on yeardays 110 and 111. In the absence of a seaward mean bottom current on day 111, the observed seaward ripple migration may be questionable, and may be an artifact of ripple reorganization or a result of incident wave reflection. This is also discussed further in chapter 4.
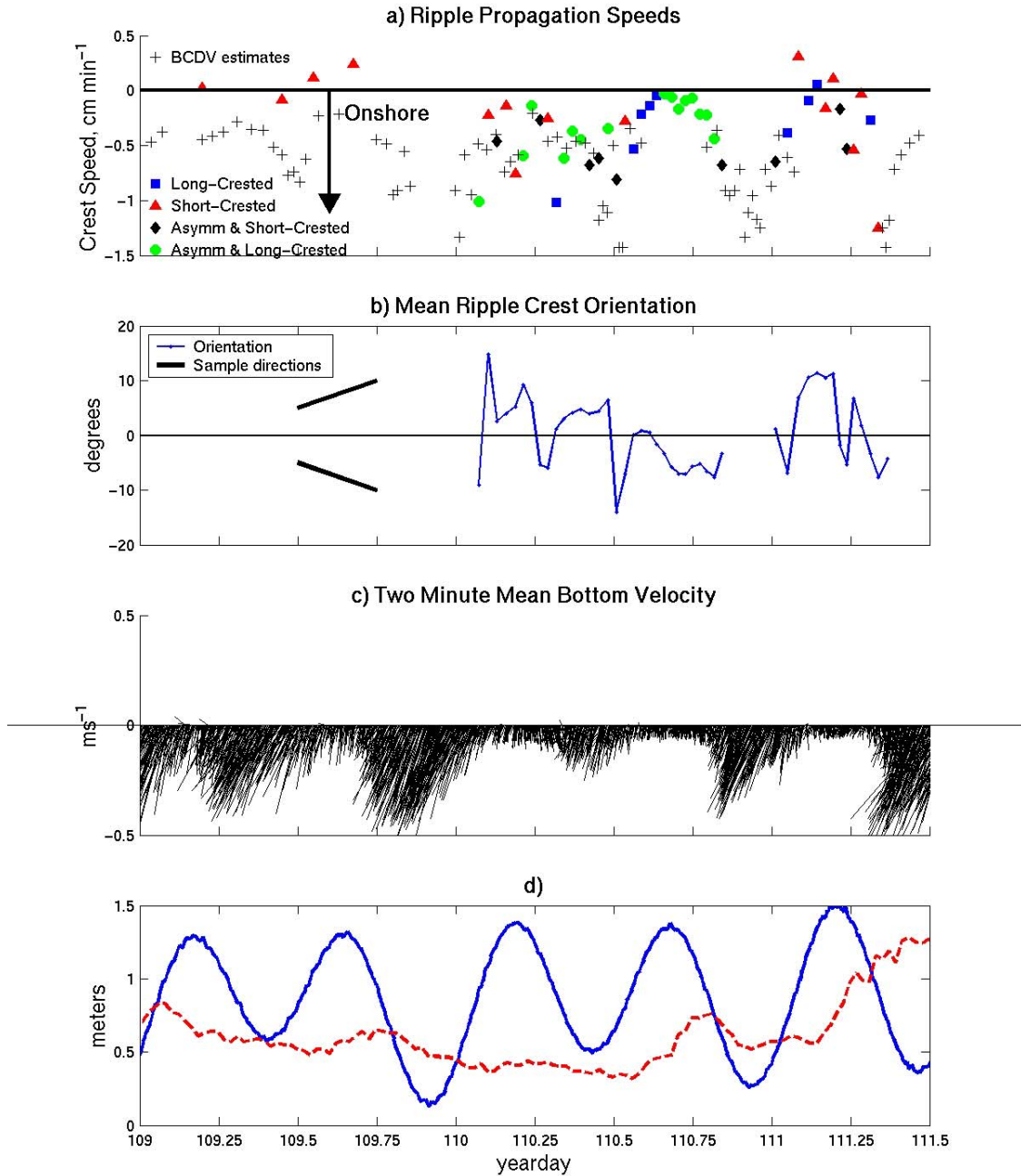
Figure 19. (A) Ripple migration velocities. BCDV estimates are assumed to be onshore (negative). See figure 18 for symbol explanations (B) Mean crest orientations, with sample orientation indicators shown at yearday 109.5. (C) Mean two minute bottom current vectors. (D) Tide and Offshore Hs for reference. Negative velocities are onshore, and crest orientations are in degrees.
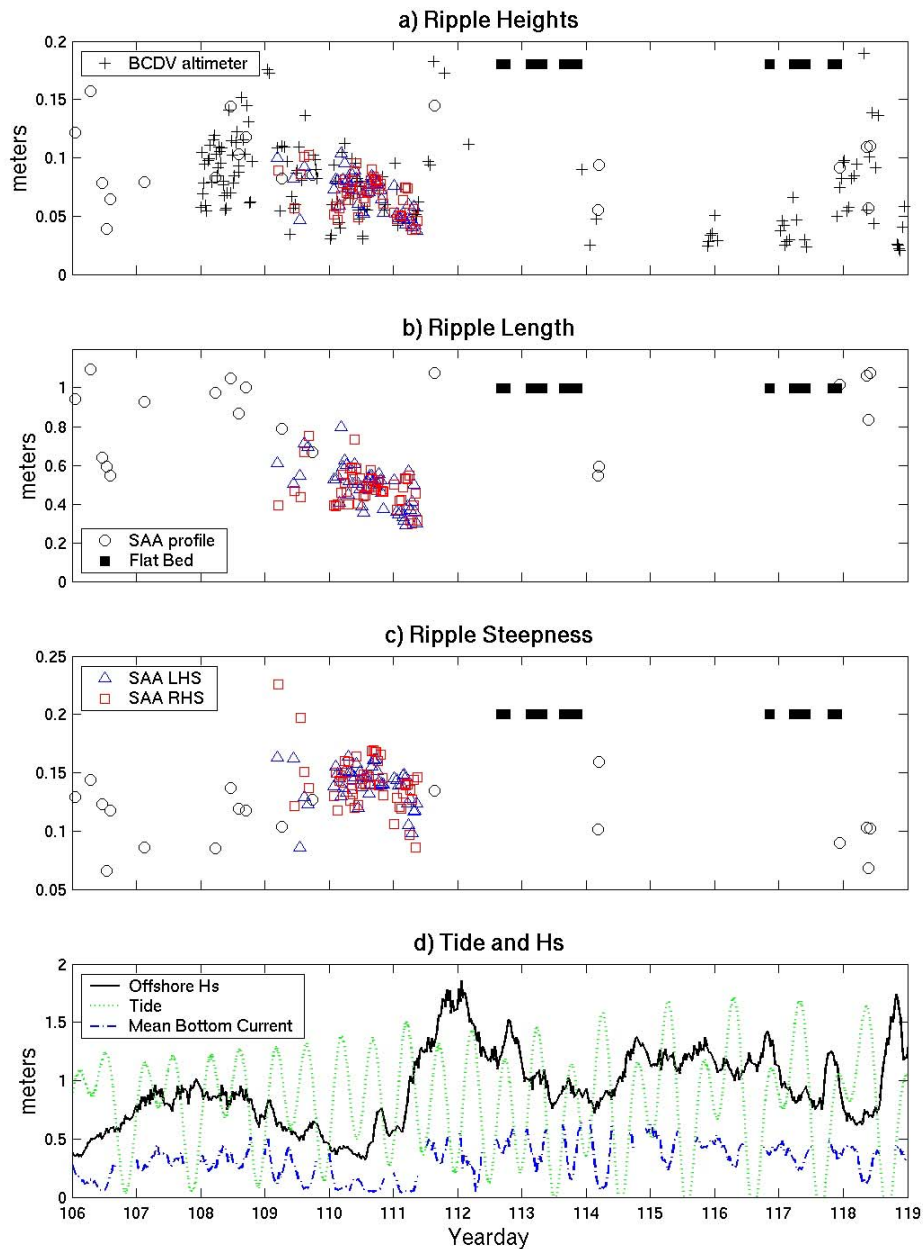
Figure 20. Summary of measured ripple parameters over the length of the deployment. (A) Ripple Height, (B) Ripple Wavelength, and (C) Ripple Steepness. Open red squares and blue triangles are those measurements obtained from full SAA map analysis, right hand side (RHS) and left hand side (LHS), respectively. Open black circles were obtained from single SAA profiles, and black '+' were obtained from the BCDV altimeter. Solid black bars represent times where the bed was observed to be flat. (D) Offshore Hs, mean current magnitude, and tide height.

Mean ripple orientation in Figure 19b does not display any characteristic shift with the change in forcing or tide. A slight shift occurs over day 110 from moderately left of shore-normal to slightly right of shore-normal migration, but no significant perturbations from shore-parallel crest orientation occur in the time range of fully resolvable ripples.

A time series of ripple observations over the entire deployment and using every observation technique is shown in figure 20. Where Hs is higher, mean bottom currents also tend to be stronger, and ripples are correspondingly high. Times marked as having observed flat bed conditions roughly correspond to those where mean bottom current and H_s are highest, possibly indicating some threshold value of one or both above which ripples are eliminated. Both quantities decrease briefly on yearday 114 and again on yeardays 116-118, corresponding to the re-appearance of ripples in the BCDV and/or SAA data.

From measured or calculated ripple characteristics, *Traykovski et al.* [1999] calculated mass sediment transport due to ripple migration as

$$M_{ripple}(t) = \int_{ripple} \rho_s (1-\varepsilon)\xi V_m dt \qquad (4)$$

where ε is the sediment porosity ($\varepsilon \cong 0.35$ for sand-sized sediments, *Sleath* [1984]), ζ is the instantaneous ripple height, and V_m is the rate of ripple migration velocity. Assuming a sinusoidal ripple profile, equation 4 can be simplified as

$$q_r = \frac{1}{2}\rho_s(1-\varepsilon)\eta\lambda V_m + q_0. \quad (5)$$

The underlying assumptions used were that during a short interval, the ripples migrate with constant velocity, perpendicular to the ripple crest, the ripples maintain their form, and that the entire volume of the ripple migrates. In the case of uni-directional flows (desert dune fields, river beds) where sediments are incrementally deposited (onshore transport) as ripples override one another, then a q_0 is added to account for the mean bed accretion due to ripple deposition. Similar arguments could be made for asymmetric ripples that occur under combined wave- and current-dominated flows, but in the absence of specific evidence of accretion, q_0 is generally set to zero.
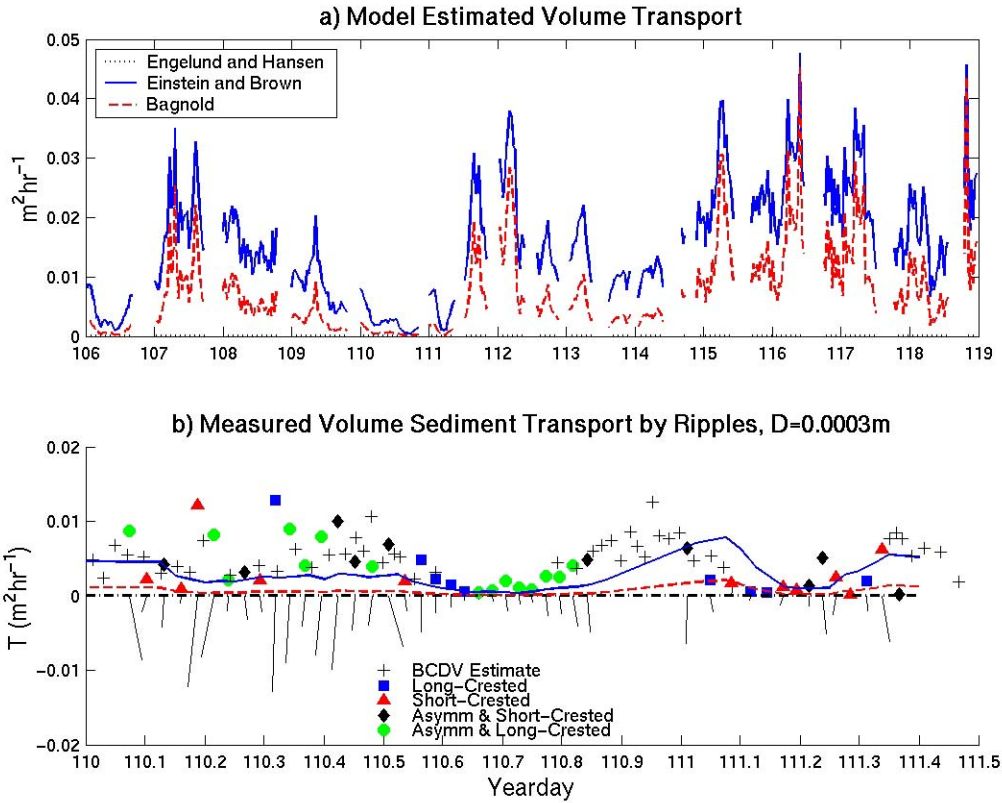
Figure 21. Model predicted volume sediment transport (A) for the entire deployment and (B) for fully-resolved SAA maps on yeardays 110-111.5. Symbols and lines indicate magnitude only. See figure 18 for symbol explanation. Vectors represent direction, with positive offshore. Transport units are m^3/hour per meter beach width, or m^2/hour.

Volume sediment transport by ripple migration given by $q_v=\frac{1}{2}\eta\lambda V_m$ is shown in figure 21 compared to model predictions, which will be discussed in chapter 4. Because variation in ripple migration is large (from zero up to 1 m/hr) in this study compared to observed changes in ripple heights and wavelengths, transport is dominated by the variation in ripple migration rate. Thus, ripple transport rates are at a minimum during high tides because of the low migration rates. BCDV "rough" estimates are also included, again using a constant ripple wavelength of 40cm. These measurements match those taken from fully resolved SAA maps well, again validating both methods of transport measurement.

43

3.   Orbital displacements and velocities

To further understand the variation in ripple geometry and migration, forcing by waves and currents are calculated and examined. Diagnostic models that attempt to describe ripple geometry based on sediment and wave forcing characteristics typically use parameters such as sediment grain size, wave orbital diameter, wave orbital velocity, and Shields number and mobility number, which implicitly include combinations of these parameters. Most of these models are based on sinusoidal, narrow-banded laboratory observations. In the field, however, wave and current forcing is much more irregular, with broad banded swell and wind waves, infragravity forcing, and directional spreading common features of the wave field [*Bagnold*,1946, *Miller and Komar*,1980a]. Irregular wave forcing causes more complex ripple patterns to be observed than in controlled laboratory experiments [*Boyd et al*., 1988, *Hay and Wilson,* 1994, *Traykovski et al*., 1999], and ripple geometry is less well defined in relation to the forcing. Many laboratory-based models consider ripples that form from a flat bed under increased forcing [*Bagnold*, 1946, *Miller and Komar,* 1980a]. As forcing diminishes again below the critical threshold, ripples do not disappear but rather remain as relicts of the previous conditions. New methods are required in both the ripple geometry prediction process and in measuring wave orbital characteristics in order to capture fully the complexities of a realistic wave field.

The first parameterization of forcing was the spectral variance of bottom velocity in the range 0.05-1.0 Hz, which is representative of the incident swell energy. This was obtained from the lowest EMCM approximately 30 cm above the bed in half hour intervals though the entire 14-day deployment. Because the EMCM was mounted near the level of the wave wire base, it emerged from the water at approximately the same time as the wave wire bottomed out. Bottom velocity measurements were therefore considered invalid at the same times that the wave wire data was considered invalid, as described above. By this method, variances of orbital displacement, orbital velocity, and acceleration were calculated.

Figure 22 shows a summary of bottom orbital velocities calculated by the spectral variance method. Bottom orbital velocity from the full spectrum is shown together with

the band-passed velocities, and the difference between the two represents the contribution from very low frequency and infragravity motions. The Infragravity contribution is proportional to the total wave energy, however the period from yeardays 110-111.5 is characterized by very little infragravity energy while the remainder of the deployment showed strong increases in infragravity energy with wave height.
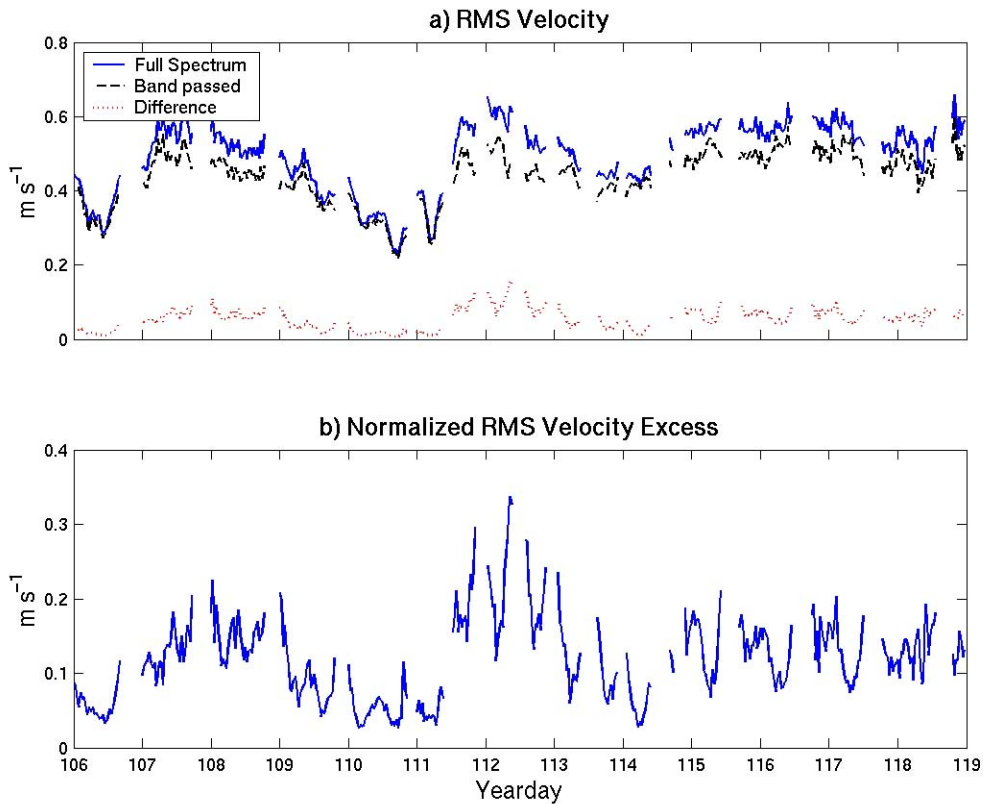
Figure 22. (A) RMS orbital velocities from full-spectrum, swell band, and their difference. Difference indicates contribution of infragravity energy. (B) The ratio of infragravity energy to swell band energy.

A second trial method examined wave forcing by detecting peaks in high-pass filtered displacement and velocity vectors. Half hour sections of raw bottom velocity data were Fast-Fourier Transformed, and frequencies below 0.05 Hz were filtered out. Each remaining complex coefficient was multiplied by $1/-i\omega$ to perform a frequency-domain integration, resulting in a filtered transform of the displacements. The filtered velocity and displacement coefficients were then inverse-transformed to create a new

high-pass filtered time series of velocity and orbital displacement. Vector maxima between cross-shore zero crossings were then identified and recorded for both the raw and filtered time series. From the identified vector peaks, a two-dimensional PDF was created for each time interval and analyzed in comparison to the scalar variances of cross-shore properties in order to capture the spatial variation of orbital motions and contrast.
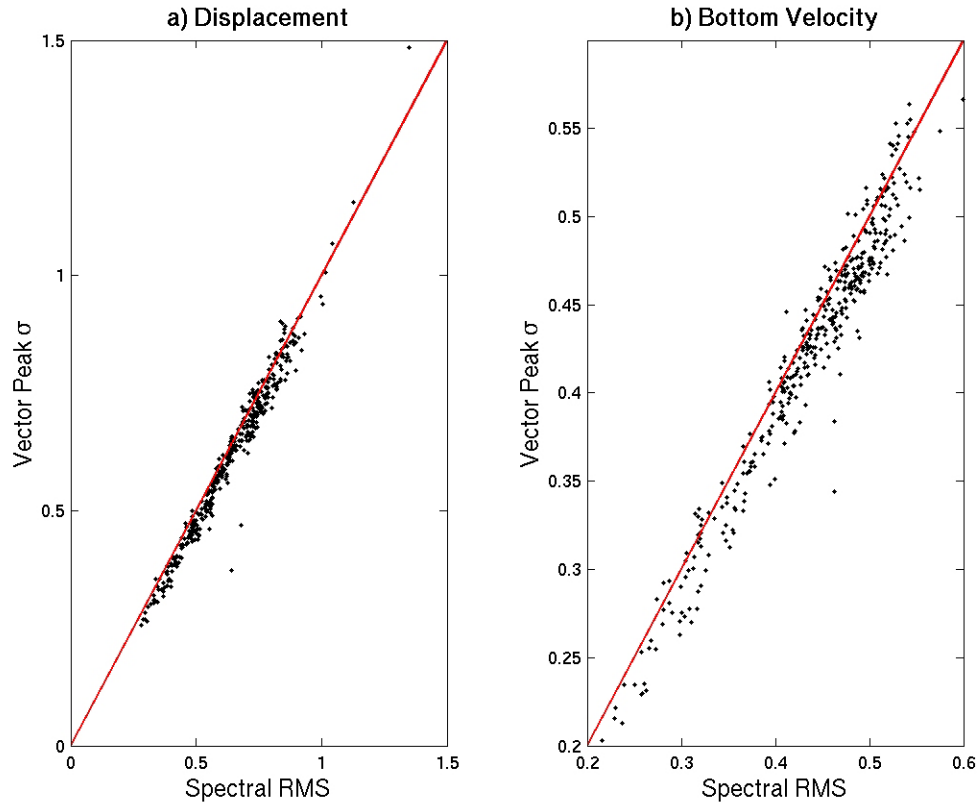
Figure 23. Comparisons of Spectral RMS wave orbital displacements and velocities to standard deviation of the filtered time series, as estimated by detected peak PDF's. (A) Orbital Displacement. (B) Orbital Bottom Velocity.

The validity of the peak detection process is verified in figure 23, which shows a regression of significant bottom orbital velocities and displacements using the spectral variance estimate against the same estimate using peak detection. From the statistical relation $\sigma = A/\sqrt{2}$ where A is the amplitude of a sinusoidal signal, the means of the velocity and displacement peaks were divided by $\sqrt{2}$ to obtain the standard deviation

estimates, or the significant orbital velocities and displacements. Figure 23 shows that there is very good agreement between the estimates.

B.   MODEL EVALUATION

1.   Ripple Predictors

Ripple geometry has been empirically linked to wave and current forcing in an effort to predict ripple geometry and relate its effect on bottom roughness. Three such studies examined ripple characteristics under wave-dominated conditions in the field and have proven to be robust under a variety of conditions.

To empirically derive ripple geometry from the forcing, *Nielsen* [1981] (hereafter Nielsen) used the instantaneous Shields Parameter as a predictor, equivalently defining θ' as

$$\theta' = \frac{1}{2} f_w \psi \tag{6}$$

where f_w is the wave friction factor of and ψ is the mobility number [*Brebner*, 1980]

$$\psi = \frac{(a\omega)^2}{(s-1)gD} \tag{7}$$

a is the wave orbital semi-displacement, ω is the wave radian frequency $2\pi/T$, where T is the wave period, and $(a\omega)=u_b$ represents the near bed wave orbital velocity. *Nielsen* [1981] defined f_w using the relation of *Jonsson* [1966]:

$$f_w = \exp\left(5.213\left(\frac{2.5D}{a}\right)^{0.194} - 5.977 \right). \tag{8}$$

Despite the narrow-banded characterization in equation 7, *Nielsen* used these parameters to obtain the following ripple predictor for field conditions under what he called "irregular" waves,:

$$\frac{\lambda}{a} = \exp\left(\frac{693 - 0.37\ln^7 \psi}{1000 + 0.75\ln^8 \psi} \right) \tag{9}$$

$$\frac{\eta}{\lambda} = 0.342 - 0.34\sqrt[4]{\theta'} \tag{10}$$

$$\eta/a = 21\psi^{-1.85}, \quad \psi > 10 \tag{11a}$$

$$\eta/a = 0.275 - 0.022\sqrt{\psi}, \quad \psi < 10. \tag{11b}$$

Nielsen [1981] also suggests that ripples will begin to shear off into sheet flow around $\theta \approx 1.0$.

Grant and Madsen [1982] (hereafter Grant and Madsen) also developed a ripple predictor in terms of the skin-friction Shields number $\theta' = u^2_*/(s-1)gD$ where u_* is the shear velocity. *Grant and Madsen* [1982] determined u_* by the relation

$$u_* = \left(f_w/2\right)^{1/2} u_{bm} \tag{12}$$

where u_{bm} is the near bed wave orbital velocity. Here f_w is defined as

$$f_w = 0.08 / \left[Ker^2 2(\zeta_0)^{1/2} + Kei^2 2(\zeta_0)^{1/2} \right] \tag{13}$$

where Ker and Kei are Kelvin functions of zero order, and ζ_0 is a dimensionless roughness length

$$\zeta_0 = k_b / 30Ka\left(\frac{f_w}{2}\right)^{1/2} \tag{14}$$

$K=0.42$ is vonKarman's Constant and $k_b=2.5D$ is the sand grain roughness height. For example, θ_c, the critical Shields Number for sediment motion, is estimated by *Grant and Madsen* [1982] as $\theta_c=0.05$, or a corresponding $u_{*c}=1.51$ cm/s for D=0.28mm.

Grant and Madsen [1982] then defined the critical Shields number for ripple breakoff as

$$\theta_{bf} = 1.8\theta_c S_*^{0.6} \tag{15}$$

where $S_*=(D/4\upsilon)[(s-1)gD]^{0.5}$ is a dimensionless sediment parameter and υ is the fluid kinematic viscosity. Where $\theta_c < \theta' < \theta_{bf}$, ripples are defined as being in the equilibrium range. Once θ' exceeds θ_{bf}, ripples are in the breakoff range and are now described by a different set of equations. Grant and Madsen's ripple prediction equations are summarized in Table 2.

	Grant and Madsen [1982]	*Li et al.* [1996]
$\theta_{cr} < \theta' < \theta_{bf}$	$\eta/a = 0.22(\theta'/\theta_c)^{-0.16}$ $\lambda/\eta = 6.25(\theta'/\theta_c)^{0.04}$	$\eta/a = 0.101(\theta'/\theta_c)^{-0.16}$ $\lambda/\eta = 4.95(\theta'/\theta_c)^{0.04}$
$\theta' > \theta_{bf}$	$\eta/a = 0.48 S_*^{0.8}(\theta'/\theta_c)^{-1.5}$ $\lambda/\eta = 3.6 S_*^{-0.6}(\theta'/\theta_c)$	$\eta/a = 0.356 S_*^{0.8}(\theta'/\theta_c)^{-1.5}$ $\lambda/\eta = 3.03 S_*^{-0.6}(\theta'/\theta_c)$

Table 2. Summary of ripple geometry prediction equations of *Grant and Madsen* [1982] and *Li et al.* [1996].

Wright et al. [1986] found by manual diver measurements that ripples at Duck, NC, were under-predicted by *Nielsen* [1981] and over-predicted by *Grant and Madsen* [1982], leading *Li et al.* [1996] to propose a modification to *Grant and Madsen* [1982] that corrects for the disparity in combined-flow conditions, also summarized in Table 2.

Once formed, orbital ripples can be partially self-sustaining by enhancing the skin friction due to the additional roughness they impart on the flow. *Li et al.* [1996] suggests using the *Nielsen* [1986] estimate for the ripple-enhanced skin friction shear velocity u_{*e}

$$u_{*e} = \frac{u_*}{\left(1 - \pi\frac{\eta}{\lambda}\right)}. \tag{16}$$

This calculation can create situations where the average skin-friction shear velocity u_* is less than the critical shear velocity u_{*cr} but the ripple enhanced shear velocity u_{*e} is larger than u_{*cr}, and active orbital ripples are observed [*Li and Amos*, 1998].

Wiberg and Harris [1994] (hereafter Wiberg and Harris) described a third ripple geometry predictor. This model, instead of using an instantaneous Shields Number, requires only the near bed wave orbital diameter $d_o=2a$ be known. Wave orbital diameter can be estimated from linear wave theory with $d_o=H/sinh(kh)$ where H is wave height, h is water depth, and k is wave number, $2\pi/L$, and L is the surface gravity wavelength.

Near bed velocity measurements in this study allow a much more direct means of acquiring orbital diameter.

Wiberg and Harris [1994] adopted the preliminary criteria proposed by *Clifton and Dingler* [1984] that orbital ripples occur when $d_o/D<2000$, where D is sediment size, and that if $d_o/D=5000$ or larger, anorbital ripples will be found. Here d_o/D is a ratio approximating the boundary layer thickness due to orbital motion to that of sediment grains alone. Between these two end points, the ripples are considered to be suborbital. Wiberg and Harris deemed it more appropriate to define ripple type by a ratio of boundary layer thickness to ripple height, d_o/η_{ano}. Orbital ripples were therefore defined as those where $d_o/\eta_{ano}<20$ and where $d_o/\eta_{ano}>100$ are anorbital ripples. Here $d_o=2a$ and η_{ano} is defined by

$$\left(\eta\big/\lambda\right)_{ano} = \exp\left[-0.095\left(\ln\frac{d_o}{\eta_{ano}}\right)^2 + 0.442\ln\frac{d_o}{\eta} - 2.28\right] \qquad (17)$$

and

$$\lambda_{ano} = 535D. \qquad (18)$$

For orbital ripples, a simple linear relation was found to be

$$\lambda_{orb} = 0.62d_o \qquad (19)$$

$$\left(\eta\big/\lambda\right)_{orb} = 0.17. \qquad (20)$$

For suborbital ripples, η is determined using the orbital relation and

$$\lambda_{sub} = \exp\left\{\left[\frac{\ln\left(d_o\big/\eta_{ano}\right) - \ln 100}{\ln 20 - \ln 100}\right]\left(\ln\lambda_{orb} - \ln\lambda_{ano}\right) + \ln\lambda_{ano}\right\} \qquad (21)$$

which is simply a weighted geometric average of the bounding values λ_{orb} and λ_{ano}.

Time series of forcing parameters for each of the above models calculated using the dominant grain size D=0.30mm and the median grain size D=0.43mm are shown in figures 24a and 24b. Notice that for the larger grain size all of the parameters fall to near or below the lowest forcing threshold, into the orbital regime of Wiberg and Harris or below the critical threshold of Nielsen and Grant and Madsen. Breakoff and Anorbital

thresholds were not approached except at the very highest forcing on yearday 112 and at the end of the deployment on yearday 118.

The models of Nielsen, Grant and Madsen, and Wiberg and Harris show some correlation with observed ripple geometry. Figure 25 shows a time series from yeardays 108-112 of each ripple geometry model and RIPEX observations using complete SAA maps, single SAA profiles, and BCDV height estimates. The median grain size of 0.43mm was used for the model calculations. During the low energy time between yearday 110 and 111.5, agreement between model predictions and observations is very close. During higher energy times before yearday 109 and after yearday 111, model predictions tend to underestimate ripple height and wavelength, although Grant and Madsen less so than the others. The model of *Li et al.* [1997] shows considerably less agreement, reducing the predictions of Grant and Madsen (the closest in terms of physical reasoning because Li merely adjusts the Grant and Madsen coefficients) nearly in half. This is an expected result of the Li et al. model because it was formulated to empirically match observations under combined wave and current forcing on the continental shelf, significantly different from the very dominant wave forcing in the nearshore at the steep beach site. Figure 26 shows the model fits of each geometry measurement to each of the three primary models using the median grain size 0.43mm. The open circles are those measurements taken from single SAA profiles, and demonstrate the poor performance of the models, especially at higher forcing, and this is enhanced by the addition of BCDV estimates in the ripple heights. Note that θ_b does not appear on the Grant and Madsen plots (figure 26b, e, h) because it is well beyond the range of the data. Similarly, the Wiberg and Harris data do not approach the anorbital ripple threshold $d_o/\eta_{ano}=100$.
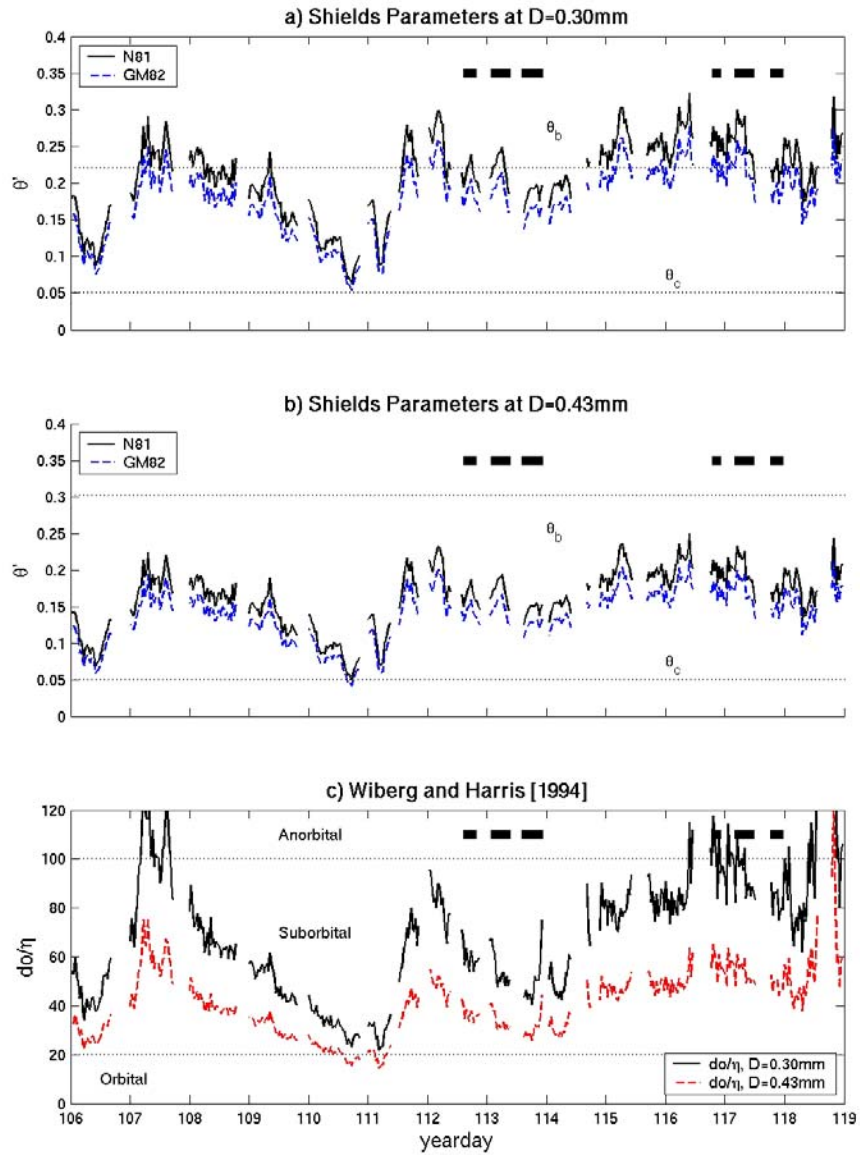
Figure 24. Summary of model forcing parameters over the length of the deployment. (A) θ' of *Nielsen* [1981] (solid) and *Grant and Madsen* [1982] (dashed), with θ_c and θ_b indicated with dotted lines, for D=0.30mm. (B) D=0.43mm. (C) d_o/η_{ano} of *Wiberg and Harris* [1994], with orbital, suborbital, and anorbital thresholds indicated with dotted lines. Times when flat beds are observed are shown as solid black bars.
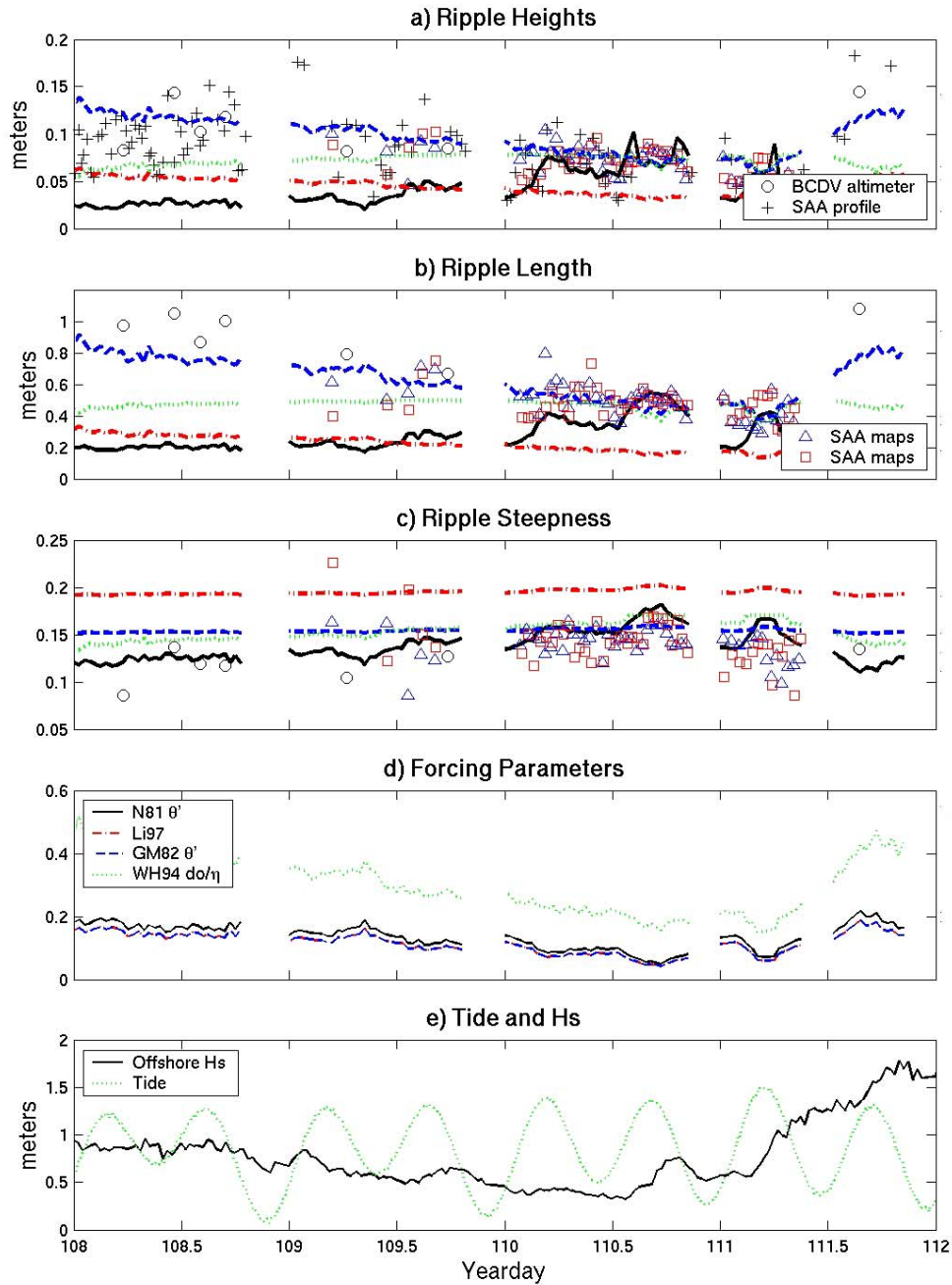
Figure 25. Summary of measured and predicted ripple geometry in the time of greatest data density, yeardays 108-112. Symbols represent measured ripples, and lines represent various predictive models. See figure 20 for symbol legend. (A) Ripple Height. (B) Ripple Wavelength. (C) Ripple Steepness. (D) Forcing parameters defined by predictive models. (E) Offshore Hs and tide height.

53
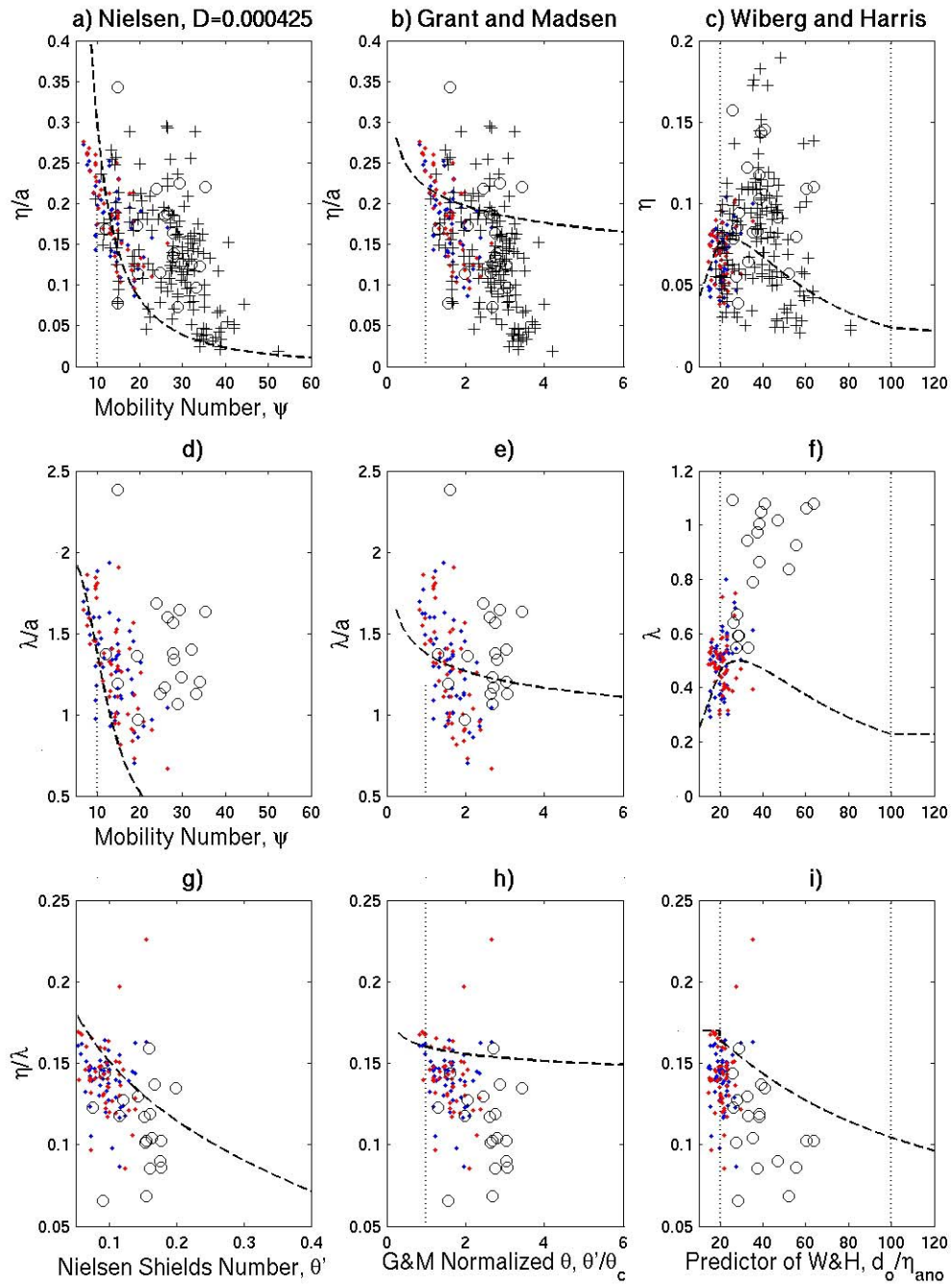
Figure 26. Model fits to ripple height (A-C), ripple wavelength (D-F), and ripple steepness (G-I) as predicted in each model. Closed circles are measurements from fully-resolved SAA maps, open circles from SAA profiles, and '+' from BCDV altimeter ripple height estimates. The median grain size, D=0.43mm, is used.

The models do show some change if the smaller dominant grain size of 0.30mm is used in the calculations. The grain size spectrum in figure 27 shows the range of grain sizes that could be considered in these ripple geometry models. It is expected that smaller grain sizes can be transported more readily, and indeed, using the smaller dominant grain size D=0.30mm increases the range of parameters that the measurements encompass, to include the anorbital or breakoff range, as shown in figure 24a. θ_b/θ_c decreases to just above 4, making the Grant and Madsen ripple prediction curves compress somewhat (figure 28). The predicted ripple geometry curves are otherwise not affected, so the data fit does not change significantly. For data during the lower forcing conditions on yeardays 110 and 111, using 0.30mm slightly improves the overall agreement of the models to the observations, but higher energy ripples are still out of the range of the model predictions. The unsatisfactory manner in which the models handle the great spread of observed ripple characteristics points out a possible deficiency in existing ripple geometry models under more energetic forcing conditions in the surf zone, where the wave forcing is typically more asymmetric as breaking waves and bores pass the observation site.

Similar results were also obtained when using the peak detection method described in section A-3. Using these estimates does not alter the agreement of the models significantly, except that in higher energy conditions the agreement using the peaks improves slightly (not shown). This further proves the applicability of using peak detection estimates at low energy, and may suggest that this method is more applicable and provides an improvement to the existing models in higher wave energy. A similar sensitivity to variation in grain size is also observed when using this method. However, it is likely that other variables including acceleration also exerts an influence on the ripple size and transport, which the existing models also ignore.
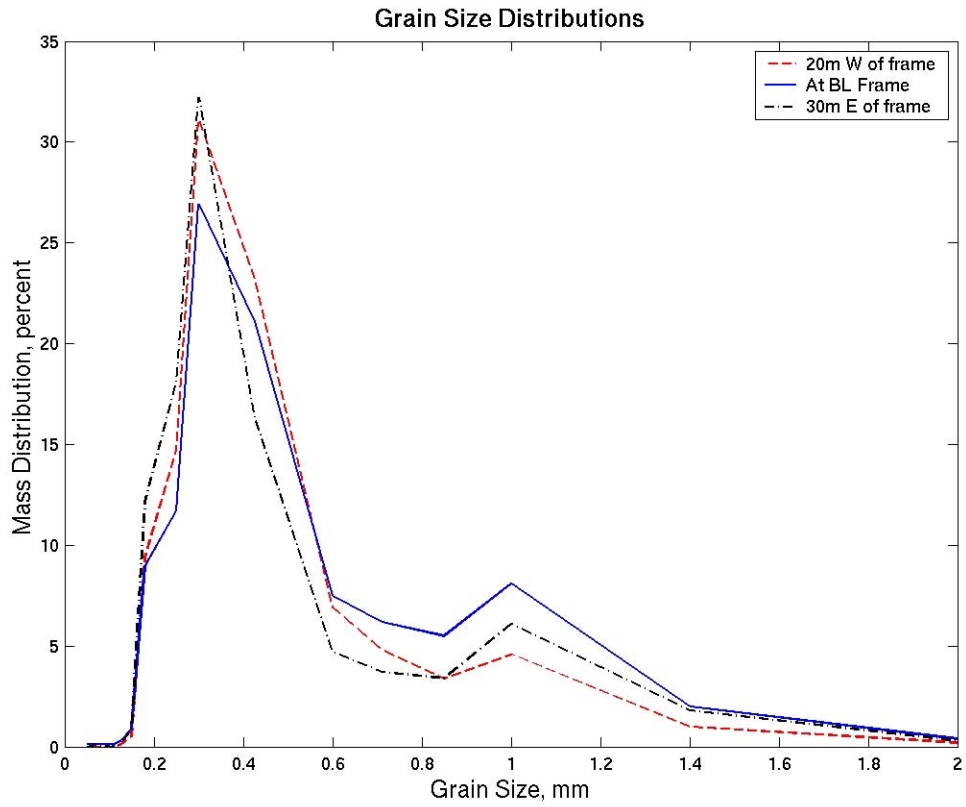
Figure 27. Grain size distribution for each of three samples taken near the boundary layer frame on yearday 110. For each sample, the dominant grain size is 0.30mm and the median (D_{50}) is 0.43mm.
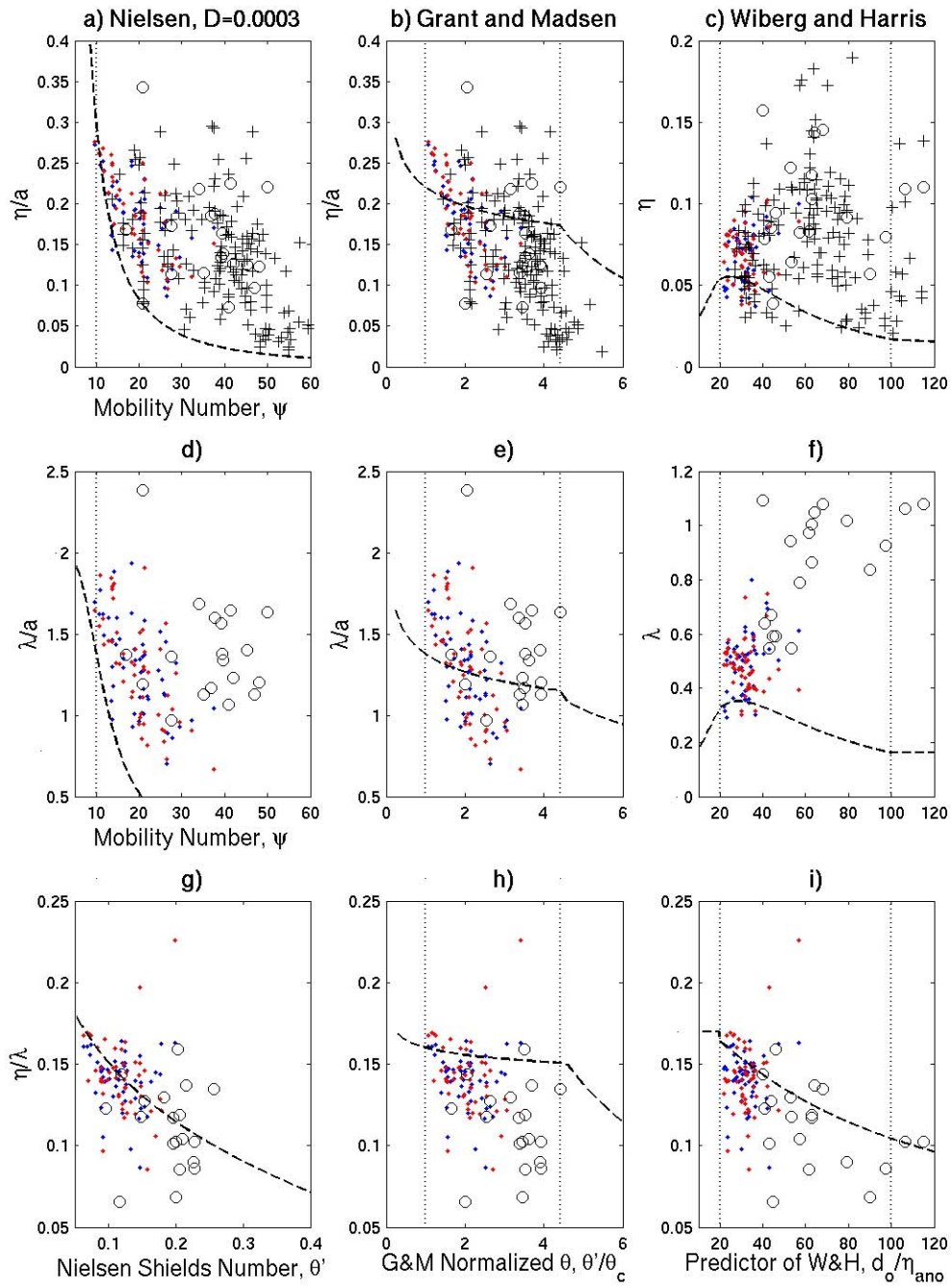
Figure 28. Same as figure 26, using the dominant grain size, D=0.30mm.

Considering figures 25, 26 and 28, the Grant and Madsen [1982] model performs the best, with comparable densities of underestimated and overestimated ripples, although none of the models can be considered to perform well. The peak in each *Wiberg and Harris* [1994] geometry prediction just above the orbital/suborbital threshold ($d_o/\eta=20$), which is the regime in which the forcing exists for most of the measured ripples, causes an artificial maximum to the predicted ripple geometries. All of the models predict a trend of decreasing ripple height and wavelength to orbital semi-excursion *a* with increasing wave energy, but data indicate that higher wave energy can generate larger ripples than predicted by the models, until some threshold is reached where ripples are no longer observed. Curiously, the similarity of model misfit between ripple height and ripple wavelength leads to a much better prediction of ripple steepness. Although steepness again cannot be considered an adequate fit, the trend of steepness decrease with wave energy is, in fact, predicted by all of the models. Interestingly, this is the parameter that is believed to exert the greatest influence in increasing boundary layer roughness.

2.   Sediment Transport Predictions

Many attempts have been made at estimating the total sediment transport under unidirectional flows, but only the three models presented here, are considered reasonable means of estimating sediment transport under combined wave and current forcing [*Li et al.,* 1997].

Total load predicted by *Engelund and Hansen* [1967]:

$$q_s = \frac{0.05 D u_{100}^2 \rho^2 u_*^3}{D(\Delta\rho g)^2} \tag{22}$$

where q_s is the volume rate of sediment transport, u_* is the skin-friction shear velocity, and $\Delta\rho=\rho_s-\rho$ is the differential sediment density.

Total load equation of *Bagnold* [1963]:

$$q_s = \frac{K\rho u_*^2 u_{100}}{\Delta\rho g} \tag{23a}$$

$$K = 0.005 \exp(0.7S) \tag{23b}$$

where K is the proportionality coefficient according to *Sternberg* [1972] and $S = \tau_{ws}/\tau_c - 1$ is the normalized excess shear stress.

Suspended load is considered minor in the Einstein-Brown (*Brown* [1950]) bed load equation:

$$q_s = 40 D w_s \left(\frac{\rho}{\Delta \rho g D} \right)^3 u_*^5 |u_*| \qquad (24)$$

where w_s is the sediment grain settling velocity, estimated by *Gibbs et al.* [1971] as 3.3 cm/s for D=0.29mm and 5.0 cm/s for D=.42 mm.

Volume sediment transport magnitude as predicted by each model and by observed ripple geometry and motion is shown in figure 21. Because ripple migration could only be robustly estimated during days 110-111.5, figure 21b is limited to this time interval. Transport analysis was performed using the dominant grain size of 0.30mm, which was considered appropriate because the dominant grain size is the most available for transport, and because smaller grain sizes are more readily transported. Direction was obtained by setting free-flow and shear velocities to negative when the raw time series mean was negative (onshore). The *Engelund and Hansen* [1967] model, as found by Li et al. [1997], shows good agreement in form, but yields predictions a full order of magnitude less than those of *Bagnold* [1963] and *Brown* [1950] and thus is excluded from this analysis. The *Bagnold* [1963] and Einstein-Brown models predict the transport mimima at high tide well (figure 21b), and the timing of the increase at the low tide in the middle of yearday 110 is reasonably well handled, although the magnitude tends to be underestimated. During other low tides, however, although measurements could not be taken, the rate increase in transport is greatly enhanced by the models (figure 21a). Modeled transport peaks were highest during the storm passage on yearday 112 and during the other high infragravity energy times on yeardays 107-109 and yeardays 115-117 (figure 21).

Similar analysis was performed using a larger grain size D=0.43mm (not shown), and as expected, the models predicted that the larger grains would be more difficult to transport, and lower transports were predicted. Vector peak estimates were also used in a

59

separate analysis, also not shown, and the results with each of the two grain sizes were very similar to those using the standard spectral RMS estimates, again as expected.

IV. DISCUSSION

A.   GENERAL OBSERVATIONS

The storm starting on yearday 111 that results in the sharp increase in offshore significant wave height caused near-bottom orbital velocities to increase above the threshold for shearing off ripple crests (figure 24), and the ripples were eliminated from the bed. Wave energy continued to produce sheet flow (figure 20) until forcing dipped substantially into the suborbital/equilibrium range on yearday 114. Infragravity energy, here defined as that portion of the velocity field with periods greater than 20 seconds, following the storm also remained high throughout the remainder of the experiment, except for a brief exception on yearday 114. Only on yearday 117 did the forcing begin to dip below the sheet flow threshold, allowing broad ripples that stretched beyond the sampling domain of the SAA. Prior to yearday 109, during another sustained high infragravity period, SAA coverage was very poor and regular bedforms could not be resolved from the maps.

Nearshore theory on planar beaches predicts that to maintain water mass balance, the onshore mass transport of incident swell is returned seaward as a mean offshore bottom current, commonly referred to as undertow. On beaches with a rip current present, as is predominantly the case in southern Monterey Bay, the wave mass transport over the shoal is instead directed alongshore and returned offshore as the rip current itself. This allows onshore mean currents to extend all the way to the bottom boundary layer without disruption. The onshore mean bottom currents shown in figure 21 lead to onshore migration of ripples during this time.

The magnitude of this shoreward current was also strongly modulated by the tide. Mass transport due to waves, as with all parameters associated with orbital wave motion, is a maximum near the surface, and decays with depth. For comparable wave forcing during a tidal cycle, as the tide goes out the onshore mass transport is confined to a smaller water column height, increasing the shoreward velocity. This tidal variation is seen in figure 21.
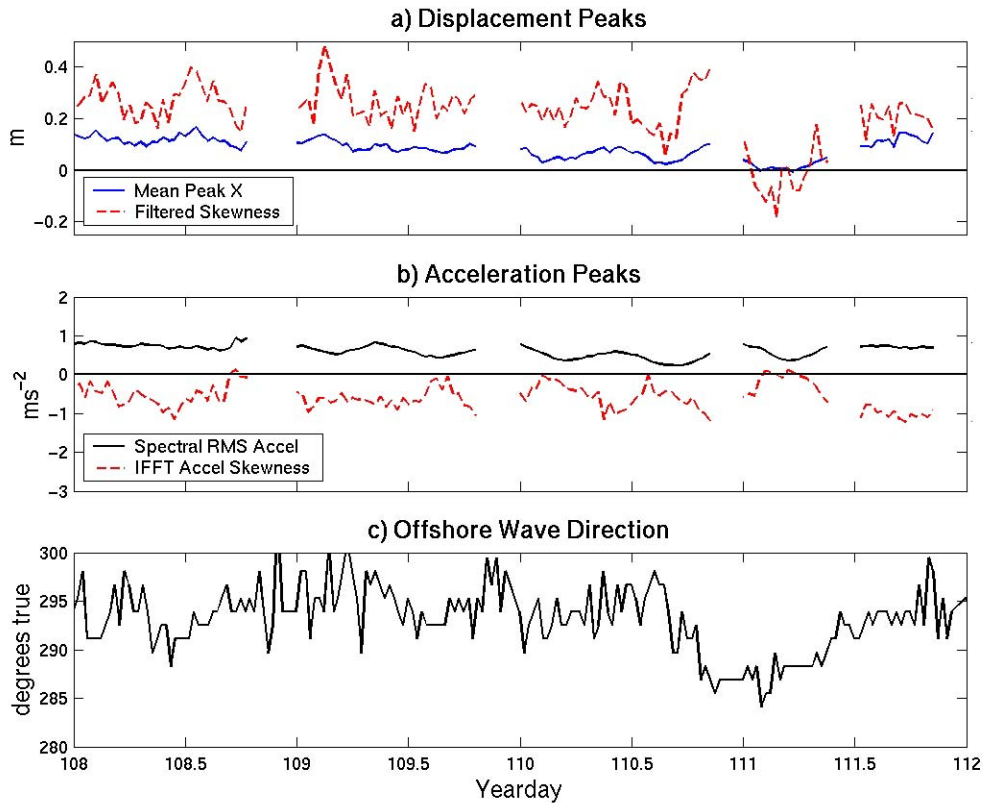
Figure 29. Time series of wave properties near observed onshore ripple migration on yearday 111. (A) Mean of displacement peak distributions (solid) and skewness of the filtered displacement time series (dashed). (B) Spectrally estimated RMS acceleration (solid) and skewness of the filtered acceleration time series (dashed). (C) Peak wave direction measured by the offshore (17m water depth) buoy.

The offshore ripple migration and transport on yearday 111 posed an interesting exception to the expected onshore migration from a mean onshore current. Coincident with this transport reversal are an anomalous reversal in the skewness of T<20sec bottom cross-shore orbital displacement, a mean of cross-shore displacement peak distributions near zero, and a skewness of T<20sec cross-shore acceleration near zero (see figure 29). These anomalies indicate that although mean orbital displacement peaks were not as asymmetric during this time and acceleration was not as skewed toward onshore, the orbital displacement reversed its skewness and ripples migrated offshore. Examination of the offshore incident wave direction reveals a change during this time from around 305T to 290T. This created a situation where the waves incident to the shoal broke and

62

dissipated, but the waves incident to the rip channel were able to be reflected at the shore, and propagated offshore more strongly than the dissipated shoal waves propagated onshore. This causes ripples to migrate offshore and change direction along the crests, as the corresponding SAA grid maps (figure 11k,l) show. The anomalous displacement statistics shown in figure 29 may be a means by which reflected waves and/or offshore ripple migration can be identified with the forcing.

Volume sediment transport by ripples in figure 21 is shown to fit reasonably to the transport models of *Bagnold* [1963] and Einstein and Brown [*Brown,* 1950] when a smaller grain size is considered. The period from yeardays 110-111.5 is one where the bed load (Einstien-Brown) or total load [*Bagnold,* 1963] appears to be predicted almost entirely by observation of ripple migration, suggesting that little deep suspended sediment transport outside of the ripple volume is occurring. This match between ripple migration transport and bed load transport models supports the assertion that ripple migration is symptomatic of bed load, sediment suspension and settling confined within wave orbits. The high transport rates predicted in figure 21 by Einstein and Brown and Bagnold as the wave forcing increases outside of yeardays 110-111.5 and the presence of flat-bed conditions during the higher forcing conditions demonstrate that sediment transport within ripples is restricted to low/moderate forcing conditions. Further analysis of BCDV sediment concentration profile time series is in progress and is expected to further validate this hypothesis.

B.   MEASUREMENT UNCERTAINTY

The SAA and BCDV, along with the boundary layer tower array, provided a unique data set of water column, boundary layer and morphology within the surf zone. Field measurements by nature are fraught with uncertainty and problems, particularly when using newly devised instruments such as these. However, analysis of instrument limitations is instructive in determining ways to improve the utility of the instruments in future experiments.

The three sediment samples presented in figure 27 were collected during yearday 110, under the lowest forcing conditions. Collecting sediment during the most benign forcing allows the sample to be most representative of the total sediment present because

winnowing of fine sediments in the upper bed by strong currents or waves occurs easily. Sediment distribution on other days during the deployment is unknown. The sensitivity of ripple geometry and transport models to grain size suggests that as the forcing increases, smaller grain size fractions may be preferentially transported, leaving the larger grains to maintain the structural integrity of the ripples, which may grow larger at larger grain sizes. Regular bed sediment collection near the boundary layer array, despite the risk of winnowing under various forcing conditions, may verify this hypothesis.

Several assumptions were made about the shape and movement of orbital ripples for this paper. To correct the observed ripples for ripple migration during the sampling time of the SAA, it was necessary to assume ripple migration was uniform across the altimeter domain and constant through the SAA sampling time. The continuity of migration speeds over the second tidal period of yearday 110 indicates that migration speeds estimated by centerline displacements are valid (figure 19a) and this is corroborated by migration rate estimates from the BCDV. The deviation of the sample-time corrected ripple crest orientation from shore-parallel in figure 19b is small, and supports the assumption used in SAA profile measurements that shore-parallel ripple measurements are accurate.

The location of the forcing measurements and bottom measurements were not exactly co-located. The 3-meter separation is well within the limits, however, of assuming homogeneity in the wave forcing, and forcing and morphology statistics over only 60 minutes are considered. The shoals between rip channels were continuous over 100 meters or more, and daily on-site inspections of the array and the surrounding bathymetry confirmed that the form of the shoal on which it was situated did not vary within 30 meters of the boundary layer array location.

The drift in the wave wire means from tide height in Figure 17b is a concern, but examination reveals that the drift is in absolute value, not in span. While this makes tide height comparisons and water depths suspect, very high resolution significant wave heights estimated by the wave wire retain their robustness. This small drift term is typical of capacitance wave wires over O(hours).

Although the maps obtained from the SAA were spectacular, forcing conditions under which detailed SAA maps were obtained were limited by the location of the instruments 1m above the bed. The highest quality and concentration of maps were obtained during the lowest forcing conditions of the entire deployment. Full maps obtained later in the deployment did allow observations of a flat bed. Bubble injection due to wave breaking in higher energy conditions degraded the quality of the altimeter maps, although this is a fundamental limitation of all non-invasive acoustics and optical bed sampling methods. High bubble densities (>0.01%) are very persistent in the surf zone and create strong scattering, or opaque, conditions for 10KHz-50MHz acoustic frequencies used in acoustic altimeters. The presence of suspended fine sediments presents an even more severe limitation for optical morphology measurements [*Dixon,* 2000] Fortunately, both SAA profiles from incomplete maps and BCDV measurements were obtainable during intermediate forcing, although these measurements are not as robust as detailed altimetry maps.

An important limitation of the data collected for this experiment is that it investigates morphology evolution at a single location, so no inferences can be made as to the accretion or erosion of the shoreline. Transport by ripples was estimated from ripples moving past this one point, and future studies will focus on examining the suspended and bed load flux profile time series as obtained by the BCDV. However, accumulation or depletion is the result of sediment flux divergence. To be able to estimate flux lateral divergence, similar measurements could be obtained from several locations arranged to capture flux gradients in several axes. However, then only the accretion or erosion within that specific series of arrays can be estimated and the sensitivity to typically high errors in sediment transport would likely produce very noisy net flux changes. Instead, net accretion and erosion rates are estimated by periodic bathymetry surveys made during the experiment.

C. MODEL UNCERTAINTY

The models presented herein represent current thinking in how wave forcing dictates ripple geometry. *Nielsen* [1981] used laboratory and field studies of others to

predict η/λ as a function of the non-dimensional shear stress (Shields number), and both η and λ, scaled by orbital amplitude, a, in terms of the mobility number ψ, a measure of the intensity of the free flow. Referring to equations 9-11, it is interesting to note that although the shear stress is significant in determining steepness of the ripples, it bears no direct impact on the individual terms. Nielsen created separate expressions for laboratory and field data in order to fit the data continuously.

Grant and Madsen [1982] developed their model to predict ripple steepness and height η/a as a function of the normalized shear stress, θ'/θ_c (table 2). Grant and Madsen's expressions were defined by an "equilibrium range", bounded by the breakoff point θ_b. This breakoff Shields number is defined by a non-dimensional sediment parameter S* that also appeared in the geometry expressions to help reduce the ripples as wave forcing moved beyond the breakoff point.

Wiberg and Harris [1994] defined ripple wavelength and steepness as a function of orbital diameter. They used d_o/η to devise a classification scheme, of orbital, suborbital, and anorbital ripples. The parameter d_o/η was used as a proxy to the ratio of the bottom boundary layer thickness to the ripple height, which they contend is the primary distinction between orbital and anorbital ripples. Based on this classification, ripple wavelength and steepness were defined as a function of orbital diameter for orbital ripples, grain size for anorbital ripples, or a weighted geometric average for suborbital ripples.

Shortfalls of each of these models are well documented. *Nielsen* [1981] developed his model primarily from laboratory measurements, and only modified his equations to empirically fit field observations. Because of his emphasis on lab data, Nielsen tends to underestimate ripple height and wavelength, as seen in the analysis for this paper and *Li et al.* [1998]. Wiberg and Harris noted that Grant and Madsen significantly over-predicts ripple wavelength at high forcing, in conditions that would be considered suborbital by Wiberg and Harris. They also noticed that their own model overpredicted ripple steepness near the transition of orbital to suborbital ripples, another result seen in these observations.

General limitations of ripple geometry and sediment transport models are the result of an effort to simplify parameters required for the prediction. Few observations are made in as energetic conditions as is experienced in the surf zone, and none were actually created from experiments performed in the surf zone. The nonlinearity of the waves and the turbulent dissipation that waves undergo in the surf zone make for drastically differing bottom boundary layer processes and conditions than is present in deeper water. Each model then attempts to summarize ripple geometry into one or two forcing parameters based on a scalar RMS value of narrow-banded waves, but it is suggested here that the forcing parameters that determine ripple geometry are more complex. Perhaps most importantly, the forcing parameters that are used are RMS estimates of swell velocity or displacement in the cross-shore direction only. While this method has proven valid in many cases, it is an over-simplification of what occurs on a real beach under shoaling and breaking waves.

D. PHYSICAL CONCEPTUAL MODEL

The ripple geometry model of *Wiberg and Harris* [1994] contained the most applicable physical reasoning with their ripple type predictor. When the boundary layer thickness is significantly less than the ripple height, the boundary layer follows the contours of the ripples, and sediment motion is primarily in the form of saltation. As boundary layer thickness increases, it continues to follow the bottom features, but it will begin to thicken in the troughs, as the boundary layer is compressed on the facing side of the crest, and vortices are generated over the troughs. This begins the process of sediment suspension above the layer that will result in ripple migration and alteration. With increased forcing, as the boundary layer thickness exceeds the ripple height, the flow following the ripple shape cannot be contained by the ripples, which will cease to have an effect on the shape of the boundary layer. Ripples crests will rapidly begin to shear off and the troughs will fill in. During this transition to sheet flow, transport rates soar throughout the boundary layer as the crests get sheared and the ripples are not tall enough to "block" the suspended sediment. The line between bed load and suspended sediment becomes obscured.

Orbital diameter is the primary variable one must examine in determining ripple wavelength. In the absence of large mean currents, once a wave orbital starts to pick up or roll a grain or grains, the orbital diameter will physically limit how far the wave can carry that sediment. If sediment gets injected into the column as suspended load outside of the wave boundary layer, the bedforms are further modified.

Ripple height will increase as sediment is deposited near the crest faster than it is eroded, or dug from the trough faster than it is deposited. Otherwise, ripple height will remain unchanged. Sediment will be deposited near the crest by wave orbitals, so the more constant the orbitals remain, the faster sediment will accrete at the preferred sites. The trajectory of the sediment particles leads to an examination of displacement peak distributions, described below.

Orbital asymmetry creates a means for sediment transport. Onshore movement not quite matched by offshore movement creates a net onshore ripple migration. Because transport occurs dominantly within the boundary layer, sediment motion serves to modify or move the ripples until either wave energy surpasses the threshold for shearing crests and filling troughs or forcing falls below the threshold for sediment movement. Imposing mean currents also creates orbital asymmetry necessary for ripple migration, but otherwise will not affect transport unless sediment is injected well above the bottom boundary layer. In deeper water, wave boundary layers may be thin, allowing for some sediment to be injected above it, and then carried by mean currents. In the high energy nearshore, wave boundary layers are thicker. Mean currents are not strong at the RIPEX/Steep Beach site, with weak longshore currents, owing to mean normal wave incidence. Over a shoal between rip currents, the mean current is primarily directed onshore. This causes the particle orbits to have net onshore displacements, so in addition to the nonlinearity of the shoaling and breaking waves, both processes cause a net shoreward transport.

E.   PEAK DETECTION METHOD

A peak detection PDF allows complexities of mean currents and wave asymmetries in the forcing to be parameterized in a vector sense. Typical RMS velocity and orbital diameter measurements are simple spectral estimates of cross-shore velocity.

The assumption that the dominant oscillatory motion is in the cross-shore direction is good within the nearshore, but even this ignores finite directional spreading of the wave orbits. Detecting vector displacement peaks from orbital displacement time series allows a distribution of wave orbital motion to be described. Distribution of the peaks reveals a range of wave properties including orbital asymmetry, mean currents, and directional spreading, as demonstrated in figure 30. The spatial distribution shows maxima and minima that represent the dominant orbital displacement of the wave field. Estimating major and minor axes through PDF's of these maxima also provides an estimate of the incident wave direction. A more intense maxima on one side of the ellipse indicates an asymmetry in the wave field. Finally, an offset of the mean from zero indicates the influence of infragravity energy or a mean current.

Ripple shape and movement is described by current models assuming even, cross-shore wave orbitals (figure 30a). This creates ripples that are straight, long-crested, symmetric and shore parallel, but short-crested, bifurcated, oblique, uneven and asymmetric ripples have been frequently observed by others in the past [*Amos et al.*, 1988, *Hay and Wilson,* 1994, *Traykovski et al.,* 1999] as well as in this study. It is proposed that the observed ripple forms are predictable from analysis of two-dimensional vector displacement peak PDF's.

Ripples are rarely straight and even. If wave orbitals were uni-directional and narrow-banded, this is what one would observe, but this is rarely the case. Directional spreading of the incident wave energy is always present, as shown in figure 30b, and this creates minor irregularities along the ripple in height or orientation. The width of the displacement peak PDF is indicative of this directional spreading (see figure 30b, 31c). The ripple spacing, however, is dominated by the orbital diameter, and maxima in peak distribution gives a measure of the orbital diameter by vector parameterization rather than a scalar RMS value. Figure 31 shows a displacement peak relative density distribution from T<60min high passed (31b) and T<20sec (31c) orbital displacement time series. The T<20sec peak distribution does not appear as a uni-axial oscillation, but as a directionally spread ellipse, with two distinct peaks indicating the dominant orbital diameter.
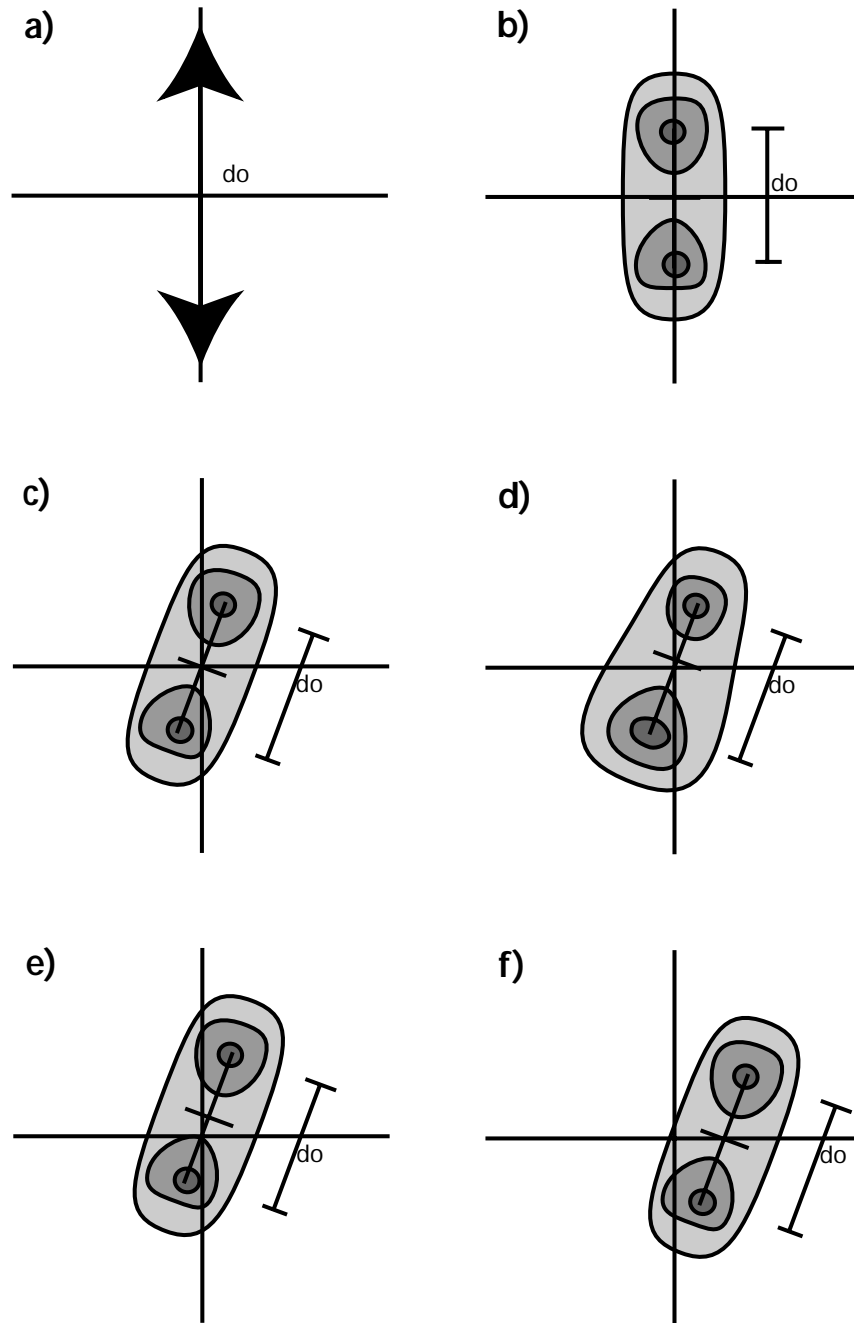
Figure 30. Hierarchy of orbital displacement distributions with increasing complexity. These represent conceptual models of forcing and bed responses not considered in existing predictive models. (A) Narrow-banded, cross-shore RMS orbitals used in existing models. (B) Directional spreading in the wave orbits gives the ripples some irregularity. (C) Rotation of major and minor axes create ripples that are at an angle to the shore. (D) Asymmetry in the orbital displacement distributions is a mechanism which allows ripple migration. (E) Along-axis very low frequency motions or currents are another means of creating orbital asymmetry. (F) Cross-axis VLF motions or currents cause ripples to become short-crested and eventually shear off.

Ripples are often oriented shore-parallel, but sometimes are not. Waves which are incident at some angle to shore-normal, as in the example figure 30c, are suggested to be the reason for a rotated ripple field. Displacement peak PDF's capture this angle as well. The PDF in figure 31c is nearly shore-normal, and this is confirmed by the shore-parallel ripples in the corresponding grid maps in figure 11f and 11g. By comparison, figure 32c shows a slightly more rotated peak distribution, agreeing with the reorientation of the ripples which is occurring on the left side of the corresponding grid map, figure 11j. Figure 33c shows an even greater angle to the shore, as well as a wider orbital diameter that may be the cause of the flat bed conditions seen in the SAA data.

Ripples are observed to migrate in most cases, and are rarely symmetric in profile. Ripple migration occurs when orbital motion in one direction is more forceful than in the other. Asymmetry in the orbital motion is reflected in orbital displacement, velocity, and acceleration, as shown in figure 30d. A more concentrated peak distribution on one side of the elliptical mean is an indication of this asymmetry, and, we propose, an indicator of ripple migration direction. Displacement asymmetry in the offshore direction results in more vigorous orbital velocity reversals as waves propagate onshore, and so velocity and acceleration time series will likely be asymmetric onshore, resulting in an onshore ripple migration. The offset of the mean in the offshore (positive) direction in figure 31c would therefore indicate an onshore ripple migration, and this is indeed what is observed at this time in figure 19a. The mean in figure 32c is zero, and this is observed as a stalling or even reversal of the ripple migration in figure 19a, supporting this as a measure of migration tendency.
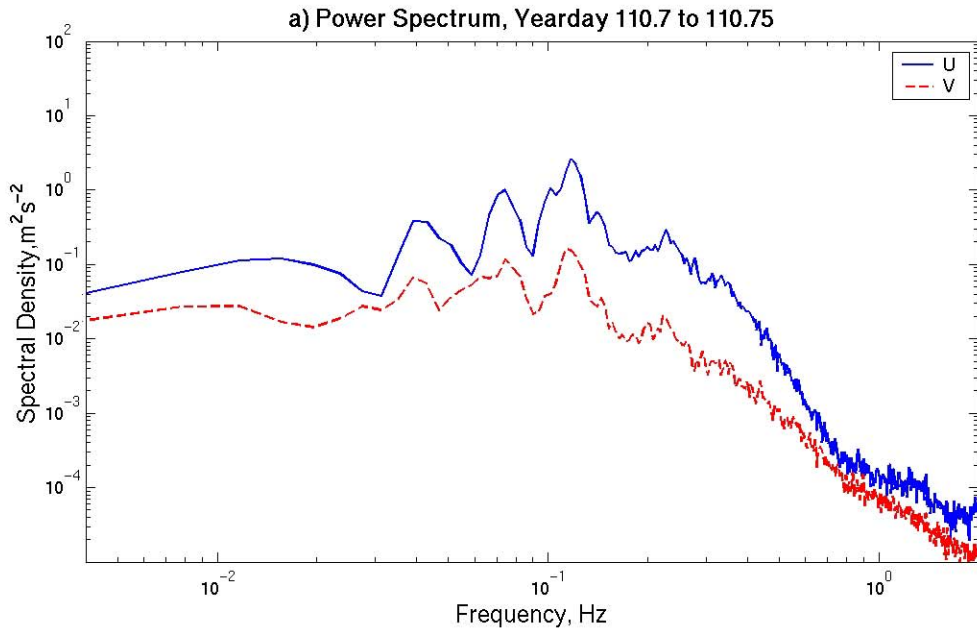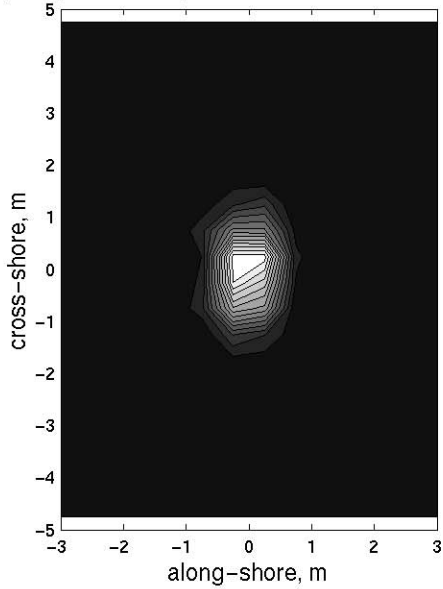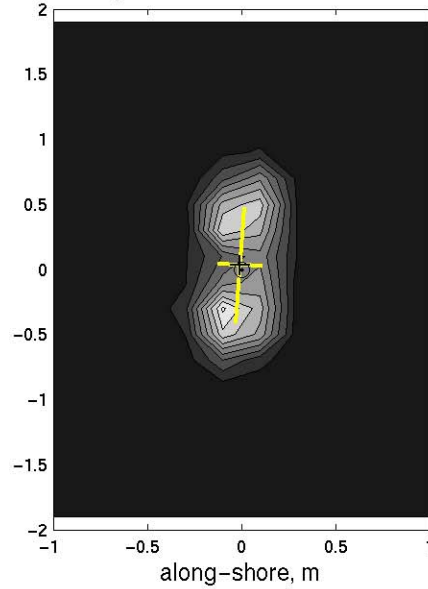
Figure 31. Wave forcing for low energy, active vortex ripples on yearday 110.70-110.75. (A) Cross-shore and along-shore power density spectrum. (B) Full bandwidth peak displacement distribution. (C) Peak orbital displacement distributions for T<20s waveband energy. Bullseye marks the origin and cross-hairs mark the mean location.
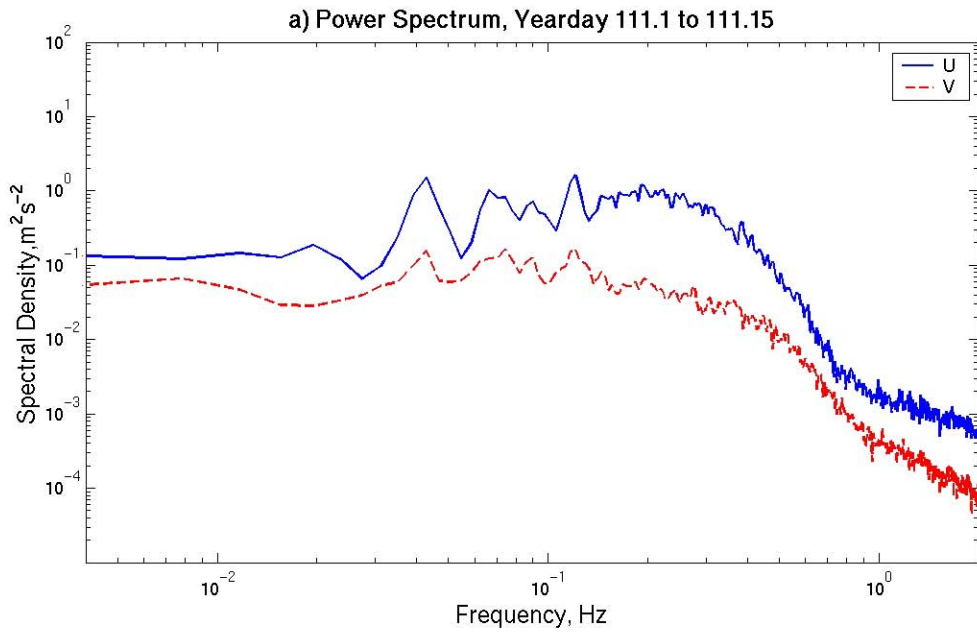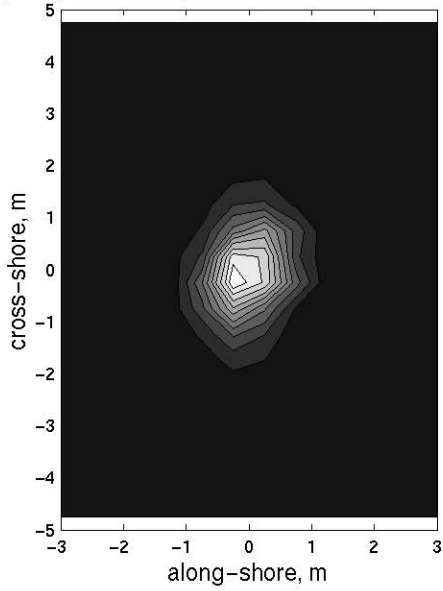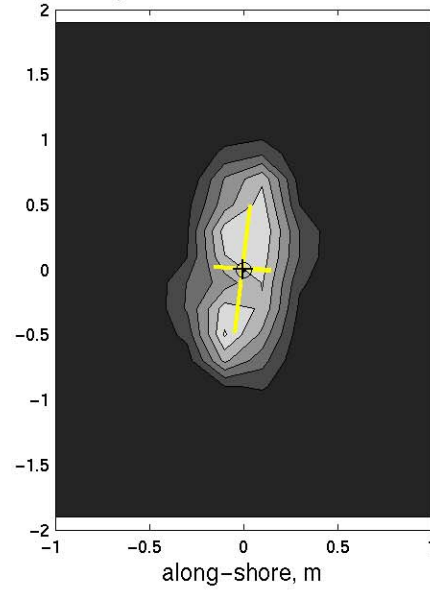
Figure 32. Same as Figure 31, except for the offshore ripple migration on yearday 111.10-111.15.

a) Power Spectrum, Yearday 113.2 to 113.25
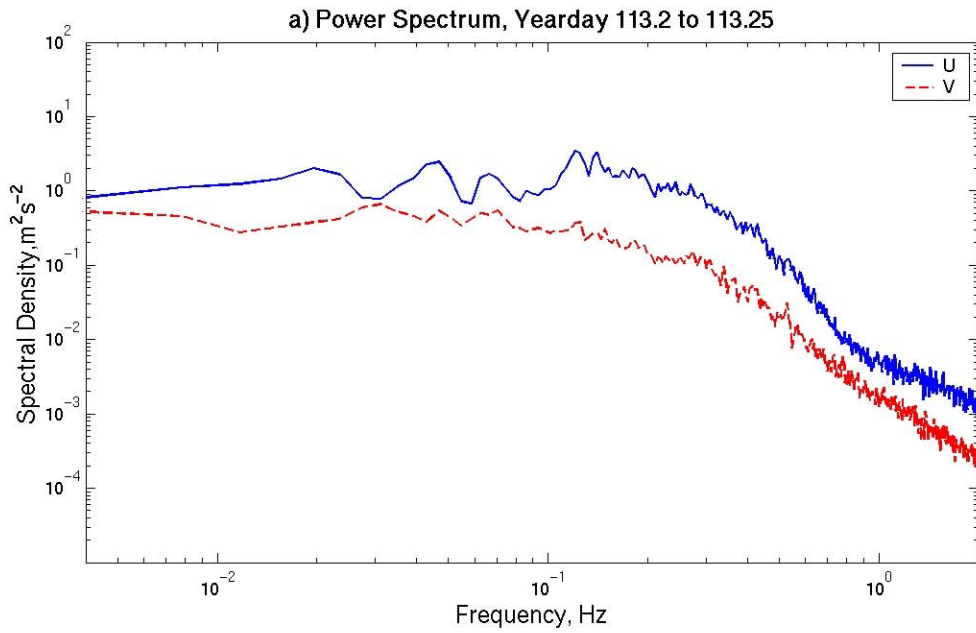
b) Displacement peaks, T<60min, 1% contours
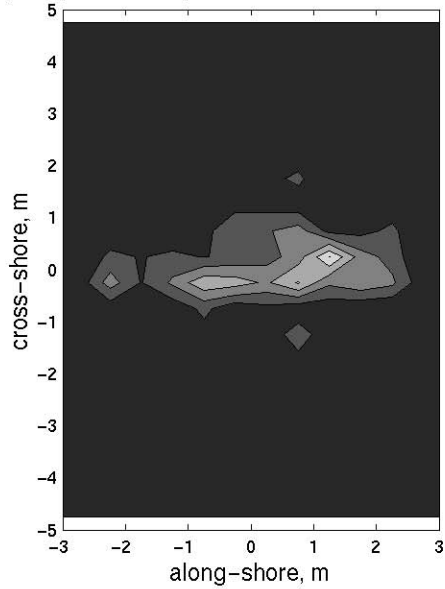
c) T<20s, rotation=13.0321
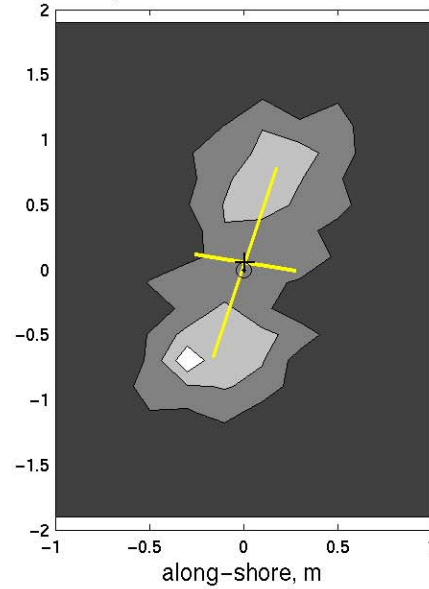
Figure 33. Same as Figure 31, except for observed sheet flow conditions on yearday 113.20-113.25. Note significant along-shore oscillation in full bandwidth peak distribution.

a) Power Spectrum, Yearday 118.35 to 118.4
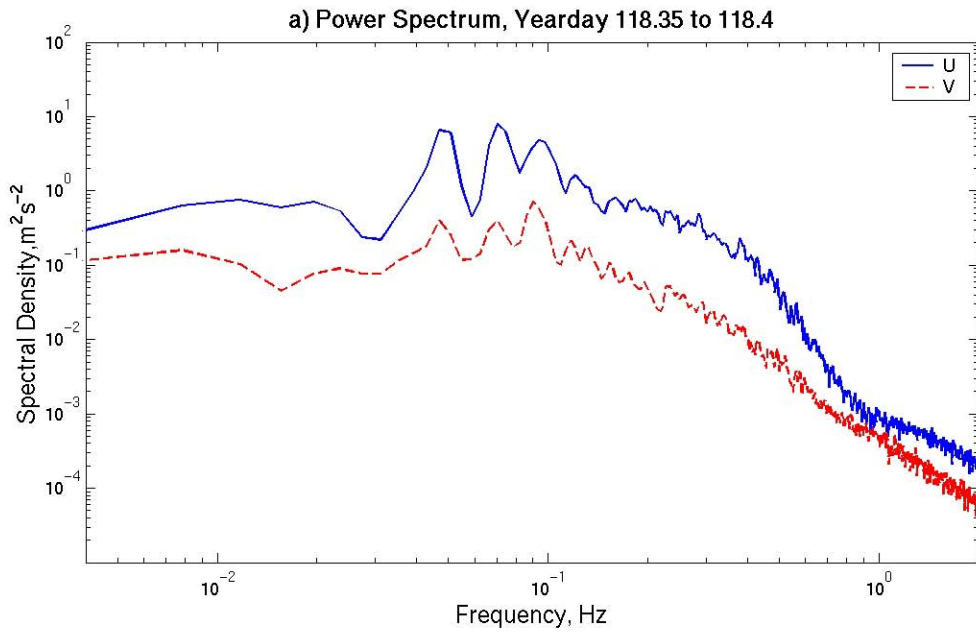
b) Displacement peaks, T<60min, 1% contours
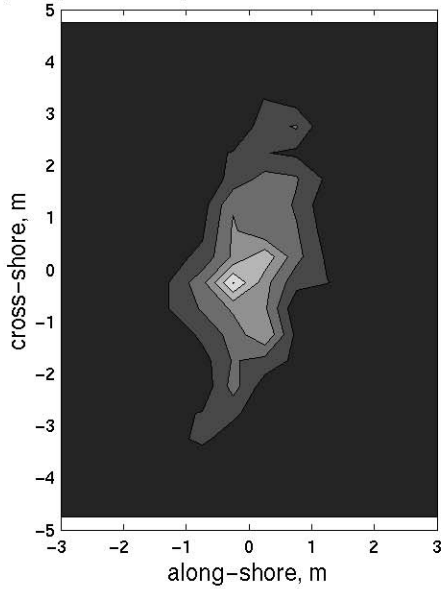
c) T<20s, rotation=10.3326
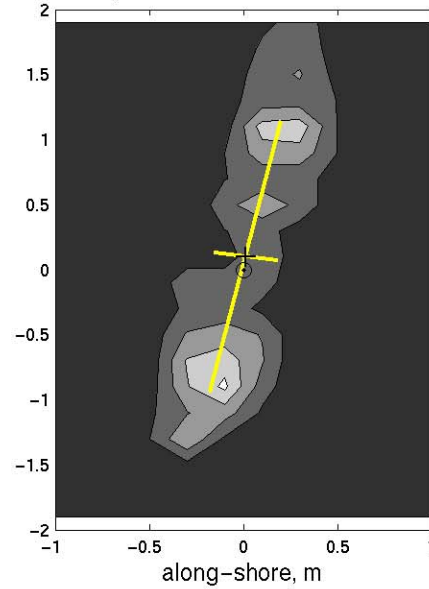
Figure 34. Same as Figure 31, except for ripples are beginning to reappear on yearday 118.35-118.4. Note large orbital diameter and axis rotation, but lack of significant along-shore oscillations in full bandwidth peak distribution.

Power spectral density plots show strong peaks below 0.05 Hz (figures 31a, 32a, 34a) that may be the result of wave reflection or bound long waves, and increased energy below 0.05 Hz (figure 33a) that indicate a substantial very low frequency contribution to the wave field. Superposition of a mean current or strong low frequency nearshore motion onto wave orbitals creates a shift in the direction of the mean motion (figures 30e,f). If the shift is in the direction of the semi-major axis of the ellipse, an asymmetry is simply imposed on the wave forcing and ripple migration will result. If the shift is strong enough that both of the distribution maxima are in the same direction, then ripples will not be sustained and will shear off. If the shift is transverse to the semi-major axis, sediment paths cease to be straight and regular. Alongshore transport will occur, and ripples will begin to shorten their crests and bifurcate. *Amos et al.* [1988] considered this indicative of an unstable ripple field, and if sustained or increased, will eliminate the ripples. Figure 33c shows a peak mean that is slightly offshore, which is not indicative of a mean flow in the direction of swell oscillations. Examination of the full bandwidth peak distribution in 33b, however, reveals a strong along-shore oscillation. This is indicative of enhanced edge wave motion that, in conjunction with the large orbital diameter, is helping to suppress the formation of ripples on the flat bed. By contrast, figure 34 shows a condition where the orbital diameter is large, but no significant along-shore motion is present in the full bandwidth peak distribution. At this time in the bed observations, large ripples are beginning to re-form from previously flat beds as the forcing declines over yeardays 117 and 118. This may indicate that a combination of low frequency along-shore oscillation and large swell orbital diameters are necessary for ripples to be eroded completely.

Incorporating a displacement peak analysis into ripple geometry prediction models is thus shown to possibly improve the accuracy and the overall utility of the model. In addition to being able to determine orbital diameter, two-dimensional displacement peak distributions could allow a characterization of the crest orientation, migration direction and speed, and the propensity for crest shortening or ripple shearing. Ongoing analyses of displacement peak PDF's are being used to develop a more robust ripple geometry transport model for the surf zone.

V. CONCLUSION

Comprehensive analysis of detailed bottom velocity, wave height, and bedform measurements has shown that the ripple geometry predictors of *Nielsen* [1981], *Grant and Madsen* [1982] and *Wiberg and Harris* [1994] can be used to qualitatively compare low-to-moderate forcing conditions with high quality SAA data and BCDV altimeter measurements. Observations of larger ripples under higher forcing conditions, near the breakoff or anorbital range, are not well predicted by the models, which predict a decrease in ripple height and wavelength.

The total load equation of Einstein and Brown qualitatively captures the transport by ripples. This suggests that mass transport within ripple migration reflects the bulk of the total sediment transport under forcing conditions lower than the threshold for sheet transport.

Existing ripple geometry and transport models developed for deep water conditions over-simplify the orbital displacements and velocities as uni-axial, spectral RMS estimates. Within the surf zone, field measurements of displacement has revealed considerably greater complexity in actual wave forcing. Directional spreading, rotation, wave asymmetry, and superimposed infragravity energy or mean currents are presented as a hierarchy of forcing complexity, and are proposed as elements of a physical model to predict ripple geometry and migration in the surf zone.

Ongoing efforts to characterize the bed and bottom boundary layer will examine the suspended and bed load transport, velocity profiles, and further examine the potential of displacement peak ripple models. Future studies are planned that will increase the sampling rate of the Scanning XY Acoustic Altimeter, and add similar high resolution optical measurement techniques to examine the timing of sediment suspension within the wave cycle.

THIS PAGE INTENTIONALLY LEFT BLANK

LIST OF REFERENCES

Bagnold, R.A., Motion of Waves in Shallow Water: Interaction Between Waves and Sand Bottoms, *Proc. R. Soc. London Ser. A, 187*, 1-15, 1946.

Bagnold, R.A., Mechanics of Marine Sedimentation, in *The Sea, Vol. 3*, Wiley-Interscience, New York, 507-527, 1963.

Boyd, R., D.L. Forbes, and D.E. Heffler, Time-Sequence Observations of Wave-Formed Sand Ripples on an Ocean Shoreface, *Sedimentology, 35,* 449-464, 1988.

Brebner, A., Sand Bed-Form Lengths under Oscillatory Flow, in *Abstracts in Depth,*, 17th International Conference on Coastal Engineering, Sydney, 1980.

Brown, C.B., Sediment Transportation, in *Engineering Hydraulics*, Wiley, New York, 796 pp, 1950.

Carstens, M.R., R.M. Neilson, and H.D. Altinbilek, Bed Forms Generated in the Laboratory under an Oscillatory Flow: Analytical and Experimental Study, *Tech. Memo 28*, 39 pp, U. S. Army Corps of Eng., Coastal Eng. Res. Cent., Washington, D.C., 1969.

Clifton, H.E., and J.R. Dingler, Wave-Formed Structures and Paleoenvironmental Reconstruction, *Mar. Geol., 60*, 165-198, 1984.

Dinger, J.R., Wave-Formed Ripples in Nearshore Sands, Ph.D. thesis, 136 pp., University of Calif., San Diego, 1974.

Dixon, D.B., Evolution of Bedforms on the Inner Shelf, M.S. thesis, 60 pp., Naval Postgraduate School, Monterey, 2000.

Engelund, F., and E. Hansen, *A Monograph on Sediment Transport in Alluvial Streams*, Teknisk Vorlag, Copenhagen, 62pp, 1967.

Gibbs, R.J., M.D. Mathews, and D.A. Link, The Relationship Between Sphere Size and Settling Velocity, *J. Sedimen. Petrol., 41*, 7-18, 1971.

Grant, W.D. and O.S. Madsen, Movable Bed Roughness in Unsteady Oscillatory Flow, *J. Geophys. Res., 87,* 469-481, 1982.

Grant, W.D. and O.S. Madsen, The Continental Shelf Bottom Boundary Layer, *Annual Review of Fluid Mechanics, 18,* 265-305, 1986.

Hanes, D.M, V. Alymov, Y.S. Chang, and C. Jette, Wave-Formed Sand Ripples at Duck, North Carolina, *J. Geophys. Res., 106,* 22575-22592, 2001.

Hay, A.E. and D.J. Wilson, Rotary Sidescan Images of Nearshore Bedform Evolution During a Storm, *Mar. Geol., 119,* 57-65, 1994.

Howd, P. and J. Brodersen, Climatology of a Bottom Boundary Layer and Acoustic Proxies for Sediment Suspension, *Eos. Trans. AGU, 83*(47), Fall Meet. Suppl., Abstract OS61A-0189, 2002.

Inman, D.L., Wave Generated Ripples in Nearshore Sands, *Tech. Memo. 100*, 66pp., U. S. Army Corps of Eng., Beach Erosion Board, Washington, D.C., 1957.

Jette, C.D. and D.M. Hanes, High-Resolution Sea-Bed Imaging: An Acoustic Multiple Transducer Array, *Meas. Sci. Technol., 8*, 787-792, 1998.

Jonsson, I.G., Wave Boundary Layers and Friction Factors, in *Proceedings 10th Coastal Engineering Conference,* Publisher, Location, 1966.

Kobayashi, N. and B.D. Johnson, Sand Suspension, Storage, Advection and Settling in Surf and Swash Zones, *J. Geophys. Res., 106,* 9363-9376, 2001.

Li, M.Z., L.D. Wright, and C.L. Amos, Predicting Ripple Roughness and Sand Resuspension under Combined Flows in a Shoreface Environment, *Mar. Geol., 130,* 139-161, 1996.

Li, M.Z., C.L. Amos, and D.E. Heffler, Boundary Layer Dynamics and Sediment Transport under Storm and Non-Storm Conditions on the Scotian Shelf, *Mar. Geol., 141,* 157-181, 1997.

Li, M.Z. and C.L. Amos, Predicting Ripple Geometry and Bed Roughness under Combined Waves and Currents in a Continental Shelf Environment, *Continental Shelf Res., 18,* 941-970, 1998.

MacMahan, J., A.J.H.M. Reniers, E.B. Thornton, and T.P. Stanton, Infragravity Motions on a Complex Beach, Part I: Observations, submitted to J. Geophys. Res., 2002.

Miller, M.C., I.N. McCave, and P.D. Komar, Threshold of Sediment Motion under Unidirectional Currents, *Sedimentology, 24,* 507-527, 1977.

Miller, M.C. and P.D. Komar, Oscillation Sand Ripples Generated by Laboratory Apparatus, *J. Sedimen. Petrol., 50*(1), 173-182, 1980(a).

Miller, M.C. and P.D. Komar, A Field Investigation of the Relationship Between Oscillation Ripple Spacing and the Near-Bottom Water Orbital Motions, *J. Sedimen. Petrol., 50*(1), 183-191, 1980(b).

Mogridge, G.R. and J.W. Kamphuis, Experiments on Bedform Generation by Wave Action, *Coastal Engineering, Proceedings of the 13th Conference.,* pp. 1123-1142, Am. Soc. Civ. Eng., New York, 1972.

Nielsen, P. *Coastal Bottom Boundary Layers and Sediment Transport.* Adv. Ser. On Ocean Eng., vol 4. World Sci., Singapore, 324 pp, 1992.

Nielsen, P., Dynamics and Geometry of Wave-Generated Ripples, *J. Geophys. Res., 86,* 6467-6472, 1981.

Nielsen, P., Suspended Sediment Concentrations under Waves, *Coastal Engineering, 10,* 23-31, 1986.

Reniers, A.J.H.M., J. MacMahan, E.B. Thornton, and T.P. Stanton, Infragravity Motions on a Complex Beach, Part II: Modeling, submitted to J. Geophys. Res., 2002.

Shields, I.A., Anwedjung der Aehnlichkeitsmichanic und der Turbulenz-forschung auf die Geschiebebewegung. Mitt. Preuss, Berlin, 1936.

Sleath, J.F.A. *Sea Bed Mechanics.* John Wiley, New York, 1984.

Stanton, T.P., www.oc.nps.navy.mil/~stanton/, 1999.

Stanton, T.P., Characterizing Wave-Forced Bedforms using a Two-Axis Scanned Acoustic Altimeter, submitted to *J. of Atm. and Oc. Tech.,* 2000.

Sternberg, R.W., Predicting Initial Motion and Bedload Transport of Sediment Particles in the Shallow Marine Environment, in *Shelf Sediment Transport: Process and Pattern*, Dowden, Hutchinson and Ross, Stroudsburg, PA, 61-82, 1972.

Swart, D.H., Offshore Sediment Transport and Equilibrium Beach Profiles, *Delft Hydraul. Lab. Publ., 131*, 1974.

Traykovski, P., A.E. Hay, J.D. Irish, and J.F. Lynch, Geometry, Migration and Evolution of Wave Orbital Ripples at LEO-15, *J. Geophys. Res., 104,* 1505-1524, 1999.

Wiberg, P.L., and C.K. Harris, Ripple Geometry in Wave-Dominated Environments, *J. Geophys. Res., 99,* 775-789, 1994.

Wilson, J.C. Analysis of Bed Load Motion at High Shear Stresses, *J. Hydr. Eng., 113,* 97-103, 1987.

Wright, L.D., J.D. Boon, M.O. Green, and J.H. List, Response of the Mid-Shoreface of the Southern Mid-Atlantic Bight to a "Northeaster", *Geo-Marine Letters, 6,* 153-160, 1984.

Yalin, M.S., An Expression for Bedload Transportation, *J. Hydraul. Div. Proc. ASCE 89*(HY3), 221-250, 1963.

THIS PAGE INTENTIONALLY LEFT BLANK

INITIAL DISTRIBUTION LIST

1.   Defense Technical Information Center
        Fort Belvoir, Virginia

2.   Dudley Knox Library
        Naval Post Graduate School
        Monterey, California

3.   Professor Timothy P. Stanton
        Naval Postgraduate School
        Monterey, California

4.   Professor Edward B. Thornton
        Naval Postgraduate School
        Monterey, California

5.   Professor Mary L. Batteen
        Naval Postgraduate School
        Monterey, California

6.   Commander John Joseph
        Naval Postgraduate School
        Monterey, California

7.   Dr. Ad Reniers
        Delft Engineering
        Delft, Netherlands

8.   James Stockel
        Naval Postgraduate School
        Monterey, California

9.   Robert Wyland
        Naval Postgraduate School
        Monterey, California

THIS PAGE INTENTIONALLY LEFT BLANK